Fall 2020

Modification of the optical response of alpha quartz via the deposition of gold nanoparticles in etched ion tracks

Maria C. Garcia Toro

Department: Nuclear Engineering and Radiation Science

MODIFICATION OF THE OPTICAL RESPONSE OF ALPHA QUARTZ VIA THE DEPOSITION OF GOLD NANOPARTICLES IN ETCHED ION TRACKS

by

MARIA CAMILA GARCIA TORO

A DISSERTATION

Presented to the Graduate Faculty of the

MISSOURI UNIVERSITY OF SCIENCE AND TECHNOLOGY

In Partial Fulfillment of the Requirements for the Degree

DOCTOR OF PHILOSOPHY

in

NUCLEAR ENGINEERING

2020

Approved by:

Joseph T. Graham, Advisor
Carlos H. Castano
Joshua P. Schlegel
Miguel L. Crespillo
Richard K. Brow

PUBLICATION DISSERTATION OPTION

This dissertation consists of the following three articles, formatted in the style used by the Missouri University of Science and Technology:

Paper I: Anisotropic Nanowell Formation by Vapor Etching of Ion Tracks Generated by High Electronic Excitation in α-Quartz, found on pages 22-54, will be submitted to the journal of Nuclear Instruments and Methods in Physics Research Section B: Beam Interactions with Materials and Atoms.

Paper II: Raman Characterization of Phonon Confinement and Strain Effects from Latent Ion Tracks in ***α***-Quartz, found on pages 55-78, will be submitted to the Journal of Raman Spectroscopy.

Paper III: Enhancement of Plasmon-Phonon coupling in etched ion tracks in α-Quartz, found on pages 79-95, is intended for submission to Nanotechnology.

ABSTRACT

This study addresses the experimental methods used to develop and characterize plasmonic devices capable of modifying the optical response of alpha quartz via the deposition of gold nanoparticles in etched ion tracks. In the first part of the research, the microstructural characterization of latent and etched ion tracks produced in alpha quartz (α-SiO_2) is presented. Single crystals of α-SiO_2 were irradiated with two highly energetic ions to different nominal fluences. As expected, the morphology of the resulting ion tracks depends on the energy of the incident ion and their stopping powers within the target material. Subsequent chemical vapor-etching was conducted to create nanowells in the crystal structure. The etching process resulted in facetted nanowells, whose superficial dimensions increased with etching times and etchant concentrations. It was found that the etching rate is highly dependent on crystal orientation. Additionally, Raman spectroscopic analysis of the phonon confinement effect and strain due to the ion tracks is presented. Results show that the optical phonon modes undergo a shift towards higher frequencies while broadening asymmetrically compared to the unirradiated samples due to phonon confinement effects. In the second part of the research, the deposition of gold nanoparticles inside of the nanowells was conducted. The modification of the optical response of quartz by depositing gold nanoparticles in the nanowells is discussed. An increase in the Raman intensity was observed thanks to the enhancement of the electromagnetic field produced by localized surface plasmons at the surface of the gold nanoparticles. The deposition of nanoparticles in etched ion tracks in fused silica was also achieved and is also briefly discussed.

ACKNOWLEDGMENTS

I would like to express my sincere and deepest gratitude to my advisor Dr. Joseph T. Graham, for his guidance, encouragement, patience, and motivation to develop this research. He has played an important influential role during this time of the greatest accomplishments in my life. I would also like to thank Dr. Miguel L. Crespillo for providing his unending advice and expertise that continuously helped me improve my knowledge for the completion of this work. I would like to thank the other members of my advisory committee: Dr. Carlos H. Castano, Dr. Joshua P. Schlegel, Dr. Richard K. Brow, who were involved in this work, I am thankful for their very valuable comments on this thesis and their participation during my final defense.

This thesis could not have been done without funding opportunities from the Nuclear Engineering Department of Missouri University of Science and Technology and the Nuclear Regulator Commission Faculty Development Grant NRC-HQ-84-15-G-0044. Also, I want to thanks the staff in the Ion Beam Materials Laboratory at the University of Tennessee Knoxville and in The Centro de Microanálisis de Materiales - Universidad Autónoma de Madrid for assistance with experimental irradiations, and the Materials Research Center (MRC) at Missouri S&T for its support and use of equipment.

From the bottom of my heart, I would like to thanks my parents, Flor and Jorge, for their dedication and support during all my life, my sister, Diana, for being the best sister and best friend for me, and my amazing boyfriend and best friend, Carlo, for his love, patience and pleasant company in all my adventures during these years.

TABLE OF CONTENTS

LIST OF ILLUSTRATIONS

SECTION Page

SECTION

LIST OF TABLES

PAPER I Page

SECTION

SECTION

1. INTRODUCTION

Over the past ten years, the term "plasmonics" has been designated to new technology focused on improving the optical properties of materials using surface plasmons in metallic nanostructures to help guide and manipulate light at the nanometric scale [1]. Metallic nanostructures can alter the way that light scatters from the molecules thanks to the ability of their optical properties to support collective light-induced electronic excitations (plasmons) [2]. Materials that use plasmons to achieve optical properties not seen in nature are known as plasmonic materials.

The most important advances in plasmonic materials are related to the capacity of the plasmonic nanostructures to concentrate light into nanoscale volumes, allowing fundamental studies of light-matter interactions at length scales that are otherwise inaccessible. Plasmonics is expected to be the key in nanotechnology that will merge electronics and conventional photonic components on the same nanodevice [3]–[6]. Figure 1.1 shows the relationship between device operating speed and device size within different technology paradigms. Each of these technologies can perform unique functions. The electrical properties of semiconductors and the high transparency of dielectrics facilitate information storage and information transport over long distances. However, semiconductor electronics are limited in speed by heat generation, and dielectric photonics are limited in size by diffractive effects. Metallic nanoplasmonics,

which utilize near-field phenomena, can act as a bridge between nanoelectronics and dielectric photonics by combining small size and high speeds [1].

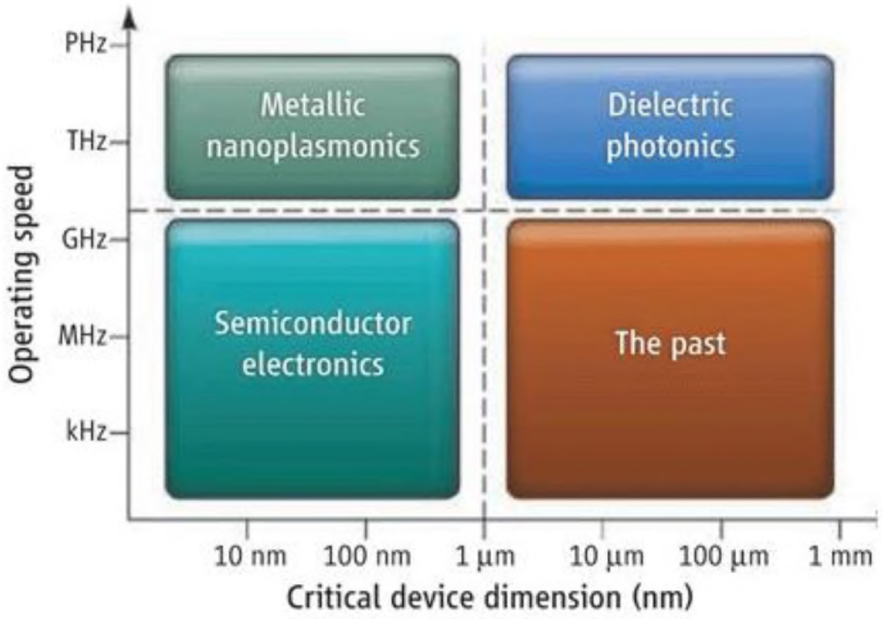

Figure 1.1. Operating speed vs critical device dimension of metallic nanoplasmonics, dielectric photonics, and semiconductor electronics. From Brongersma, M.L., and Shalaev, V.M., 2010. The case for plasmonics. science, 328(5977), pp.440-441. Reprinted with permission from AAAS

All forms of light-matter interaction are heavily influenced by the optical density of states (DOS) in different materials. The DOS represents the number of 'channels' for storing and/or routing the electromagnetic energy in a specific medium. Materials with DOS values higher than that of ordinary isotropic media can be engineered to enhance light absorption and emission, enabling localized heating and driving near-field heat exchange between hot and cold surfaces. Some applications that use materials with high

DOS values include solid-state lighting, solar-thermal technologies, photovoltaics, and thermophotovoltaics [7]–[10].

In an interface of a metal-dielectric material, the incident light can excite coherent electron density oscillations, the quanta of which are known as plasmons. The free electrons at the metallic surface absorb the energy of the incident photon and oscillate collectively producing both charge motion in the metal and electromagnetic waves in the dielectric material, in accordance with Maxwell's laws. These excitations are known as surface plasmon polaritons [11], [12].

When a metallic material is macroscopic in size, the free electrons can travel along the metal reflecting the light and producing the luster characteristic of conductive materials. When the metallic structure is nanometers in scale, however, its free electrons are confined within a small space, limiting the frequencies at which they can vibrate. The characteristic frequencies of the oscillation depend on the size and shape of the metallic nanostructure. Such plasmons only absorb the fraction of the incoming light that oscillates at the same frequency as the plasmon itself, reflect the rest of the light. These so-call localized surface plasmons have large DOS values and are thus able to locally concentrate the oscillating electric field component of electromagnetic radiation at specific frequencies [13], [14]. The large DOS of plasmonic nanomaterials and their ability to absorb EM radiation and locally concentrate electric fields has been successfully used for nanoantennas [15], [16], efficient solar cells [17]–[19], nanoplasmonic biosensors [20]–[24], surface-enhanced Raman spectroscopy [25]–[28], localized heat generation [29]–[32], smart coatings [33]–[37], plasmonic nanofilters [38]–[40], and other useful devices.

Plasmonic nanoparticles strongly modify the phase of the optical field in their vicinity due to their capacity to couple their electron density with an electromagnetic field with wavelengths that are larger than the nanoparticle itself [41]. When two or more nanoparticles are near each other, separated by a distance comparable to or smaller than their diameters, additional electromagnetic effects appear [42]–[45]. Plasmon coupling occurs when two or more plasmonic nanoparticles form clusters and their near-field surface plasmons begin to hybridize. This creates a boosted localized electric field within the clusters (hot spots), as well as favors the exchange of hot electron between adjacent nanoparticles. Previous studies have reported an enhancement of the interparticle electric field by several orders of magnitude, far-exceeding the field enhancement created by single plasmonic nanoparticles [46]–[49]. One of the sensing applications that use plasmon coupling to achieve ultralow detection limits is surface-enhanced Raman spectroscopy [50].

Indeed, the incorporation of nanostructures with plasmonic properties into optoelectronic devices is believed to be a promising approach to modify specific device properties without increasing the size of the device. The plasmon coupling is thus able to combine photonics, electronics, and all of the advantages of nanotechnology in one device while enhancing the optical near-field at sub-wavelength length scales.

1.1. RESEARCH OBJECTIVE AND CONTRIBUTION

This research is aimed towards constructing a device to modify the optical properties of alpha quartz (α-SiO_2) by reinforcing external electromagnetic fields near the crystal surface via localized plasmonic resonance of gold nanoparticles. To achieve this

goal, the experimental campaign was divided into three parts: first, α-SiO_2 samples were irradiated with highly energetic ions to create amorphous areas (ion tracks) in the crystal structure; second, the nanowells were produced by chemical vapor etching of the ion tracks with hydrofluoric acid solutions; and third, gold nanoparticles were deposited inside the etched nanowells. The deposition of gold nanoparticles in etched tracks in fused silica is also briefly discussed. The modification of the optical properties of quartz by the presence of the gold nanoparticles was evaluated with Raman spectroscopy. Additionally, a quantitative analysis of the phonon confinement effect and coherence lengths produced by the ion tracks and subsequently etched nanowells are presented. Phonon confinement effect refers to the alteration of the phonon transport along a crystal structure due to the presence of defects or impurities.

The formation of latent ion tracks in dielectric materials has been studied extensively. Some of the studies include amorphous and crystalline (quartz) SiO_2 [51]–[63]. However, with regard to chemical etching, most of the studies that involve etching of ion tracks in SiO_2 have been conducted on amorphous SiO_2 substrates [64]–[67]. One essential reason for the lack of knowledge on the chemical etching of ion tracks produced in α-SiO_2 is its complex crystal structure. It has been difficult to predict the results of α-SiO_2 etching with models based exclusively on theoretical assumptions. Experimental studies conducted so far include analysis of possible crystallographic planes and the etch rates for various etchants and the rate-controlling steps [68]–[71]. However, to our knowledge, no authors have conducted etching studies on ion tracks in crystalline SiO_2, much less explored the possibility of developing novel plasmonic devices using the resulting nanostructures.

Thus, this dissertation extends the current state of knowledge of: (1) the irradiation response of α-SiO_2 and its dependence on different crystal orientations, ion energies, stopping power, and ion velocities; (2) α-SiO_2 chemical vapor etching rates in ion tracks, its anisotropic behavior, and dependence on the crystal orientation and etchant concentration.

Furthermore, the integration of the gold nanoparticles into the nanowell structures resulting from ion track etching shows a strong coupling between localized surface plasmons and optical phonons. The plasmonic properties of these devices combined with the optical properties of quartz may represent a useful vertex in optoelectronics, photonics, and nanotechnology.

1.2. DISSERTATION OUTLINE

This dissertation is based on the manuscripts that were prepared to be submitted to peer-review journals and is divided into three different sections. Section 1 provides a brief introduction to the research topic, as well as the research objectives, contributions, and some background information that establishes the state of knowledge on the topic of this study. Section 2 contains three manuscripts that present: (1) the ion track formation by irradiating α-SiO2 samples with highly energetic ions and subsequent chemical vapor etching with HF solutions to create nanowells. Microstructural characterization of the latent and etched ion tracks was conducted with AFM measurements; (2) a quantitative analysis of phonon confinement in α-SiO_2 by the presence of ion tracks and nanowells. Calculations of the coherence length were conducted by fitting the experimental results with results obtained by the phonon confinement model (PCM) and Density Functional

Perturbation Theory (DFPT) calculations; and (3) a detailed analysis of how the optical response of irradiated and etched α-SiO_2 is modified by localized surface plasmons. This analysis was conducted using Raman microscopy.

2. STATE OF KNOWLEDGE

2.1. ALPHA QUARTZ

Quartz is the crystalline form of SiO_2 and is one of the most abundant minerals in the Earth's crust. Quartz is a thermally stable oxide that presents interesting optical and electrical properties, which in conjunction with high resistance to chemical attack, have made it one of the materials widely used in many diverse applications including microelectronics, construction materials, integrated optics, spectroscopy, and others [72]–[76]. Quartz exists in two different forms: alpha quartz (α-SiO_2) is stable under standard conditions while beta quartz (β-SiO_2) is a high-temperature phase. The transformation from the α-quartz to β-quartz occurs at 573 °C and atmospheric pressure.

2.1.1. Crystal Structure of Quartz. Both forms of quartz belong to trapezohedral crystal classes. α-SiO_2 belongs to the 3 2 class in the trigonal crystal system, while β-SiO_2 belongs to the 6 2 2 class in the hexagonal crystal system. Figure 2.1 shows the crystal habit of α-quartz and defines the conventional lattice vectors ($\boldsymbol{a}_1$, $\boldsymbol{a}_2$, $\boldsymbol{a}_3$, and $\boldsymbol{c}$) and Cartesian axes (X,Y, and Z). α-quartz presents a characteristic threefold symmetry around its optical axis (c-axis) that is perpendicular to the prismatic planes. Perpendicular to the c-axis are the three equivalent electrical X-axes, each with twofold symmetry, and three equivalent mechanical Y-axes.

The unit cell of α-quartz has dimensions of a=b=4.91 Å and c = 5.41 Å, and consists of three SiO_2 groups rotated with respect to each other by 120°. The atomic structure of quartz is such that every silicon atom is surrounded by a regular tetrahedron of four covalently bonded oxygen atoms.

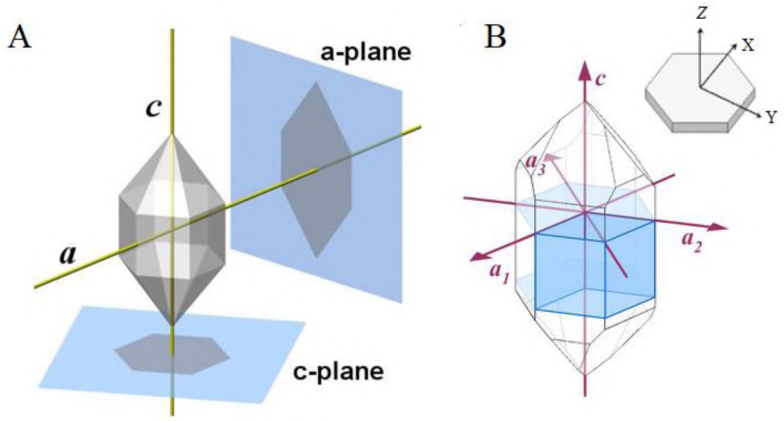

Figure 2.1. Crystal habit of α-quartz. (A) Projection of quartz crystal structure onto a- and c-planes. (B) definition of lattice vector and Cartesian coordinates Adapted from http://www.quartzpage.de/gen_struct.html

The O atoms are shared with other Si atoms forming oxygen bridges. The bond lengths are 1.61 Å for Si-O and 2.65 Å for O-O (nearest neighbors) and the Si-O-Si bonds form an angle of 144°. -Si-O-Si- chains form continuous helical (and chiral) paths around three-fold screw axes parallel to the c-axis. Figure 2.2 shows the unit cell of quartz generated in VESTA [77], a three-dimensional visualization system for crystallographic studies and electronic state calculations. In Figure 2.2, the silicon atoms are represented by blue spheres, the red spheres represent the oxygen atoms, and the green rods represent the Si-O atomic bonds.

2.1.2. Anisotropic Properties of Quartz. The crystal structure not only defines the symmetries of a material but also plays an important role in material properties. Quartz, being an anisotropic material can show anisotropic or direction-dependent physical properties. Some of these anisotropic properties include refraction,

birefringence, optical activity, hardness, thermal conductivity, piezoelectricity, and relative permittivity. [78]–[81].

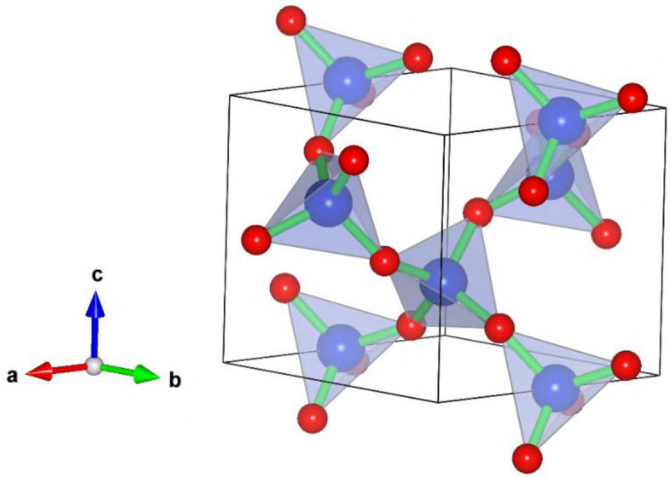

Figure 2.2. Crystal structure of quartz

2.2. IRRADIATION WITH ENERGETIC IONS

Material modification via high-energy ion irradiation has been a topic of great interest as it is possible to alter the physical and chemical properties of materials. Ion irradiation can modify the crystal structure through the introduction of defects such as voids, dislocations, grain boundaries, and amorphous regions [82]–[84]. Examples of properties that have been modified through irradiation include the index of refraction, dielectric constant, absorbance, and chemical reactivity [63], [82], [85]–[87].

The interaction of energetic ions with a target material can be analyzed from two different perspectives: from the perspective of the incident ion that loses energy in the

target, and from the perspective of the target material that experiences rapid and dramatic nuclear and electronic excitation from the deposited ion energy. Such energy deposition can bring about both transient and permanent changes to the crystal structure.

From the perspective of the incident energetic ions, the ions interact with the target by shedding their kinetic energy through two main energy loss mechanisms: nuclear energy loss and electronic energy loss. The nuclear energy loss regime occurs at low ion energies (on the order of keV/amu), where elastic collisions are produced between the incident ions and the atoms in the target material. At higher energies (higher than about 0.1 MeV/amu), the incident ions transfer their energy to the electrons of the target through inelastic collisions, inducing ionization and initiating a cascade of secondary electrons that spreads radially from the track core [55], [88]–[91]. In less than a picosecond, energy in the electrons is transferred to the atoms, resulting in rapid lattice heating that can produce localized melting and cooling. Depending on the temperatures and rates of heating and cooling disordered areas, amorphous zones, recrystallized zone, and new phases can form along the ion pathway.

From the perspective of the target material, the nuclear energy loss regime produces point defects and defect clusters in the crystal matrix. Such defects include: vacancies, vacancy clusters, self-interstitial atoms, interstitial clusters, antisites (in the case of certain compounds), and implanted ions. In the electronic energy loss regime, the type of defects introduced will depend on the electronic structure of the material. High-energy ions introduce a high density of electronic excitations through inelastic collisions. The nature of these excitations and their stability depends on the electronic structure of the material. Trapped carriers can remain for long periods in insulators and

semiconductors while excited electrons dissipate their energy in conductors as thermal energy without creating a significant number of defects [91]–[94]. However, in both cases, the rapid dissipation of energy from the electrons into the lattice can result in localized lattice heating and the production of latent ion tracks. This will be discussed in further detail below.

Stopping power is a quantity that characterizes the energy loss decelerating an incident ion during its passage through a material. The nuclear stopping power (S_n) accounts for nuclear energy loss (elastic ion-ion collisions) while the electronic stopping power (S_e) accounts for electronic energy loss from inelastic collisions with orbital electrons. Ion track formation, permanent structural changes along the track core, have been observed at sufficiently high values of S_e. Experimentally one sees that the S_e value needs to be higher than a certain threshold value (S_{Th}) in order for highly defective or amorphous ion tracks to form [55], [88], [95].

The formation of ions tracks is still not completely understood. Different theories exist, including: the Coulomb explosion explanation [96]–[99], reduced electronic energy loss [100], thermal spike model [55], [101]–[104], bond weakening [105], [106] , among others. This section will include just a general explanation of the two more popular models, the Coulomb explosion model proposed by Fleischer et al. [97] and the inelastic thermal spike model proposed by Dessauer [104].

The Coulomb explosion model proposes a “cold” mechanism that transforms the energy of the incident ion into atomic motion via electrostatic repulsion. This model assumes that the incident energetic ion strips outer valence electrons from the target

atoms, breaking the chemical bonds between the atoms, and creating a highly ionized region along the ion pathway.

The ionized electrons are ejected away from the track core creating a positive space charge region in the core surrounded by a negative space charge region from the surrounding electrons. The partially ionized atoms in the core, being positive, experience mutual electrostatic repulsion and rapidly explode into a plasma of more fully ionized matter. This explosion produces a large number of atomic displacements creating the amorphous tracks. This model offers an explanation for the insensitivity to ion irradiation observed in hard insulators and metallic materials in the electronic energy loss regime, as well as the description of the conditions under which repulsive Coulomb forces are sufficient to overcome lattice bonding forces [101].

The inelastic thermal spike model proposes a mechanism that involves a melting process along the ion pathway followed by a rapid cooling process. Amorphous regions form in the ion track as a consequence of supercooling. The incident ion loses its kinetic energy through inelastic collisions with the electrons on the target material producing a dense column of electronic excitation in its wake. The excited electrons quickly equilibrate with each other through electron-electron interactions and establish quasi-equilibrium in which the electrons have a well-defined temperature many thousands of degrees hotter than the lattice temperature. As the hot electrons diffuse outward from the track core they also transfer heat to the cold lattice through the electron-phonon coupling resulting in a spike in the lattice temperature and a drop in the electron temperature.

If sufficient energy is deposited along the track, highly localized heating will melt a columnar region of material around the track. This process is followed by rapid

cooling as the heat is conducted into the surrounding cool matrix. When cooling is sufficiently rapid, the material may be supercooled and form a glassy amorphous core.

At slower cooling rates, recrystallization and annealing are also possible. The competition between amorphization, recrystallization, and annealing are thought to establish the observed threshold stopping power for track formation. This model offers an explanation for the dependence of the amorphous track diameter on the electronic stopping power and also offers some insights into the ion annealing effect.

As mentioning before, permanent changes in the crystal structure can occur when a material is irradiated with high-energy ions above the electronic stopping power threshold (S_{Th}). Previous studies [55], [88], [91], [102], [107], had reported the relationship of the ion track morphology with the S_e in dielectric materials. When S_e is close to S_{Th}, the pass of the ion through the material creates extended spherical point defects with small radii (about 1.5 nm). Upon increasing the S_e the point defects begin to elongate forming discontinuous cylinders of similar radii. Once S_e is larger enough to produce continuous tracks, the track radius increases with S_e. When the track radius is larger than ~ 3 nm, the tracks begin to become regular, homogeneous cylinders. Figure 2.3 shows the effective radii (R_e) in crystalline SiO_2 for different values of S_e from both experiments conducted by Meftah *et al.* [55] and calculations in the framework of the exciton model from Itoh [108]. Meftah *et al.* irradiated samples of alpha quartz at room temperature at the 7 MV tandem Van de Graaff accelerator at Bruyeres le Chatel, and at the Grand Accelerateur National d'Ions Lourds (GANIL) facility in Caen, France.

The irradiations were conducted with ^{19}F, ^{32}S, and ^{63}Cu ions with incident energies of 0.79, 1.56, and 0.79 MeV/amu, respectively, covering a S_e range between 2.4

and 9 keV/nm. The ion beam flux was on the order of 10^9 ions cm^{-2} s. Rutherford backscattering ion channeling (RBS-C) and electron microscopy were used to measure the damage cross-section ($A=\pi R_e^2$). Figure 2.4 shows the effective radius versus the energy loss for amorphous tracks created in yttrium iron garnet irradiated with ions at 15 MeV/amu (triangles), at 2 MeV/amu (circles) [109], and with cluster beams (square) [110]. The track morphology was directly linked to the damage cross-section area, A. S_e dependent track morphology was observed in several materials and seems to be a rather general feature [111]. The ion velocity also determines track formation and morphology [102], [109], [112]. For a given S_e, ions with high specific energy (MeV/amu) deposit its kinetic energy over a larger radius from the track core, resulting in wider continuous tracks. Consequently, when the ion energy increases, the S_{Th} increases for fixed stopping power. This phenomenon is sometimes referred to as the velocity effect.

It is important to note that ion tracks have a different density than the bulk material. Compared to the crystalline matrix, the highly disordered volume within the tracks has a reduced density from the more random bonding arrangement. This results in swelling that can be observed as a hillock with nanometric dimensions at the sample surface [113], [114]. In the case of initially amorphous materials, the passage of the ion can produce densification and plastic deformation along the ion pathway, creating compacted ion tracks [56], [62], [88], [112], [115]. Other surface modifications produced by ion irradiation include: surface roughness, sputtering, and the creation of holes.

The formation of latent ion tracks in dielectric materials has been studied extensively. Some of these studies include ion track formation in amorphous and crystalline silicon dioxide (SiO_2) [51]–[63], [112], [116]. Therefore, the presence of

latent ions tracks and the fabrication of nanopores in quartz is a promising area within materials science and engineering [92], [117].

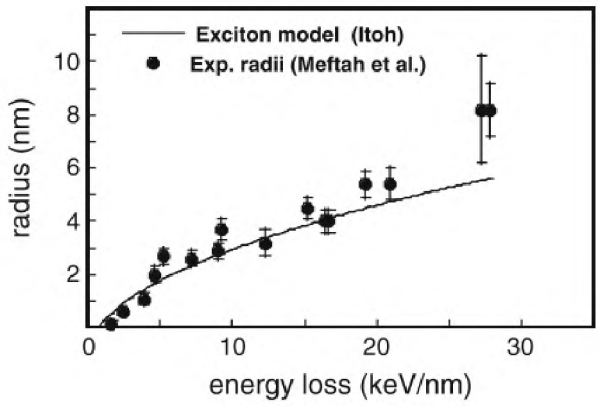

Figure 2.3. Experimental effective track radius in crystalline SiO_2 for different Se. Experimental data from Meftah et al. [55] and calculations from Itoh [108]. Taken from [102]

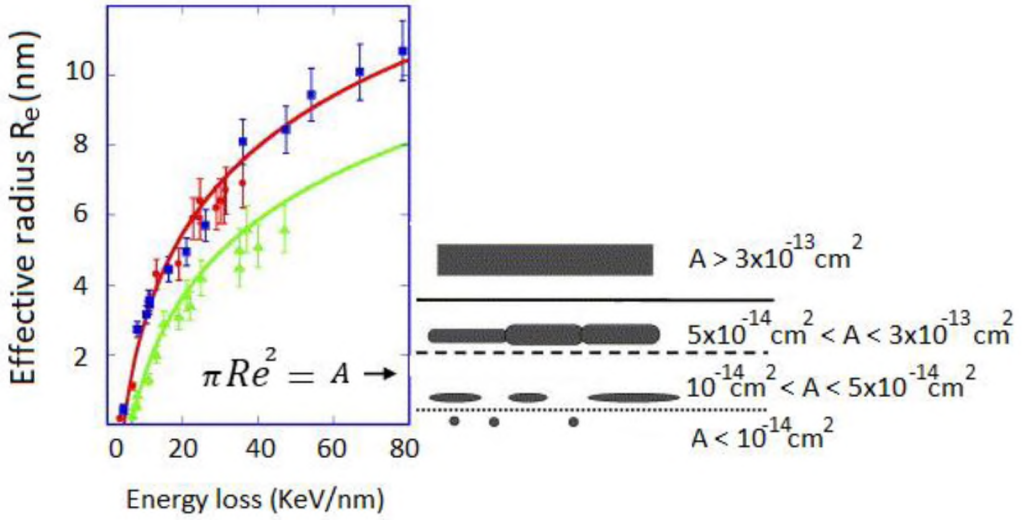

Figure 2.4. Effective radius versus the energy loss for amorphous tracks created in yttrium iron garnet irradiated with ions at 15 MeV/amu (triangle), at 2 MeV/amu (circle) [109], and with cluster beams (square) [110]. The track morphology was directly linked to the damage cross section *A*. Taken from [88]

2.3. CHEMICAL ETCHING OF ION TRACKS

Chemical etching of ion tracks is an effective way to produce nanometer sized pores in an ion irradiated material. The highly disordered regions inside the ion tracks make the tracks more susceptible to the chemical attack and therefore etch at a faster rate than the non-irradiated areas [118], [119]. As a consequence, the ion track is etched faster than the pristine crystal, forming pores [64], [120]. A major advantage of ion track etching is that multiple parameters beyond the etching conditions can be controlled. These include the ion energy and species, the ion fluence, and incident angle. As such, this method may be tailored to suit a wide variety of applications and materials.

At room temperature, SiO_2 is chemically inert to most substances. The reason for its low reactivity is the strong Si-O bond and its macromolecular structure. Being an anhydrite of an acid itself (orthosilicic acid H_4SiO_4), it will not be attacked when exposed to a wide number of acids, hydrofluoric acid (HF) being a prominent exception. When exposed to HF, SiO_2 will decompose to form silicon fluoride (SiF_4) and then hydrofluorosilic acid ($H_2[SiF_6]$). Some studies report that HF in combination with ammonium fluoride (NH_4F) can produce especially uniform surfaces [68], [69].

The HF etching reaction is based on two mechanisms: first, the acidic component (H^+) breaks the siloxane bonds at the SiO_2 surface forming silanol species [121]. Second, the silanol groups interact with the fluorinate species from the etchant, changing the electric field at the surface, and allowing the replacement of these OH groups by F or HF. The resulting increase of the electronegativity causes nucleophilic chemisorption of HF to the silicon, eventually causing the SiF_4 to detach from the surface [64], [122]–[127]. The general reaction equation SiO_2 with an HF etchant can be described by Equation (1):

$$SiO_{2\,(s)} + 4HF_{(aq)} \longrightarrow SiF_{4\,(g)} + 2H_2O_{(g)} \quad (1)$$

SiF_4 and excess water are volatile and are desorbed from the surface [69]. Additionally, some of the water will interact with both the newly exposed Si-O bonds at the surface and the HF molecules, creating a positive feedback mechanism that increases the reaction rate [64], [128]. The chemical etching mechanism does not seem to differ between amorphous and crystalline SiO_2 [68], but, in the case of α-SiO_2, the etching rate depends on the crystallographic orientation, where the fastest etching rate proceeds on the plane perpendicular to the optical axis (R(Z) > R(AT) > R(+X) > R(-X) > R(Y)) [68], [129].

A previous study suggested that the etching rate depends on the number of oxygen atoms that are exposed on the SiO_2 surface [122]. In that study, the author proposed four different ways in which the atomic structure can be exposed at the SiO_2 surface. Figure 2.5 shows the four possible surface exposures of the SiO_4 tetrahedron. Type I is the most unstable configuration and may be removed in the presence of water through the formation of silanol. Type IV tetrahedra are mostly unreactive due to steric considerations that make it difficult to construct an alternative coordination site close to the silicon atom. In aqueous systems, exposed oxygen anions are electrically neutralized by protons forming a surface layer of hydroxyl groups (OH). Upon exposure to HF, the OH groups are replaced by F or HF. Figure 2.6 shows an example of how the Type II tetrahedron can be modified in presence of HF. The Si atom can coordinate up to six fluorine atoms to satisfy the electrical neutrality requirements.

In Figure 2.6, the hybrid tetrahedron will tend to coordinate a further complement of fluorine ions, leading to the full exchange of O to F and increase the electronegativity

of the tetrahedron. This produces a SiF_4 molecule which then detaches from the sample surface. It is important to note that the number of oxygen atoms at the sample surface, and therefore the concentration of types I-IV, will depend on the crystal structure

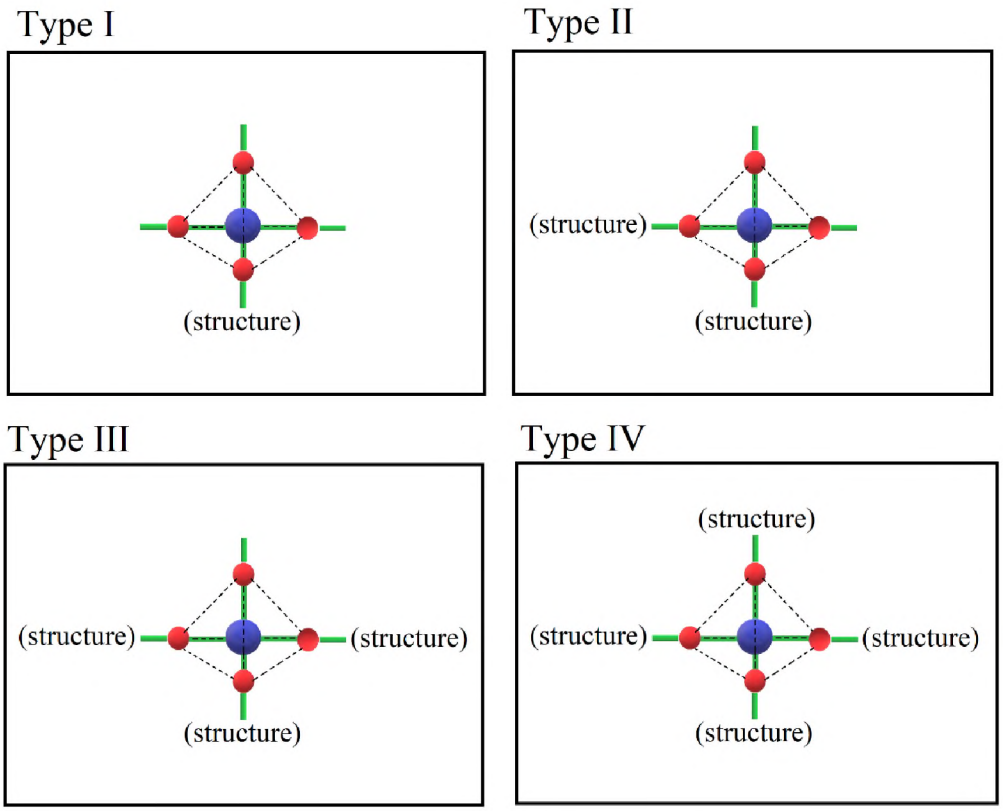

Figure 2.5. Four possible surface configuration of the SiO_4 tetrahedron. Adapted from [122]

In amorphous SiO_2, the four types will occur randomly and therefore isotropic behavior of the etching is observed. The presence of ion tracks in the crystal structure of α-SiO_2 favors the etching process along the ion track thanks to the amorphous region

created by the passage of the ion. At the same time, the anisotropic nature of the crystal will lead to differences in etching rates in various directions. Thus, the geometry of etched pores/nanowells can be irregular.

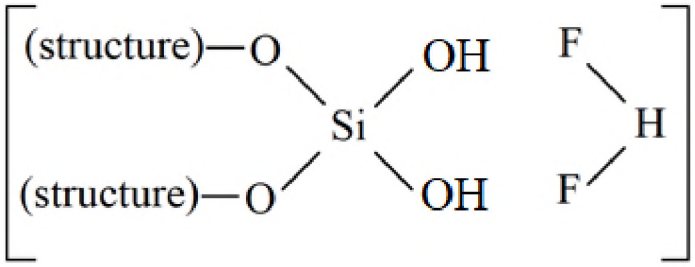

Figure 2.6. Hybrid SiO_4 tetrahedra resulting from the replacement of OH^- by F^-. Adapted from [122]

Chemical etching can be conducted as a wet process (by submerging the sample in the etchant solution) or a dry process (by exposing the sample to the vapor etchant at a specific distance from the liquid surface). Most of the studies that involve chemical etching of latent ion tracks in SiO_2 have been conducted on amorphous SiO_2 substrates [64]–[67]. These studies have demonstrated that wet-etching of amorphous SiO_2 produces conically shaped holes while vapor-etching produces more cylindrical-shaped holes [64], [120], [130], [131]. This difference in the hole shape can be explained as a consequence of the etching rate of the ion track (V_T) being comparable to the etching rate of the unirradiated crystal (V_B). A nearly cylindrical hole results when V_T is large

compared to V_B. The cone half-angle (φ) is given in Equation (2):

$$\varphi = \sin^{-1}\left(\frac{V_B}{V_T}\right) \tag{2}$$

A previous study had reported that liquid etching of the fission fragment tracks in fused silica produced conical pits with cone half angles of 15°-20° [60], [64]. Figure 2.7 schematically illustrates the etched ion track structure [132].

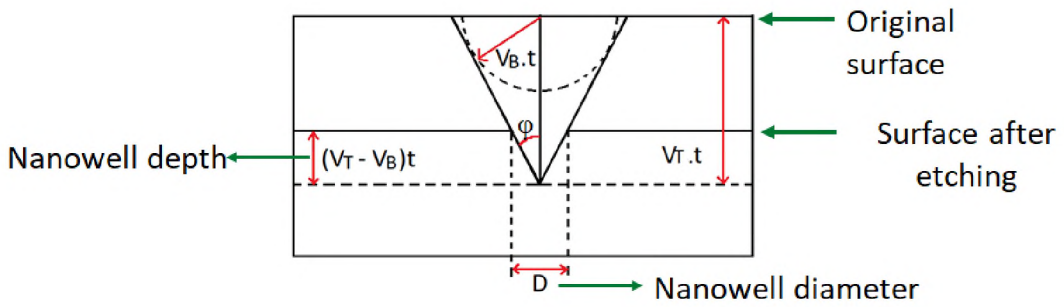

Figure 2.7. Diagram of an etched ion track. Adapted from [132]

PAPER

I. ANISOTROPIC NANOWELL FORMATION BY VAPOR ETCHING OF ION TRACKS GENERATED BY HIGH ELECTRONIC EXCITATION IN α-QUARTZ

Maria C. Garcia Toro [a], Miguel L. Crespillo [b], Jose Olivares [c,d], Joseph T. Graham [a,e].

[a] Nuclear Engineering Program, Missouri University of Science and Technology, 65409, Rolla, MO, United States

[b] Department of Material Science and Engineering, University of Tennessee, 37996, Knoxville, TN, United States

[c] Instituto de Optica, Consejo Superior de Investigaciones Científicas (IO,CSIC), Madrid, E-28006, Spain

[d] Centro de Micro-Análisis de Materiales (CMAM), Universidad Autónoma de Madrid, Madrid, E-28049, Spain

[e] Department of Materials Science and Engineering, Missouri University of Science and Technology, 65409, Rolla, MO, United States

ABSTRACT

This study reports a systematic microstructural characterization of latent and etched ion tracks generated by high electronic excitation in alpha quartz (α-SiO_2). Single crystals of Y- and Z-cut α-SiO_2 were irradiated at room temperature with 20 MeV Ni^{6+} ions and 40 MeV I^{7+} ions to different nominal fluences. The revealed morphology of the resulting ion tracks depends on the energy of the incident ion and the stopping power on the target material. Subsequent chemical vapor-etching with hydrofluoric acid solutions was conducted with varying etching times and acid concentrations. The vapor etching

process resulted in facetted nanowells, whose superficial dimensions increased with etching time and etchant concentrations. It was found that the etching rate is highly dependent on crystal orientation. The Y-cut samples etched more slowly than the Z-cut samples and exhibited anisotropic track etching behavior. Production of nanowells with different aspect ratios was accomplished by altering the etching time and etchant concentration. The obtained ion tracks and subsequently etched nanowells were characterized by Atomic Force Microscopy (AFM). A detailed procedure to generate templates with the stated nanostructures is presented. Such templates could be used in the fabrication of novel nanodevices with unique optical, thermal, and electronic properties.

Keywords: Nanowells, chemical etching, α-quartz, ion tracks, ion beam modification

1. INTRODUCTION

Nanomodification of materials is a topic of great technological interest as it is often observed that material properties can be radically altered when their chemical or physical characteristics are modified at the nanometer and atomic scale [1]–[4]. High energy irradiation is one of the tools used to alter the physical properties of materials. Through irradiation, it is possible to modify the crystal structure through the introduction of defects such as voids, dislocations, grain boundaries, and amorphous regions [5]–[7]. Examples of properties that have been modified through irradiation include refraction index, dielectric constant, absorbance, and chemical reactivity [5], [8]–[11].

1.1. ION TRACK FORMATION

Ion tracks represent one such irradiation-induced microstructural modification. Under irradiation, the incident energetic ions interact with the target material by losing their energy via two independent mechanisms.

In the nuclear energy loss regime, which dominates at low energies (on the order of keV/amu), elastic collisions are produced between the incident ions and the atoms in the target. At higher energies (> 0.1 MeV/amu), the incident ions transfer their energy to the electrons of the target through inelastic collisions (electronic energy loss regime), inducing ionization and initiating a cascade of secondary electrons that spreads radially from the track core [12]–[16]. In less than a picosecond, energy in the electrons is transferred to the atoms, resulting in lattice heating. The rapid lattice heating can result in localized melting and cooling that leaves behind disordered areas along the ion pathway, as well as small hillocks at the specimen surface.

Permanent changes in the structural properties occur when the electronic stopping power (S_e) is above a certain threshold (S_{Th}) required to form highly defective or amorphous zones [12], creating ion tracks embedded in the crystal matrix [16], [17]. The ion velocity also determines track formation and morphology [18], [19]. For a given S_e, ions with low specific energy deposit their kinetic energy over a deeper distance from the sample surface, resulting in larger continuous tracks. Consequently, when the ion energy increases, the S_{Th} increases for fixed stopping power. This phenomenon is sometimes referred to as the velocity effect.

Although ion tracks have importance in geological dating, microelectronics in radiation environments and the nuclear fuel cycle, interest in ion tracks in

nanotechnology and nanoscience mainly comes from their usefulness in fabricating tailored nanopores and nanowires. Modification of materials using ion tracks has contributed to a number of different technologies [15], [20]–[23]. The formation of latent ion tracks in dielectric materials has been studied extensively. Some of these studies include ion track formation in amorphous and crystalline silicon dioxide (SiO_2) [10], [16], [18], [24]–[35].

Quartz is one of the most abundant minerals in the Earth's crust. It is thermally stable, strong, and resistant to chemical attack. Thanks to its optical and electrical properties, α-quartz (α-SiO_2) is used in many diverse applications including semiconductors, construction materials, integrated optics, microelectronics, spectroscopy, and others [36]–[40]. Therefore, the presence of latent ions tracks and the fabrication of nanopores in quartz is a promising area within materials science and engineering [1],[41].

1.2. CHEMICAL ETCHING PROCESS IN SiO_2

Chemical etching is an effective way to produce nanowells in an ion irradiated material. When exposed to an etching solution, the ion tracks produced in the crystal matrix etch at a faster rate than the non-irradiated areas. As a consequence, the ion track is etched out before the pristine crystal gets removed, forming pores [42], [43].

This preferential etching is related to the presence of highly disordered regions along the length of the ion track and its susceptibility to the chemical attack [44], [45]. Chemical etching can be conducted as a wet process (by submerging the sample in the etchant solution) or a dry process (by exposing the sample to the vapor etchant at a specific distance from the liquid surface). For both amorphous and crystalline SiO_2, the

etching process is usually conducted with fluoride-based solutions. Some studies report that etchants with HF, often in combination with ammonium fluoride (NH_4F) can produce smooth surfaces [46], [47]. The chemical etching mechanism does not seem to differ between amorphous and crystalline SiO_2 [46], but, in the case of α-SiO_2, the etching rate depends on the crystallographic orientation (R(Z) > R(AT) > R(+X) > R(-X) > R(Y)) [46], [48]. A previous study suggested that the etching rate depends on the number of oxygen atoms that are exposed on the SiO_2 surface [49]. This dependence can be explained by the etching reaction that is based on two mechanisms: first, in the presence of an aqueous solution, the acidic component (H^+) breaks the siloxane bonds at the SiO_2 surface forming silanol species [50]. Second, the silanol groups interact with the fluorinate species from the etchant, changing the electric field at the surface, and allowing the replacement of these OH groups by F or HF. The resulting increase of the electronegativity causes nucleophilic chemisorption of HF to the silicon, eventually causing the SiF_4 to detach from the surface [42], [49], [51]–[55].

The general reaction equation SiO_2 with an HF etchant can be described by Equation (1):

$$SiO_{2\,(s)} + 4HF_{(aq)} \longrightarrow SiF_{4\,(g)} + 2H_2O_{(g)} \quad (1)$$

where the SiF_4 and excess water are volatile and are desorbed from the surface [47]. Additionally, some of the water will interact with both the newly exposed Si-O bonds at the surface and the HF molecules, creating a positive feedback mechanism that increases the reaction rate [42], [56].

Most of the studies that involve chemical etching of latent ion tracks in SiO_2 have been conducted on amorphous SiO_2 substrates [42], [57]–[59]. These studies have demonstrated that wet-etching of amorphous SiO_2 produces conically shaped holes while vapor-etching produces more cylindrical-shaped holes [42], [43], [60], [61]. Holes with diameters of ~24 to ~80 nm have been documented with length/diameter ratios of up to 22 when vapor-etching with HF solutions varying acid concentration (4.5 - 48%w), etchant temperature (19°C - 28°C), and sample temperature (23°C - 47°C) [42].

One reason for the lack of knowledge on the chemical etching of ion tracks produced in α-SiO_2 is its complex crystal structure. It has been difficult to predict the result of α-SiO_2 etching with models based exclusively on theoretical assumptions. Experimental studies conducted so far include analysis of possible crystallographic planes and their etch rates for various etchants and the rate-controlling steps [46], [47], [62]–[64].

Additionally, previous studies reported that the etching rate of SiO_2 increases with HF concentration [46], [59], [62], [65]. The temperature-dependence of the etching rate in bulk SiO_2 has been reported as well [46], [53], [56]. Some of these studies included the analysis of etching rates when ion tracks are present [42], [43], [59], [62], [65], [66]. The etching rate of bulk SiO_2 rapidly decreases with increasing sample temperature (>60°C) [67]. Also, a previous study reported that the amount of oxygen removed decreases by more than two orders of magnitude when the sample temperature is increased from 25°C to 50°C for vapor from an azeotropic solution of HF/H_2O [58], [67]. Despite the decrease in etching rate with higher sample temperatures, one of these studies also reported

stronger preferential etching along ion tracks when the sample temperature is higher than the etchant temperature ($\Delta T \approx 10°C$ - $15°C$) [42].

The purpose of this work is to produce latent ion tracks in α-SiO_2 and subsequently etch nanowells by chemical vapor-etching using HF solutions. Different etching conditions were used to determine how etchant concentration, time, and ion species can control track dimension and morphology and can be used to tailor nanostructures. This manuscript describes the irradiation process, the ion track morphology, and their size distribution. An analysis of the etching process and its relation to crystal orientation is also discussed.

2. METHODOLOGY

Optical grade synthetic α-SiO_2 (Y-cut and Z-cut) single crystals were used in this study. The samples, purchased from MTI Corp., had dimensions of $1 \times 10 \times 10$ mm and were polished on one side. The different orientations were selected to better understand how ion track formation and the etching process are affected by crystallographic direction. Two different ion species at different energies were employed. Higher energies and heavier ions will produce more well-defined, continuous, and deeper tracks with homogeneous radii in accordance with the velocity effect. Therefore, a particular choice of ion species and energy may be selected in order to achieve a particular etched nanopore shape (e.g. with the desired aspect ratio, depth, superficial opening shape, regularity, etc.).

2.1. IRRADIATION CONDITIONS

21 samples of α-SiO_2 (9 Y-cut / 12 Z-cut) were irradiated under a vacuum of 5×10^{-5} Pa in the Ion Beam Materials Laboratory (IBML) at the University of Tennessee Knoxville (UTK) [68]. The irradiation process was conducted at room temperature with 20 MeV Ni^{6+} (0.34 MeV/amu) at nominal fluence values of 1×10^{9}, 1×10^{10}, and 1×10^{12} ions cm^{-2}. The fluence values were chosen to maintain a degree of track separation, from isolated (1×10^{9} ions cm^{-2}) to partially overlapping (1×10^{12} ions cm^{-2}) regime. To reach such low fluences accurately, the beam was defocused and rastered to achieve a low beam current on the order of picoamperes.

The ion beam current was measured using a Faraday cup placed under the sample holder and a picoammeter (Keithley Model 6485). The samples were tilted 5 degrees with respect to the incident ion beam to avoid ion channeling during irradiation. Adjustable beam slits were used to define an irradiation area of 10×10 mm^2 covering the entire sample surface. Beam homogeneity was verified to within 10% by measuring the spatial ion luminescence signal induced in a sample of amorphous silica using a 12-bit charge-coupled device (CCD) camera mounted on the end-station [69]. In addition, the current measured during irradiation through slits guarantees irradiation uniformity.

A second set of irradiations was conducted at the Centro de Microanálisis de Materiales - Universidad Autónoma de Madrid (CMAM-UAM) [70]. 30 samples of α-SiO_2 (15 samples for each orientation) were irradiated using 40 MeV I^{7+} (0.31 MeV/amu) under similar irradiation conditions used in the nickel irradiations (fluences: 1×10^{9}, 1×10^{10}, and 1×10^{11} ions cm^{-2}). Table 1 shows the experimental conditions for both

irradiation process including the nominal fluences and the effective distance between ion tracks estimated using $D_{tracks} = 1/\sqrt{\Phi}$, where Φ is the ion fluence.

The combination of ion species and energies were chosen based on the S_{Th}. S_{Th} for α-SiO_2 lies between 2 and 5 keV nm^{-1} [12], [34], [71]. The Stopping and Range of Ions in Matter (SRIM) code (version 2008) [72] was used to calculate the relevant irradiation parameters. The electronic stopping power in the surface region for 20 MeV Ni^{6+} ions in SiO_2 is 6.7 keV nm^{-1}, and the projected range is 6.7 μm. For the case of 40 MeV I^{7+} ions, the electronic stopping power in the surface region is 9.1 keV nm^{-1}, and the projected range is 8.1 μm. Figure 1 shows the nuclear energy loss, electronic energy loss, and the implanted ion concentration for both ions used in the irradiations.

Table 1. Experimental conditions for the irradiation processes with different ions

	20 MeV – Ni^{6+} ion irradiation			40 MeV – I^{7+} ion irradiation		
Nominal Fluence (cm^{-2})	1×10^{9}	1×10^{10}	1×10^{12}	1×10^{9}	1×10^{10}	1×10^{11}
Flux ($cm^{-2}s^{-1}$)	2.2×10^{8}	5.8×10^{8}	3.5×10^{10}	1.3×10^{8}	1.5×10^{8}	2.2×10^{8}
D_{tracks} (nm)	316.2	100.0	10.0	316.2	100.0	31.6
I (nA)	0.2	0.5	3.0	15.0	17.0	25.0
Δt (s)	4.5	17.3	28.8	8.0	66.0	449.0

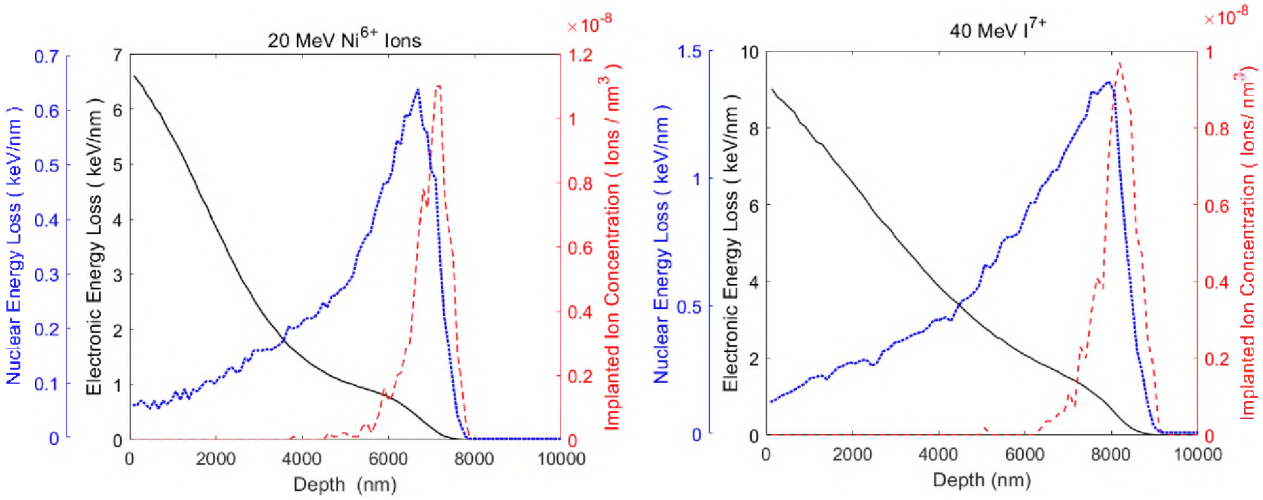

Figure 1. SRIM simulation for the ions and energies used in the irradiations

2.2. ETCHING CONDITIONS

The ion irradiated samples of the present work were chemical vapor etched with HF solutions at different etching times and etchant concentrations (10%w HF, 20%w HF, and 30%w HF). Some experiments included the variation of etchant temperature to evaluate the effect of the temperature on the production of nanowells. It was found that higher acid temperatures dramatically increased the etching rate, making it difficult to control the etching process. High roughness was observed even at low acid concentrations (10%w HF) and short etching times (30 seconds). Therefore, subsequent etching processes were conducted with the HF acid at room temperature while the concentration and etching time were varied. The results reported in this study include just the etching process conducted with the samples and the acid at room temperature.

All samples were cleaned with isopropyl alcohol and deionized water before etching. The homemade experimental setup consists of a high-density polyethylene container with a

sample holder attached to the lid. The sample holder suspends the surface of the α-SiO_2 sample 1 cm above from the etchant solution, with the irradiated side facing down. The holder was designed to expose all irradiated areas to the etchant, avoiding undesirable condensation by contact on the surface of interest.

2.3. ATOMIC FORCE MICROSCOPY

A Digital Instruments Nanoscope IIIa Atomic Force Microscope was used to examine the surface of the irradiated samples. The AFM measurements were performed at room temperature using hard tapping mode. Two different AFM silicon probes (from AppNano), with a reflex side of aluminum, were used. The first type has a tip with a tetrahedral shape and radius of curvature of 6 nm. This type of probes has a high resonance frequency (300 kHz) for high-speed scanning in tapping mode. The second type of probes was used to analyze the depth of the obtained etched nanowells. These tips had a pyramidal shape with high aspect ratio tips, 2 μm long spike, with no tilt compensation. The radius of curvature was 20 nm. It is important to note that the tip shape and radius of curvature affect the measurement [73], [74], a larger radius will reduce the resolution. However, the high aspect ratio allowed to get acquired measurements of nanowell depths. The Full Width at Half Maximum (FWHM) and the height of the hillocks created by the ions were measured. AFM measurements of the unirradiated samples were taken for comparison purposes.

The AFM imaging conditions for all samples were as follows: the images sizes range from 0.8 μm^2 to 5 μm^2, with a scan speed of 1–1.97 Hz, and 512 points per line. These parameters allowed a digital resolution up to 10 nm $pixel^{-1}$. The integral and

proportional gains were set at 0.4. Drive frequency was set around 310 kHz with a drive amplitude of approximately 357 mV. The amplitude set point was 2.75 V. Second-order flattening was used to correct for image bow caused by the piezoelectric scanner non-linearity. This correction does not affect features much smaller than the image size; therefore, it does not significantly affect the quantitative measurement of the hillock features on the irradiated surface.

3. RESULTS AND DISCUSSION

3.1. FORMATION AND CHARACTERIZATION OF ION TRACKS

The formation of ion tracks in α-SiO_2, at different crystal orientations, was successfully accomplished by irradiating with both 20 MeV Ni^{6+} ions and 40 MeV I^{+7} ions, using different fluences. The AFM measurements show the presence of hillocks at the surface of all samples analyzed. The actual fluence was found to be in reasonable agreement with the nominal fluence (within about half order of magnitude) by counting the number of hillocks found in the AFM micrographs. Figure 2 shows the α-SiO_2 surfaces of Z-cut samples after irradiation with 20 MeV Ni^{6+} at different fluences. As one can see, the surface modification by the presence of the hillocks increases with ion fluence. The samples irradiated at higher fluences (1×10^{11} ions cm^{-2} for 40 MeV I^{7+}, and 1×10^{12} ions cm^{-2} for 20 MeV Ni^{6+}) showed a high degree of track overlapping that complicated the quantitative characterization of the hillocks. A similar situation was observed after etching these highly irradiated samples. Due to the high degree of track overlapping, it was not possible to observe individual nanowells above a fluence of

1×10^{10} ions cm^{-2}. For illustration purposes, Figure 3 shows a Y-cut sample that was irradiated with 40 MeV I^{7+} to a fluence of 1×10^{11} ions cm^{-2} and a Z-cut sample irradiated with 20 MeV Ni^{6+} to a fluence of 1×10^{12} ions cm^{-2}. Both samples were etched for 10 minutes with 10% HF at room temperature. Henceforth, the analysis conducted for the latent ion tracks and etched nanowells will include the results obtained from samples irradiated at the two lower fluences (1×10^{9} and 1×10^{10} ions cm^{-2}) paying particular attention to the etching process of samples irradiated to 1×10^{9} ions cm^{-2}. Figure 4 shows AFM images of an unirradiated α-SiO_2 surface in the Z-cut direction (A), the hillocks produced at the same sample surface after being irradiated with 1×10^{9} cm^{-2} 40 MeV I^{7+} ions (B), its 3D-surface view (C), and the section analysis of the ion tracks found in the analyzed area (D).

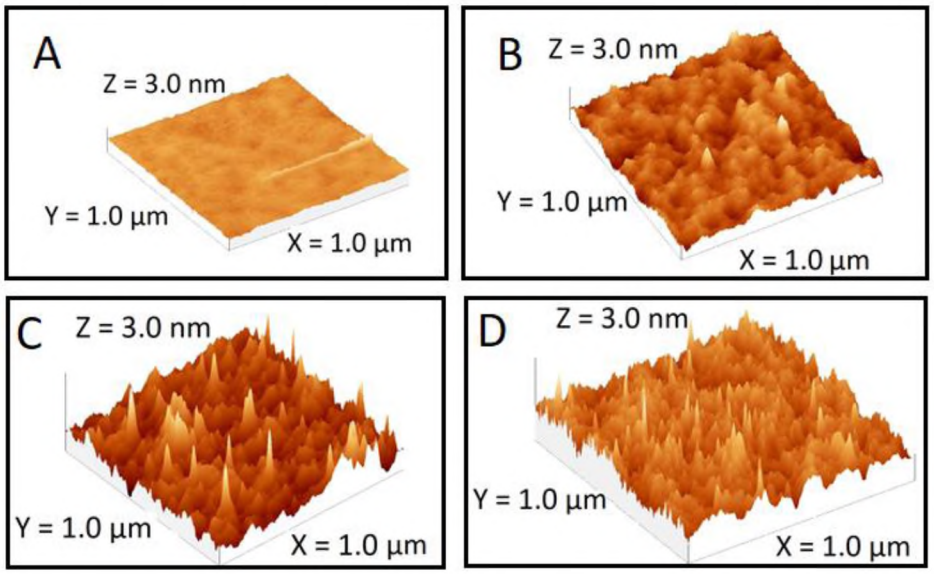

Figure 2. Surfaces of Z-cut samples. (A) Unirradiated, and after been irradiated with 20 MeV Ni^{6+} at (B) 1×10^{9}ions cm^{-2}, (C) 1×10^{10}ions cm^{-2}, and (D) 1×10^{12} ions cm^{-2}

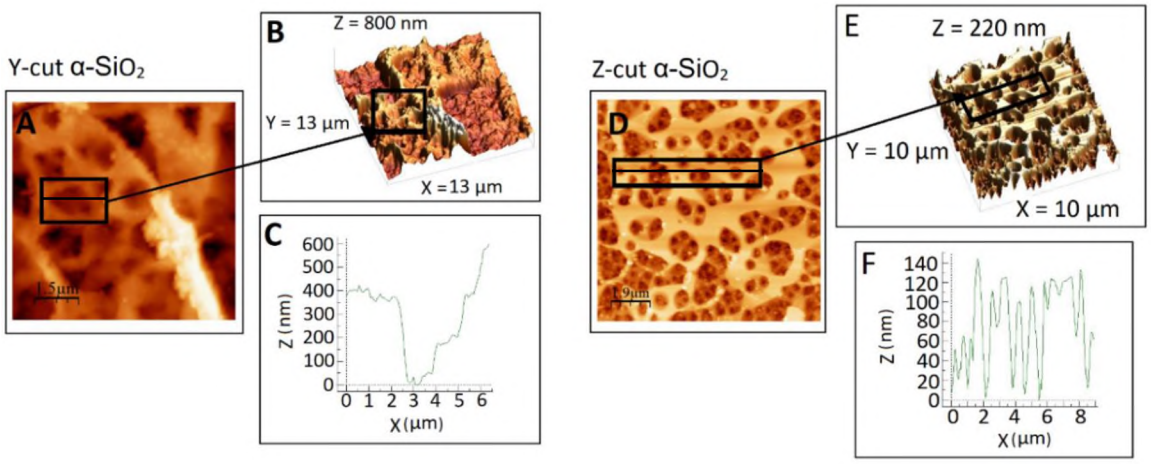

Figure 3. Etched samples with 10% HF for 10 minutes at room temperature. Y-cut sample irradiated with 40 MeV I^{7+} at 1×10^{11} ions cm^{-2} (A), etched sample surface (B), 3D-surface analysis, and (C) the section analysis of the nanowells found in the selected area. Z-cut sample irradiated with 20 MeV Ni^{6+} at 1×10^{12} ions cm^{-2} (D), etched sample surface (E), 3D-surface analysis, and (F) the section analysis of the nanowells found in the selected area

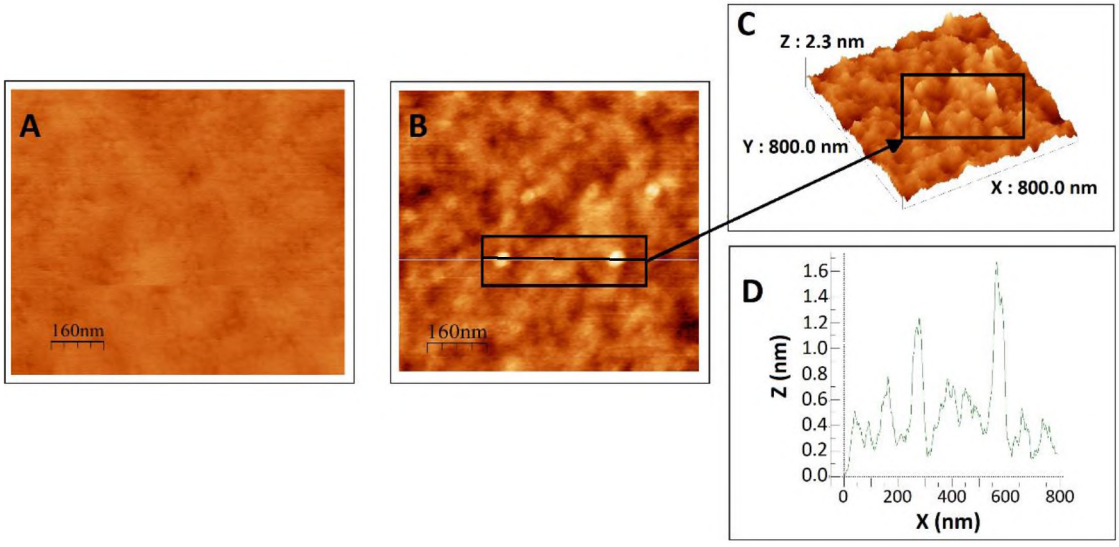

Figure 4. AFM images of a Z-cut α-SiO_2 before and after being irradiated. (A) Unirradiated surface. (B) Irradiated surface with 40 MeV I^{7+} ion at 1×10^{9} cm^{-2}. (C) 3D-surface analysis of the irradiated surface and (D) the section analysis of the hillocks found in the selected area

From AFM image analysis, it was found that the hillocks have similar dimensions (height and FWHM) in both crystal orientations. Table 2 shows the mean and standard error values for the hillock heights and FWHMs obtained after the irradiation with each ion at different fluences. For the analysis, 60 hillocks from each sample were measured.

Table 2. Height, FWHM, and standard error of ion track hillocks

Ion	Crystal orientation	Fluence (ion cm^{-2})	Ave. Height (nm)	Ave. FWHM (nm)
20 MeV Ni^{6+}	Z-cut	1×10^{9}	1.58 ± 0.10	29.6 ± 1.1
		1×10^{10}	1.38 ± 0.04	28.9 ± 0.9
	Y-cut	1×10^{9}	1.34 ± 0.09	27.7 ± 1.2
		1×10^{10}	1.24 ± 0.06	27.2 ± 1.1
40 MeV I^{7+}	Z-cut	1×10^{9}	1.09 ± 0.04	26.7 ± 0.9
		1×10^{10}	1.22 ± 0.06	25.6 ± 0.8
	Y-cut	1×10^{9}	1.00 ± 0.03	24.8 ± 1.1
		1×10^{10}	1.14 ± 0.02	24.4 ± 0.7

It was found that samples irradiated with 20 MeV Ni^{6+} produced slightly higher (97% confidence) and broader (99% confidence) hillocks. This observation is ascribed to the difference in length of the produced ion track and the deposited energy density, which affect the resulting macroscopic swelling creating hillocks with different dimensions.

Even when the ions had similar specific energy (0.34 MeV/amu for Ni^{6+} and 0.31 MeV/amu for I^{7+}), irradiating with 40 MeV I^{7+} presented a higher S_e value (ΔS_e = 2.4 keV nm^{-1}), inducing a larger but lower density radial distribution of energy deposited

onto the electronic structure, and resulting in deeper tracks with smaller diameters which can be related with a lower swelling effect and smaller hillocks. The obtained results are in agreement with previous studies [16], [75]. Z-cut samples had slightly larger hillocks on average. This may be due to the anisotropic nature of the material. It should be mentioned, however, that the difference was statistically weaker (77% confidence on the FWHM). However, the effect is still plausible as it has been observed in other materials such as lithium niobate where crystal symmetry plays an important role in hillock morphology evolution due to the crystal-dependence on strain around the tracks and due to the energy and mass of the ions [76], [77].

3.2. FORMATION AND CHARACTERIZATION OF NANOWELLS

The production of nanowells by HF-vapor etching of the irradiated samples was successfully achieved with different acid concentrations. As expected, it was found that both the nanowell superficial dimensions and depths increase with longer etching time and higher acid concentration. However, the Z-cut samples showed a higher sensitivity to the acid with a faster etch rate than the Y-cut samples. Previous studies have discussed the anisotropic etching behavior of quartz [46]–[48], [64], [67].

3.2.1. Effect of Crystal Orientation on the Etching Rate. Figure 5 shows AFM images of sample surfaces that were etched at different etching times and acid concentrations. These images include AFM measurements of Y-cut and at Z-cut samples that were irradiated with 20 MeV Ni^{6+} ions to a fluence of 1×10^{9} cm^{-2}. The Z-cut sample that was etched with 20%w HF for 1 minute at room temperature and exhibits conical

features that likely etch outward from the ion tracks. The selected area shows a well isolated conical feature with dimensions of 400 nm diameter and 50 nm depth.

Presumably, the sponge-like features are formed when more closely separated conical wells merge with each other. The Avrami model with an effective particle diameter of 400 nm and areal density of 1×10^{9} cm^{-2} predicts that 72% of the surface should be covered with overlapping wells, which is in qualitative agreement with Figure 5. The Y-cut sample was etched with a more concentrated acid for a longer time (30% HF for 15 minutes). The surface obtained had nanowells with pyramidal-shaped nanopores and faceted diameters around 80 nm in width with depths of < 30 nm. In addition, etching of unirradiated samples was conducted to compare the damage caused at the surface when no ion tracks are present. Etching conditions were similar to those used on the irradiated samples. It was found that the unirradiated surfaces became slightly rougher after etching (average roughness 0.4 nm). However, it was not possible to find nanostructures at the sample surface with comparable geometry and dimensions to those of the etched irradiated samples. Figure 5 also includes the AFM images of an unirradiated Y-cut sample that was etched with 20%w HF for 10 minutes.

In order to produce isolated nanowells in the Z-cut samples, it is necessary to conduct the etching process with a lower concentration. From this point forward, the results shown for etched Z-cut samples include samples etched with 10%w HF for up to 10 minutes. After 10 min, the agglomerated nanowell features appear. Figure 6 shows the depths and superficial diameters of nanowells obtained in Z-cut samples after etching with 10%w HF. AFM images of a Z-cut sample, irradiated with $1x10^{9}$ - 20 MeV Ni^{6+} and etched with 10%w HF for 10 minutes are also included. It was found that the etching rate

was fast during the first minute (diameter ≈ 68 ± 7 nm min^{-1}, depth ≈ 3.1 ± 0.3 nm min^{-1} for samples irradiated with Ni^{6+}, diameter ≈ 60.2 ± 8.2 nm min^{-1}, depth ≈ 4.9 ± 0.3 nm min^{-1} for samples irradiated with I^{7+}). After one minute of etching, the rate decreases significantly (diameter ≈ 14 ± 3 nm min^{-1}, depth ≈ 0.9 ± 0.1 nm min^{-1} for samples irradiated with Ni^{6+}, diameter ≈ 12.2 ± 1.3 nm min^{-1}, depth ≈ 1.34 ± 0.02 nm min^{-1} for samples irradiated with I^{7+}).

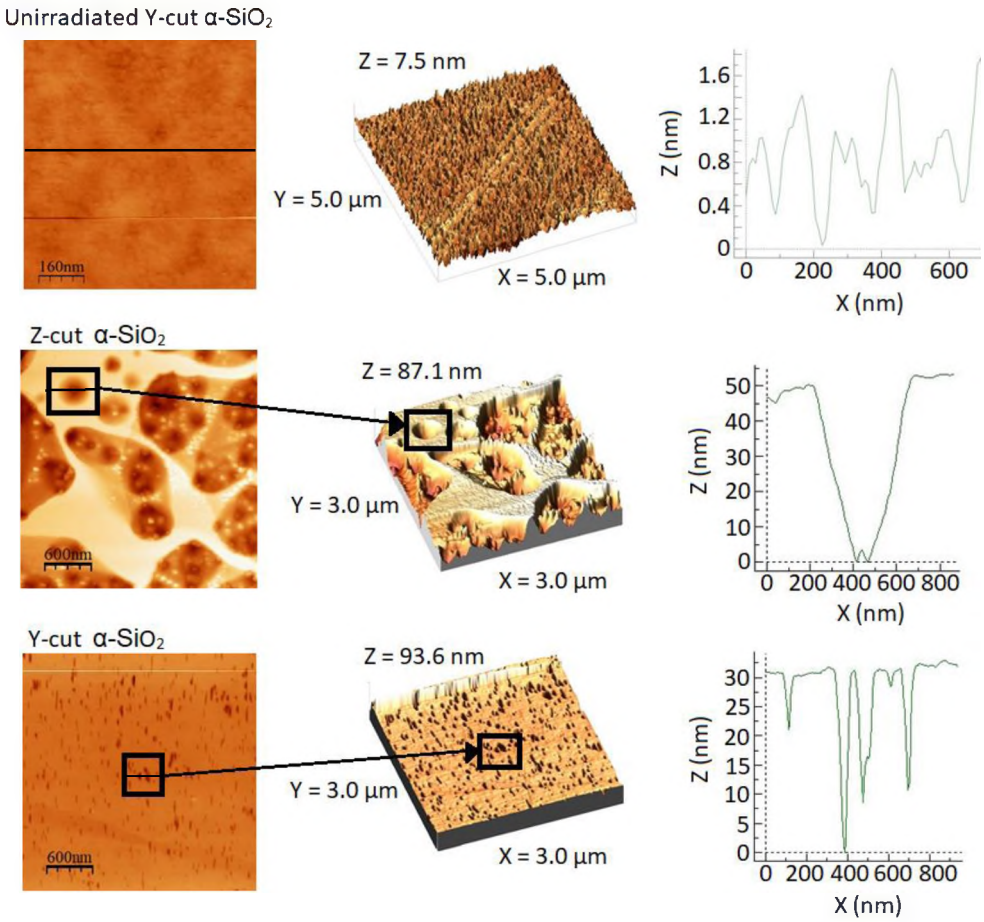

Figure 5. AFM images for etched α-SiO_2 samples. (top) unirradiated Y-cut sample (etched with 20%w HF for 10 minutes), (middle) an irradiated Z-cut sample (20 MeV Ni^{6+} at 1×10^9 cm^{-2}- etched with 20%w HF for 1 minute), and (bottom) an irradiated Y-cut α-SiO2 sample (20 MeV Ni^{6+} at 1×10^9 cm^{-2} - etched with 30%w HF for 15 minutes)

This behavior suggests that two different kinetic regimes may be present. In the initial fast regime, the hillocks and ion track cores etch at a faster rate than the rest of the sample surface. The fast etching rate can be related to the high density of crystal defects along the ion tracks. After removing the hillocks from the surface and forming the nanowells, the etching rates slow. The decrease in the etching rate could be due to the increase in the ratio of the surface area of the crystalline to amorphous regions. It may also be indicative of differences between the near-surface track structure, density, and strain. Table 3 shows the nanowell aspect ratio (depth/width), surface nanowell diameter etching rate, and nanowell depth etching rate obtained for the Z-cut samples.

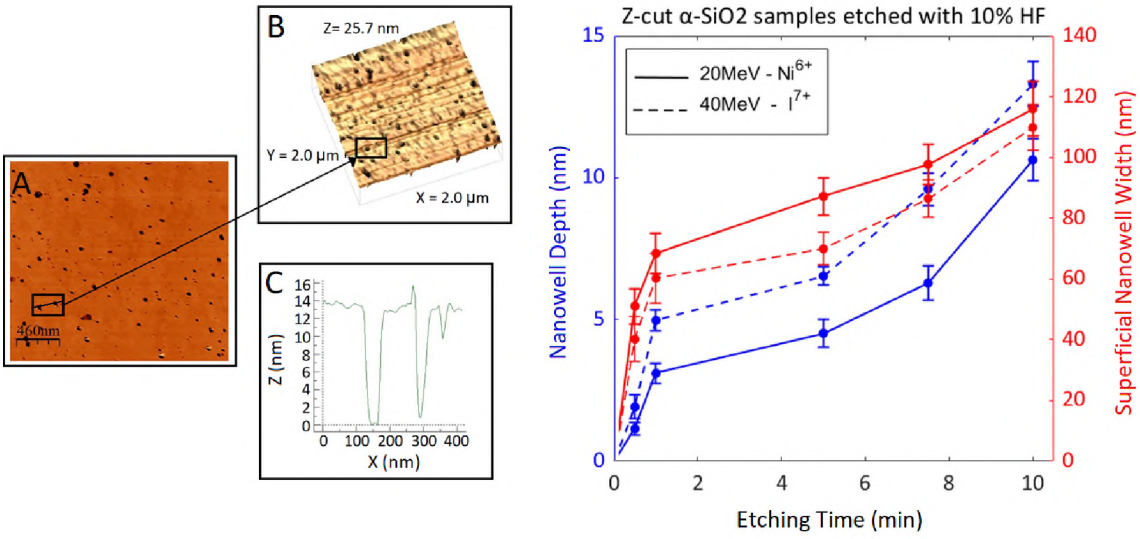

Figure 6. (Left) AFM images of a Z-cut α-SiO2 irradiated with 20 MeV Ni^{6+} at 1×10^{9} ions cm^{-2}, and etched with 10%w HF for 10 minutes. (A) etched sample surface, (B) 3D-surface analysis, and (C) the section analysis of the ion tracks found in the selected area. (Right) Depth and superficial diameter of nanowells in Z-cut samples that were etched with 10% HF

Table 3. Pore aspect ratio, surface nanowell diameter etching rate, and nanowell depth etching rate obtained for the Z-cut samples etched with 10% HF after 1 minute

		Etching rates (nm min^{-1})	
Ion	Pore Aspect ratio	Diameter	Depth
20 MeV Ni^{6+}	< 0.09	14.0 ± 2.4	0.9 ± 0.1
40 MeV I^{7+}	< 0.12	12.2 ± 1.3	1.30 ± 0.03

The AFM analysis conducted on the etched Y-cut samples exhibited lower etching rates. Nanowells could be produced with less modification of the crystal surface. Due to the lower reactivity of the surface, it was possible to conduct the etching process with higher acid concentrations (10%, 20%, and 30% HF) for up to 2 hours. However, after 1 hour of etching with 30% HF, the surface became highly damaged making subsequent image analysis difficult. Therefore, all etched samples were quantitatively analyzed up to 1 hour of etching.

3.2.2. Anisotropic Behavior in the Etching of Y-cut Samples. Anisotropic behavior in the etching process was found after 15 minutes of etching. During the first 15 minutes, the nanowells appeared as lenticular-shaped features at the surface. After 15 minutes, the nanowells began to elongate in the Z-direction transforming the nanowells into nanochannel structures. Figure 7 shows the anisotropic behavior of the etching process conducted on Y-cut samples irradiated with 40 MeV I^{7+} and etched with 20% HF at different etching times of 10 minutes (A), 30 minutes (B), and 60 minutes (C). The superficial XZ aspect ratios were found to increase linearly with etching time and were 0.8 ± 0.2, 2.8 ± 1.3, and 4.8 ± 2.0, respectively.

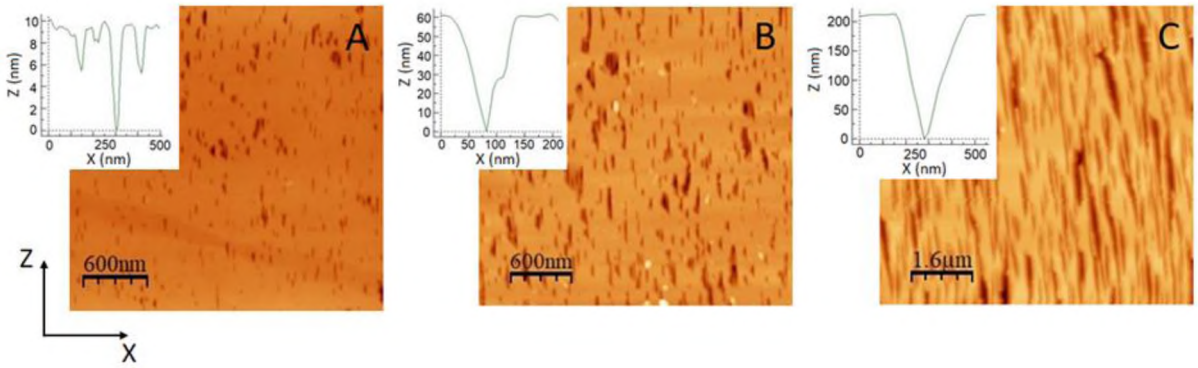

Figure 7. Anisotropic behavior revealed by the etching process on Y-cut samples irradiated with 40 MeV I^{7+} and etched with 20% HF at different etching times: (A) 10 minutes, (B) 30 minutes, and (C) 60 minutes

Figure 8 shows the superficial dimensions (length and width) and the depths of the nanowells in Y-cut samples. The etching rates were slower than those of the Z-cut samples (~50% slower for width/diameter, 15% - 60% slower for depths), even when using high etchant concentrations (30% HF). Table 4 shows the etching rate values in nm min^{-1} during the fast regime (first 20 minutes of etching). As shown in Table 4, the etching rate at the sample surface along the Z direction (nanowell length) is faster than the etching rate along the X direction (width) favoring the production of nanochannels at higher acid concentrations.

Three different kinetic regimes of the etching process were observed in the Y-cut samples. The first regime was observed for the first 20 minutes of etching, after which the etching rate decreases significantly. After about 40 minutes of etching, the nanowells began to agglomerate creating the nanochannels at the sample surface. At about this time the etching rate increased.

Table 4. Etching rate for superficial dimensions and depths of the obtained nanowells in Y-cut samples when etching with HF at different concentrations

Acid concentration	Ion	Length (Z direction) (nm min^{-1})	Width (X direction) (nm min^{-1})	Depth (Y direction) (nm min^{-1})
10%w	20 MeV Ni^{6+}	2.7 ± 0.9	2.1 ± 0.9	0.3 ± 0.1
	40 MeV I^{7+}	2.0 ± 0.6	2.0 ± 0.6	0.5 ± 0.1
20%w	20 MeV Ni^{6+}	11.4 ± 4.1	5.3 ± 0.8	1.4 ± 0.4
	40 MeV I^{7+}	9.8 ± 4.1	4.0 ± 0.7	3.0 ± 1.5
30%w	20 MeV Ni^{6+}	28.5 ± 9.5	6.4 ± 0.9	2.1 ± 0.5
	40 MeV I^{7+}	27.0 ± 9.5	5.0 ± 0.4	5.0 ± 3.3

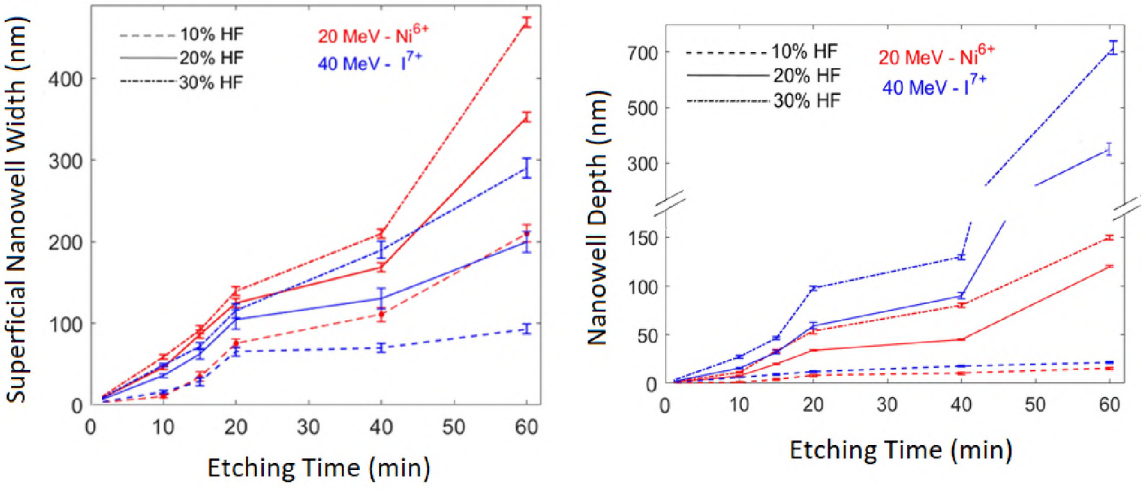

Figure 8. Superficial width and depth of etched tracks in Y-cut samples

The increase in etching rate is probably due to the enhanced transport of HF into and through the agglomerated channel structure. It was possible to obtain nanowells with ~700 nm depth with the samples irradiated with 40 MeV I^{7+} and etched with 30% HF.

The depth aspect ratios (depth/superficial width) of nanowells obtained at different irradiation conditions and different etchant concentrations are shown in Table 5.

Table 5. Aspect ratios of obtained nanowells at different acid concentrations for samples irradiated with both energetic ions

	10% HF	20% HF	30% HF
20 MeV Ni^{6+}	$< 0.12 \pm 0.01$	$< 0.34 \pm 0.01$	$< 0.39 \pm 0.01$
40 MeV I^{7+}	$< 0.40 \pm 0.01$	$< 1.75 \pm 0.01$	$< 2.41 \pm 0.01$

All samples irradiated with 40 MeV I^{7+} had deeper nanowells with smaller diameters than samples irradiated with 20 MeV Ni^{6+} which had shallow nanowells with wider diameters. The difference in aspect ratio is consistent with the ion velocity effect. For a given nanowell depth, a higher aspect ratio could be achieved with a more concentrated etchant. This suggests that the adsorption of HF onto the surface may be a rate-limiting step. With these findings, it appears there are parameters that could be used to design and tailor nanowell templates. Such templates could be used in novel nanodevices and to functionalize the surface of quartz thereby enhancing its thermal, optical, and dielectric properties, among others.

4. CONCLUSIONS

The production of latent ion tracks in α-SiO_2 and subsequent formation of nanowells by chemical HF-vapor etching was systematically studied. Irradiating quartz with both 20 MeV Ni^{6+} ions and 40 MeV I^{+7} ions produced continuous and homogeneous ion tracks. After irradiating, it was possible to observe hillocks at the sample surface as a consequence of the amorphization process. Hillocks of similar height and FWHM were observed in both Y- and Z-cut samples. The hillock morphology depends on the ion velocity. Samples irradiated with 20 MeV Ni^{6+} had broader hillocks and presumably wider tracks. Samples irradiated with 40 MeV I^{+7} ions produced deeper ion tracks with smaller diameters.

Upon etching, it was found that Z-cut samples etched at faster rates. Low acid concentrations (<10% HF) were needed to conduct an etching process with controllable etching time and without damaging the surface of the samples. Under those etching conditions, it was possible to obtain conical-shaped nanowells with superficial dimensions up to ~140 nm with and depths of around ~15 nm.

In the etched, Y-cut samples, strong anisotropic etching was revealed. Nanowells produced during the first 15 minutes were roughly lenticular in shape. After longer etching times, the nanowells began to elongate in the Z direction, eventually agglomerating into nanochannels.

Different kinetic regimes were identified in all etched samples. Initially, the etching process is rapid and occurs primarily along the track core. This is followed by a slower regime where the growth of the superficial dimension(s) increases. For Y-cut

quartz, a third, fast etching regime was also observed where the agglomeration of channels creates a relatively open structure that may improve HF transport. The ion velocity effect is believed to explain differences in the nanowell aspect ratio. Samples that were irradiated with 20 MeV Ni^{6+} ions presented shallower nanowells with broader diameters than those irradiated with 40 MeV I^{+7}. Higher aspect ratios could also be achieved at higher etchant concentrations. Through the right choice of irradiation parameters (i.e. ion mass and energy) as well as a choice of etchant and crystallographic orientation, it may be possible to further optimize the etching process to design and tailor nanowell templates. Functionalizing such templates may prove to be an effective route to developing novel optical, electronic, and thermal metamaterials.

ACKNOWLEDGMENTS

This work was supported by the Nuclear Regulatory Commission Faculty Development Grant NRC-HQ-84-15-G-0044. M.L.C. acknowledges support from the University of Tennessee Governor's Chair program. The authors are grateful to the staff in The Centro de Microanálisis de Materiales - Universidad Autónoma de Madrid for assistance with experimental irradiations. Also, the authors want to thank the Materials Research Center (MRC) at Missouri S&T for its support and use of equipment. J. O. acknowledges the projects TechnofusionIII (S2018/EMT-4437) from Comunidad de Madrid and EU COST Action CA17126.

REFERENCES

[1] Y. Z. R. Hellborg, H.J. Whitlow, Ion Beams in Nanoscale and Technology. 2009.

[2] W. J. Weber, D. M. Duffy, L. Thomé, and Y. Zhang, "The role of electronic energy loss in ion beam modification of materials," *Curr. Opin. Solid State Mater. Sci.*, vol. 19, no. 1, pp. 1–11, 2015, doi: 10.1016/j.cossms.2014.09.003.

[3] J. Li, D. Stein, C. Mcmullan, and D. Branton, "Ion-beam sculpting at nanometre length scales," *Nature*, vol. 412, no. 6843, pp. 166–169, 2001.

[4] Y. Shimotsuma, J. Qiu, P. G. Kazansky, and K. Hirao, "Nano-Modification Inside Transparent Materials by Femtosecond Laser Single," *Mod. Phys. Lett. B*, vol. 19, no. 05, pp. 225–238, 2005, doi: 10.1142/S0217984905008281.

[5] K. linga Murty and I. Charit, *An introduction to nuclear materials: fundamentals and applications*, Illustrate. John Wiley & Sons, 2013, 2013.

[6] L. K. Mansur, A. F. Rowcliffe, R. K. Nanstad, S. J. Zinkle, W. R. Corwin, and R. E. Stoller, "Materials needs for fusion, Generation IV fission reactors and spallation neutron sources - Similarities and differences," in *Journal of Nuclear Materials*, 2004, doi: 10.1016/j.jnucmat.2004.04.016.

[7] G. García, A. Rivera, M. L. Crespillo, N. Gordillo, J. Olivares, and F. Agulló-López, "Amorphization kinetics under swift heavy ion irradiation: A cumulative overlapping-track approach," *Nucl. Instruments Methods Phys. Res. Sect. B Beam Interact. with Mater. Atoms*, vol. 269, no. 4, pp. 492–497, 2011, doi: 10.1016/j.nimb.2010.12.073.

[8] N. L. Singh, S. Shah, A. Qureshi, F. Singh, D. K. Avasthi, and V. Ganesan, "Swift heavy ion induced modification in dielectric and microhardness properties of polymer composites," *Polym. Degrad. Stab.*, vol. 93, no. 6, pp. 1088–1093, 2008, doi: 10.1016/j.polymdegradstab.2008.03.015.

[9] R. A. B. Devine, "Ion implantation- and radiation-induced structural modifications in amorphous SiO 2," vol. 152, pp. 50–58, 1993.

[10] Á. R. Páramo *et al.*, "Mechanical response to swift ion irradiation-induced nano-tracks in silica," *Nucl. Instruments Methods Phys. Res. Sect. B Beam Interact. with Mater. Atoms*, vol. 352, pp. 145–147, 2015, doi: 10.1016/j.nimb.2014.12.073.

[11] J. Manzano, J. Olivares, F. Agulló-López, M. L. Crespillo, A. Moroño, and E. Hodgson, "Optical waveguides obtained by swift-ion irradiation on silica (a-SiO 2)," *Nucl. Instruments Methods Phys. Res. Sect. B Beam Interact. with Mater. Atoms*, vol. 268, no. 19, pp. 3147–3150, 2010, doi: 10.1016/j.nimb.2010.05.075.

[12] N. Itoh, D. M. Duffy, S. Khakshouri, and A. M. Stoneham, "Making tracks: Electronic excitation roles in forming swift heavy ion tracks," *J. Phys. Condens. Matter*, vol. 21, no. 47, 2009, doi: 10.1088/0953-8984/21/47/474205.

[13] E. C. H. Silk and R. S. Barnes, "Examination of fission fragment tracks with an electron microscope," *Philos. Mag.*, vol. 4, no. 44, pp. 970–972, 1959, doi: 10.1080/14786435908238273.

[14] M. Lang, R. Devanathan, M. Toulemonde, and C. Trautmann, "Advances in understanding of swift heavy-ion tracks in complex ceramics," *Curr. Opin. Solid State Mater. Sci.*, vol. 19, no. 1, pp. 39–48, 2015, doi: 10.1016/j.cossms.2014.10.002.

[15] M. Toulemonde, C. Trautmann, E. Balanzat, K. Hjort, and A. Weidinger, "Track formation and fabrication of nanostructures with MeV-ion beams," *Nucl. Instruments Methods Phys. Res. Sect. B Beam Interact. with Mater. Atoms*, vol. 216, no. 1–4, pp. 1–8, 2004, doi: 10.1016/j.nimb.2003.11.013.

[16] A. Meftah *et al.*, "Track formation in SiO2 quartz and the thermal-spike mechanism," *Phys. Rev. B*, vol. 49, no. 18, pp. 12457–12463, 1994, doi: 10.1103/PhysRevB.49.12457.

[17] J. Provost *et al.*, "Swift, Heavy Ions in Insulating and Conducting Oxides: Tracks and Physical Properties," *MRS Bull.*, vol. 20, no. 12, pp. 22–28, 1995, doi: 10.1557/S0883769400045863.

[18] A. Rivera *et al.*, "Permanent modifications in silica produced by ion-induced high electronic excitation: Experiments and atomistic simulations," *Sci. Rep.*, vol. 7, no. 1, pp. 1–14, 2017, doi: 10.1038/s41598-017-11182-4.

[19] A. Meftah *et al.*, "Swift heavy ions in magnetic insulators: A damage-cross-section velocity effect," *Phys. Rev. B*, vol. 48, no. 2, p. 920, 1993, doi: 10.1103/PhysRevB.48.920.

[20] Spohr and Reimar, *Ion tracks and microtechnology: principles and applications*, 1st ed. Frankfurt: Vieweg+Teubner Verlag, 1990.

[21] C. Trautmann, "Micro-and nanoengineering with ion tracks," in *Ion Beams in Nanoscience and Technology*, R. Hellborg, H. Whitlow, and Y. Zhang, Eds. Berlin: Springer, Berlin, Heidelberg, 2009, pp. 369–387.

[22] M. E. Toimil-Molares, "Characterization and properties of micro- and nanowires of controlled size, composition, and geometry fabricated by electrodeposition and ion-track technology," *Beilstein J. Nanotechnol.*, vol. 3, no. 1, pp. 860–883, 2012, doi: 10.3762/bjnano.3.97.

[23] A. Weidinger, "Ion tracks - a new route to nanotechnology," *Europhys. News*, vol. 35, no. 5, pp. 152–155, 2004.

[24] D. Schauries *et al.*, "Temperature dependence of ion track formation in quartz and apatite," *J. Appl. Crystallogr.*, vol. 46, no. 6, pp. 1558–1563, 2013, doi: 10.1107/S0021889813022802.

[25] J. Manzano-Santamaría, J. Olivares, A. Rivera, and F. Agulló-López, "Electronic damage in quartz (c-SiO 2) by MeV ion irradiations: Potentiality for optical waveguiding applications," *Nucl. Instruments Methods Phys. Res. Sect. B Beam Interact. with Mater. Atoms*, vol. 272, pp. 271–274, 2012, doi: 10.1016/j.nimb.2011.01.081.

[26] W. Primak, L. H. Fuchs, and P. Day, "Effects of Nuclear Reactor Exposure on Some Properties of Vitreous Silica and Quartz," *Am. Ceram. Soc.*, vol. 38, no. 4, pp. 135–139, 1955, doi: https://doi.org/10.1111/j.1151-2916.1955.tb14916.x.

[27] A. Benyagoub, S. Löffler, M. Rammensee, S. Klaumünzer, and G. Saemann-Ischenko, "Plastic deformation in SiO2 induced by heavy-ion irradiation," *Nucl. Inst. Methods Phys. Res. B*, vol. 65, no. 1–4, pp. 228–231, 1992, doi: 10.1016/0168-583X(92)95039-T.

[28] H. Fischer, G. Götz, and H. Karge, "Radiation damage in ion-implanted quartz crystals. Part I: Nuclear and electronic energy deposition. Title," *Phys. status solidi*, vol. 76, no. 1, 1983, doi: https://doi.org/10.1002/pssa.2210760129.

[29] F. A. Cucinotta, R. Katz, and J. W. Wilson, "Heavy ion track-structure calculations for radial dose in arbitrary materials," *Robert Katz ...*, no. February, 1995, [Online]. Available: http://digitalcommons.unl.edu/cgi/viewcontent.cgi?article=1003&context=physics katz%5Cnpapers3://publication/uuid/1F421F7E-C169-488C-B570-0E75E73F51CF.

[30] D. Schauries, B. Afra, M. D. Rodriguez, C. Trautmann, A. Hawley, and P. Kluth, "Ion track annealing in quartz investigated by small angle X-ray scattering," *Nucl. Instruments Methods Phys. Res. Sect. B Beam Interact. with Mater. Atoms*, vol. 365, pp. 380–383, 2015, doi: 10.1016/j.nimb.2015.07.081.

[31] R. L. Fleisher, P. B. Price, and R. M. Walker, *Nuclear tracks in solids: Principles and applications*. Berkeley California: Univ of California Press, 1975.

[32] B. Wang, Y. Yu, I. Pignatelli, G. Sant, and M. Bauchy, "Nature of radiation-induced defects in quartz," *J. Chem. Phys.*, vol. 143, no. 2, 2015, doi: 10.1063/1.4926527.

[33] R. G. Macaulay-Newcombe and D. A. Thompson, "Ion bombardment damage in α-quartz at 50–295 K," *Nucl. Instruments Methods Phys. Res. Sect. B Beam Interact. with Mater. Atoms*, vol. 1, no. 2–3, pp. 176–182, 1984.

[34] S. Klaumünzer, "Ion tracks in quartz and vitreous silica," *Nucl. Instruments Methods Phys. Res. Sect. B Beam Interact. with Mater. Atoms*, vol. 225, no. 1-2 SPEC. ISS., pp. 136–153, 2004, doi: 10.1016/j.nimb.2004.05.014.

[35] D. M. Follstaedt, A. K. Norman, B. L. Doyle, and F. D. McDaniel, "Strain fields around high-energy ion tracks in α-quartz," *J. Appl. Phys.*, vol. 100, no. 6, 2006, doi: 10.1063/1.2345029.

[36] C. L. Phillips, R. J. Magyar, and P. S. Crozier, "A two-temperature model of radiation damage in α -quartz," *J. Chem. Phys.*, vol. 133, no. 14, 2010, doi: 10.1063/1.3481356.

[37] U. Utzinger and R. R. Richards-Kortum, "Fiber optic probes for biomedical optical spectroscopy," *J. Biomed. Opt.*, vol. 8, no. 1, p. 121, 2003, doi: 10.1117/1.1528207.

[38] F. P. Bolin, L. E. Preuss, R. C. Taylor, and R. J. Ference, "Refractive index of some mammalian tissues using a fiber optic cladding method," *Appl. Opt.*, vol. 28, no. 12, pp. 2297–2303, 1989.

[39] C. Stambaugh, H. Shakeel, D. Kalteyer, P. Abbott, and J. Pomeroy, "Traceability of frequency based mass measurements using a quartz crystal microbalance," *J. Phys. Conf. Ser.*, vol. 1065, no. 4, 2018, doi: 10.1088/1742-6596/1065/4/042002.

[40] M. Blomqvist, O. Blomster, M. Palsson, S. Campbell, F. Becker, and W. Rath, "All-in-quartz optics for low focal shifts," in *Proceedings Volume 7912, Solid State Lasers XX: Technology and Devices*, 2011, doi: 10.1117/12.874597.

[41] C. G. Gunderson, S. T. Barlow, and B. Zhang, "FIB-milled quartz nanopores in a sealed nanopipette," *J. Electroanal. Chem.*, vol. 833, no. December 2018, pp. 181–188, 2019, doi: 10.1016/j.jelechem.2018.11.052.

[42] R. G. Musket, J. M. Yoshiyama, R. J. Contolini, and J. D. Porter, "Vapor etching of ion tracks in fused silica," *J. Appl. Phys.*, vol. 91, no. 5760, 2002, doi: 10.1063/1.1467402.

[43] C. Milanez Silva, P. Varisco, A. Moehlecke, P. P. Fichtner, R. M. Papaléo, and J. Eriksson, "Processing of nano-holes and pores on SiO2 thin films by MeV heavy ions," *Nucl. Instruments Methods Phys. Res. Sect. B Beam Interact. with Mater. Atoms*, vol. 206, pp. 486–489, 2003, doi: 10.1016/S0168-583X(03)00803-6.

[44] P. B. Price and R. M. Walker, "Chemical etching of charged-particle tracks in solids," *J. Appl. Phys.*, vol. 33, no. 12, pp. 3407–3412, 1962, doi: 10.1063/1.1702421.

[45] P. Apel, "Track etching technique in membrane technology," *Radiat. Meas.*, vol. 34, no. 1–6, pp. 559–566, 2001, doi: 10.1016/S1350-4487(01)00228-1.

[46] C. Hedlund, U. Lindberg, U. Bucht, and J. Soderkvist, "Anisotropic etching of Z-cut quartz," *J. Micromechanics Microengineering*, vol. 3, no. 2, 1993.

[47] P. Rangsten, C. Hedlund, I. V. Katardjiev, and Y. Bäcklund, "Etch rates of crystallographic planes in Z-cut quartz - Experiments and simulation," *J. Micromechanics Microengineering*, vol. 8, no. 1, pp. 1–6, 1998, doi: 10.1088/0960-1317/8/1/001.

[48] P. Suda, A. . Zumsteg, and W. Zinng, "Anisotropy of Etching Rate for Quartz in Ammonium Bifluoride," in *33rd Annual Symposium on Frequency Control*, 1979, pp. 359–363, doi: 10.1109/FREQ.1979.200339.

[49] F. M. Ernsberger, "Structural effects in the chemical reactivity of silica and silicates," *J. Phys. Chem. Solids*, vol. 13, no. 3–4, pp. 347–351, 1960.

[50] G. M. Rignanese, J. C. Charlier, and X. Gonze, "First-principles molecular-dynamics investigation of the hydration mechanisms of the (0001) α-quartz surface," *Phys. Chem. Chem. Phys.*, vol. 6, no. 8, pp. 1920–1925, 2004, doi: 10.1039/b311842h.

[51] J. S. Judge, "A Study of the Dissolution of SiO2 in Acidic Fluoride Solutions," *J. Electrochem. Soc.*, vol. 118, no. 11, p. 1772, 1971.

[52] D. J. Monk, D. S. Soane, and R. T. Howe, "A review of the chemical reaction mechanism and kinetics for hydrofluoric acid etching of silicon dioxide for surface micromachining applications," *Thin Solid Films*, vol. 232, no. 1, pp. 1–12, 1993, doi: 10.1016/0040-6090(93)90752-B.

[53] J. K. Vondeling, "Fluoride-based etchants for quartz," *J. Mater. Sci.*, vol. 18, no. 1, pp. 304–314, 1983, doi: 10.1007/BF00543840.

[54] C. R. Helms and B. E. Deal, " Mechanisms of the HF/H 2 O vapor phase etching of SiO 2 ," *J. Vac. Sci. Technol. A Vacuum, Surfaces, Film.*, vol. 10, no. 4, pp. 806–811, 1992, doi: 10.1116/1.577676.

[55] D. M. Knotter, "Etching mechanism of vitreous silicon dioxide in HF-based solutions," *J. Am. Chem. Soc.*, vol. 122, no. 18, pp. 4345–4351, 2000, doi: 10.1021/ja993803z.

[56] N. Miki, H. Kikuyama, I. Kawanabe, M. Miyashita, and T. Ohmi, "Gas-Phase Selective Etching of Native Oxide," *IEEE Trans. Electron Devices*, vol. 37, no. 1, pp. 107–115, 1990, doi: 10.1109/16.43806.

[57] M. A. Kozlova and P. A. Shkonda, "Structure of the Surfaces of Vitreous Silica and Quartz After Prolonged Etching in Hf.," *The Soviet journal of glass physics and chemistry*, vol. 13, no. 2. pp. 127–130, 1987.

[58] M. Wong and R. A. Bowling, "Silicon Etch Using Vapor Phase HF/H2O and O3," *J. Electrochem. Soc.*, vol. 140, no. 2, pp. 567–570, 1993.

[59] E. Y. Kaniukov *et al.*, "Tunable nanoporous silicon oxide templates by swift heavy ion tracks technology," *Nanotechnology*, vol. 27, no. 11, 2016, doi: 10.1088/0957-4484/27/11/115305.

[60] J. Jensen, G. Possnert, A. Razpet, and M. Skupinski, "Ion track formation below 1 MeV/u in thin films of amorphous SiO 2," *Nucl. Instrum. Methods Phys. Res. B.*, vol. 243, no. 1, pp. 119–126, 2006, doi: 10.1016/j.nimb.2005.07.226.

[61] B. Canut, M. G. Blanchin, S. Ramos-Canut, V. Teodorescu, and M. Toulemonde, "Incorporation of sol-gel SnO2: Sb into nanoporous SiO 2," *Nucl. Instruments Methods Phys. Res. Sect. B Beam Interact. with Mater. Atoms*, vol. 245, no. 1, pp. 327–331, 2006, doi: 10.1016/j.nimb.2005.11.123.

[62] L. Singh, A. S. Sandhu, S. Singh, and H. S. Virk, "Etching and annealing kinetics of heavy ion tracks in quartz crystal," *Nucl. Instruments Methods Phys. Res. Sect. B Beam Interact. with Mater. Atoms*, vol. 46, no. 1–4, pp. 149–151, 1990, doi: https://doi.org/10.1016/0168-583X(90)90687-P.

[63] H. Iwata, "Multistage chemical etching for high-precision adjustment of resonance frequencies in ultrahigh-frequency-fundamental quartz resonators," *Proc. IEEE Int. Freq. Control Symp. Expo.*, pp. 121–124, 2005, doi: 10.1109/freq.2004.1418439.

[64] C. R. Tellier, "Some results on chemical etching of AT-cut quartz wafers in ammonium bifluoride solutions," *J. Mater. Sci.*, vol. 17, no. 5, pp. 1348–1354, 1982, doi: 10.1007/BF00752244.

[65] A. Hadley *et al.*, "Etched ion tracks in amorphous SiO2 characterized by small angle x-ray scattering: Influence of ion energy and etching conditions," *Nanotechnology*, vol. 30, no. 27, 2019, doi: 10.1088/1361-6528/ab10c8.

[66] F. Bergamini, M. Bianconi, and S. Cristiani, "Wet and vapor etching of tracks produced in SiO2 by Ti ion irradiation," *Nucl. Instruments Methods Phys. Res. Sect. B Beam Interact. with Mater. Atoms*, vol. 257, no. 1-2 SPEC. ISS., pp. 593–596, 2007, doi: 10.1016/j.nimb.2007.01.045.

[67] B. J. Jurcik, J. R. Brock, and I. Trachtenberg, "Anisotropic Etching of SiO2 with a 38.2 Weight Percent Hydrofluoric Acid Aerosol," *J. Electrochem. Soc.*, vol. 138, no. 7, pp. 2141–2145, 1991.

[68] Y. Zhang *et al.*, "New ion beam materials laboratory for materials modification and irradiation effects research," *Nucl. Inst. Methods Phys. Res. B*, vol. 338, pp. 19–30, 2014, doi: 10.1016/j.nimb.2014.07.028.

[69] M. L. Crespillo, J. T. Graham, Y. Zhang, and W. J. Weber, "In-situ luminescence monitoring of ion-induced damage evolution in SiO2 and Al2O3," *J. Lumin.*, vol. 172, pp. 208–218, 2016, doi: 10.1016/j.jlumin.2015.12.016.

[70] A. Climent-Font, F. Paszti, G. Garcia, M. T. Fernandez-Jimenez, and F. Agullo, "First measurements with the Madrid 5 MV tandem accelerator," *Nucl. Instruments Methods Phys. Res. B*, vol. 219–220, pp. 400–404, 2004, doi: 10.1016/j.nimb.2004.01.090.

[71] O. Peña-Rodríguez, J. Manzano-Santamaría, A. Rivera, G. García, J. Olivares, and F. Agulló-López, "Kinetics of amorphization induced by swift heavy ions in α-quartz," *J. Nucl. Mater.*, vol. 430, no. 1–3, pp. 125–131, 2012, doi: 10.1016/j.jnucmat.2012.07.001.

[72] J. F. Ziegler, M. D. Ziegler, and J. P. Biersack, "SRIM - The stopping and range of ions in matter (2010)," *Nucl. Instruments Methods Phys. Res. Sect. B Beam Interact. with Mater. Atoms*, vol. 268, no. 11–12, pp. 1818–1823, 2010, doi: 10.1016/j.nimb.2010.02.091.

[73] L. T. W. Lim, A. T. S. Wee, and S. J. O'Shea, "Effect of tip size on force measurement in atomic force microscopy," *Langmuir*, vol. 24, no. 6, pp. 2271–2273, 2008, doi: 10.1021/la703231h.

[74] M. L. Crespillo, "Ion beam damage by electronic excitation with swift heavy ions in lithium niobate : mechanisms and nanostructuring for photonic applications," Universidad Autonoma de Madrid, 2011.

[75] M. Toulemonde, C. Dufour, A. Meftah, and E. Paumier, "Transient thermal processes in heavy ion irradiation of crystalline inorganic insulators," *Nucl. Instruments Methods Phys. Res. Sect. B Beam Interact. with Mater. Atoms*, vol. 166, pp. 903–912, 2000, doi: 10.1016/S0168-583X(99)00799-5.

[76] A. Rivera, G. Garcia, J. Olivares, M. L. Crespillo, and F. Agulló-López, "Elastic (stress-strain) halo associated with ion-induced nano-tracks in lithium niobate: Role of crystal anisotropy," *J. Phys. D. Appl. Phys.*, vol. 44, no. 47, 2011, doi: 10.1088/0022-3727/44/47/475301.

[77] M. L. Crespillo *et al.*, "Optimization of nanopores obtained by chemical etching on swift-ion irradiated lithium niobate," *Nucl. Instruments Methods Phys. Res. Sect. B Beam Interact. with Mater. Atoms*, vol. 267, no. 6, pp. 1035–1038, 2009, doi: 10.1016/j.nimb.2009.02.028.

II. RAMAN CHARACTERIZATION OF PHONON CONFINEMENT AND STRAIN EFFECTS FROM LATENT ION TRACKS IN α-QUARTZ

Maria C. Garcia Toro [a], Miguel L. Crespillo [b], Joseph T. Graham [a, c.]

[a] Nuclear Engineering Program, Missouri University of Science and Technology, 65409, Rolla, MO, United States

[b] Department of Material Science and Engineering, University of Tennessee, 37996, Knoxville, TN, United States

[c] Department of Materials Science and Engineering, Missouri University of Science and Technology, 65409, Rolla, MO, United States

ABSTRACT

This study reports phonon confinement and strain effects in the Raman spectrum of ion irradiated and subsequently etched α-quartz. Y- and Z- cut α-quartz single crystals were irradiated at room temperature with 20 MeV Ni^{6+} and 40 MeV I^{7+} ions. Latent ion tracks were produced with areal densities ranging from the isolated track regime to the overlapping track regime (nominal fluences of $1x10^{9}$, $1x10^{10}$, and $1x10^{11}$ ions cm^{-2}). Nanowell structures were revealed after vapor etching with HF aqueous solutions. A phonon confinement model was invoked to explain the observed changes in the shape of the strong Raman peak located around 463 cm^{-1}. Phonon coherence lengths of the irradiated samples were determined by fitting experimental data to the confinement model. An additional blue shift at higher ion fluences was attributed to a contribution from lattice strain when track separations are small and the overlapping strain fields around ion tracks extend through a large volume fraction of the crystal.

Keywords: Phonon confinement, Raman Spectroscopy, ion tracks, α-quartz, swift heavy ions

1. INTRODUCTION

Raman spectroscopy is a non-destructive tool that has been widely used for studying phonon dynamics, structure, and the phases of different materials, including nanostructured materials [1]–[8]. In the first-order Raman scattering process, when long-range order exists over length scales comparable to the wavelength of the incident photons, only phonons with small wave vector (i.e. those near the Brillouin-zone center) contribute to the Raman signal, producing Stokes lines with Lorentzian shape and narrow FWHM [9], [10]. In the case of nanomaterials, where long-range order is reduced to submicron or nanometric dimensions, the wave vector selection rule is relaxed, causing contributions from phonons further away from the Brillouin-zone center to contribute to the Raman signal. This phenomenon has been described as a phonon confinement effect. It can lead to major modifications in the vibrational, electronic, and nonlinear properties of the material [6]–[8]. In the Raman spectrum, it appears as asymmetric broadening and shifting of the Raman bands [9]–[13].

Confinement effects have been observed in structurally modified single crystals and polycrystals [5], [6], [14]–[16]. Ionizing radiation, for example, can produce disorder in a crystal through the introduction of defects like ion tracks, voids, phase precipitates, and dislocations [17], [18]. When disorder is introduced, the correlation length of the phonons is reduced as the wave vector selection rule is relaxed. Consequently, the

phonon modes shift and broaden asymmetrically as the irradiation fluence is increased [19], [20].

With the aforementioned considerations in mind, the present study aims to analyze the phonon confinement effect in a crystalline material that was irradiated to produce ion tracks and subsequently etched to produce nanowells. Latent ion tracks are amorphous or highly disordered columnar nanostructures created by the passage of highly energetic ions through a material, causing atomic displacements, and thus creating highly-disordered regions along the ion pathway [21]–[23]. The projectile ions must have electronic stopping powers (S_e) higher than a certain threshold ($S_{e,Th}$) [21], [24], [25]. Through chemical etching, it is possible to preferentially remove the disordered volume of the ion track and produce holes in the crystal structure (nanowells) [26]–[30]. It is believed that phonons can be scattered or confined by the presence of various defects and nanostructures, including ion tracks and nanopores [31]–[33]. Studying the ion track-induced alteration of the phonon spectrum helps one understand how energy and heat transfer may be tailored by irradiating materials with ion beams [34].

Experiments were conducted using single crystals of α-quartz. Raman spectra of α-quartz with ion tracks and etched ion tracks (resulting in nanowells) were measured as a function of the ion fluence for two different crystal orientations. In addition to being a commonly occurring mineral in Earth's crust, quartz has many technological uses thanks to its optical and dielectric properties [35]–[41]. The phonon spectrum of quartz has been studied extensively with Raman and Infrared spectroscopy [42]–[49], with which it has been possible to completely define the fundamental optical phonon modes at the center of the Brillouin zone. However, to the authors' knowledge, none of these previous studies

have examined the effect of ion tracks or porous structures on the phonon properties of quartz. Thus, this study presents new knowledge of phonon confinement effects in irradiated α-quartz. The irradiation conditions, etching processes, and characterization are described in greater detail in a companion paper.

Measurements using Raman Spectroscopy, in conjunction with Density Functional Perturbation Theory calculations, performed with the first principles code, ABINIT [50], were conducted to analyze the effect of ion tracks on phonon confinement.

2. METHODOLOGY

30 samples of single-crystal Y- and Z-cut α-SiO_2 from MTI corp. (15 samples per direction), were used in this study. The samples had dimensions of 10×10×1 mm and were polished to optical grade on one side.

The samples were irradiated at room temperature with both 20 MeV nickel ions (20 MeV – Ni^{6+}) and 40 MeV iodine ions (40 MeV – I^{7+}) at nominal fluences of 1×10^{9}, 1×10^{10}, and 1×10^{11} ions cm^{-2}. At these energies, continuous track lengths are expected to be at least 2 μm ($S_e > S_{e,Th} \approx$ 2-5 keV nm-1 [21], [51], [52]).

Subsequent chemical vapor-etching with aqueous solutions of hydrofluoric acid at concentrations of 10%w, 20%w, and 30%w were conducted for various etching times. Figure 1 shows a schematic diagram the irradiation and etching processes used to produce ion tracks and nanowells.

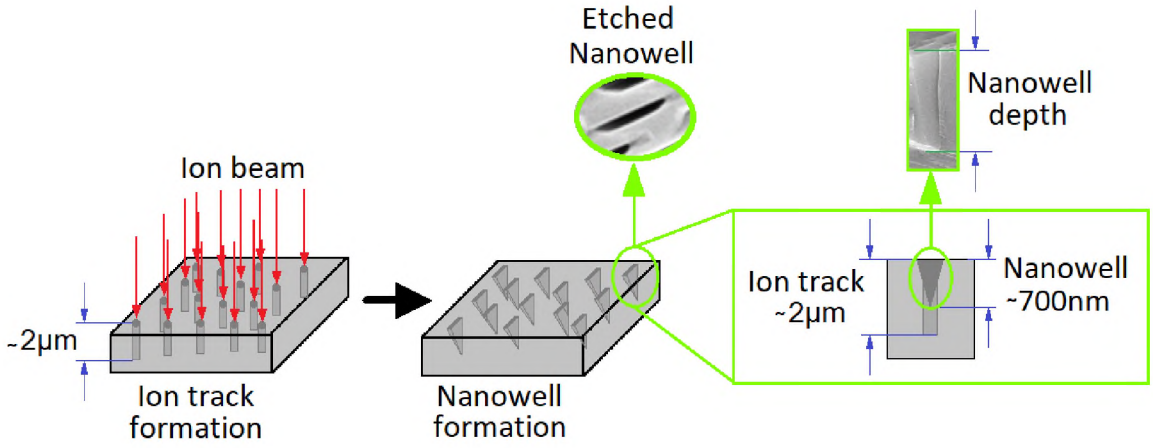

Figure 1. Schematic diagram of ion tracks and nanowells formation

Raman measurements were taken with a Horiba Xplora Plus Confocal Raman Microscope. Unirradiated, irradiated, and etched samples were analyzed for comparison purposes. The measurements were conducted at room temperature. A 785 nm semiconductor laser was used with a 1800 lines mm^{-1} grating and a 100 µm diameter confocal aperture. A 100× objective with an air numerical aperture of 0.9 was used. Based on these parameters, the index of refraction of quartz and the formulae in [53], an optical sectioning resolution (FWHM) of about 2 µm is assumed. With the focal plane placed on the surface region of the sample, this ensures that the Raman signal mostly contains information from the ion track region and not from the underlying single crystal substrate (depth > ~2µm). All measurements were acquired in the backscattering geometry without polarization optics.

Analysis of the Raman measurements was divided into three sections to compare the differences produced in the spectra when: (1) the samples are irradiated with different ions (effect of mass and energy of projectile ion), (2) the irradiation is conducted at different ion fluences (ion fluence effect), and (3) the sample is unirradiated, irradiated or etched (effect of nanostructure features on the modification of substrate properties).

In general, it was possible to identify the Raman active optical phonon modes at the center of the Brillouin zone for frequencies between 100 cm^{-1} and 500 cm^{-1} in all measured samples. Well-defined bands located around 120, 205, 263, 354, 393, 398, and 463 cm^{-1} were found in the Raman spectra for Y- and Z-cut samples. Differences in the peak intensities were observed and are related to the dependence of the vibrational modes on the crystal orientation [46], [54].

3. RESULTS AND DISCUSSION

3.1. RAMAN EXPERIMENTAL DATA ANALYSIS

Figure 2 shows the Raman spectra of Y- and Z-cut samples irradiated with 1×10^{9} ions cm^{-2} of 40 MeV I^{7+} and 20 MeV Ni^{6+} ions. The spectra were normalized to the maximum intensity value and shifted vertically for better visualization. The phonon modes are specified for each peak, where A1 represents the non-degenerate phonons and E represents the doubly degenerate phonons that can present longitudinal (L) or transverse (T) oscillations.

By comparing the Raman spectrum for each crystal orientation, it can be observed that the peak at 120 cm^{-1} has a higher intensity for Z-cut samples while the peak at 263

cm^{-1} is not present in this crystal orientation. A similar situation occurs with the peak centered at 393 cm^{-1} that is not present in the spectrum obtained from Y-cut samples. The peaks at 205 cm^{-1} and 463 cm^{-1} remain in the spectra with small changes in the intensity for each crystal orientation. Henceforth, the analysis of the Raman spectra was restricted to the most intense Raman peak, located at 463 cm^{-1}, to obtain consistent analysis for both crystal orientations. It is important to note that the vibration located at 463 cm^{-1} can be described as the motion of the bridging oxygen in the planes bisecting pairs of Si atoms in Si-O-Si groups [46], [54].

In comparing the data obtained from samples irradiated with the different ions, consistent behavior was observed in the evolution of the line shape. In other words, the Raman spectra obtained from samples irradiated with Ni^{6+} did not present significant differences when compared to those obtained after irradiation with I^{7+} at the same fluence, despite the differences in ion mass, energy, and electronic stopping powers (ΔS_e = 2.41 keV nm^{-1} at the surface). These results can be explained by the production of ion tracks with similar diameters and depths.

From the companion paper, it was found that the irradiation conditions used here produced surface features with comparable dimensions in both Y- and Z-cut samples when irradiating with these two different ions. While the ion tracks may differ in radius by several nanometers, the inter-track spacing is primarily determined by the ion fluence at low fluences. Therefore, one can conclude that either the structure of the tracks are similar or that the structure and morphology of the tracks do not contribute significantly to changes in the Raman spectra (at least to within the equipment resolution (0.5 cm^{-1})). The magnified view of the 463 cm^{-1} peak on the right side of Figure 2 shows no

observable change in peak center or width, with crystallographic orientation or ion (at the same fluence). Similar behavior was found with the other Raman bands.

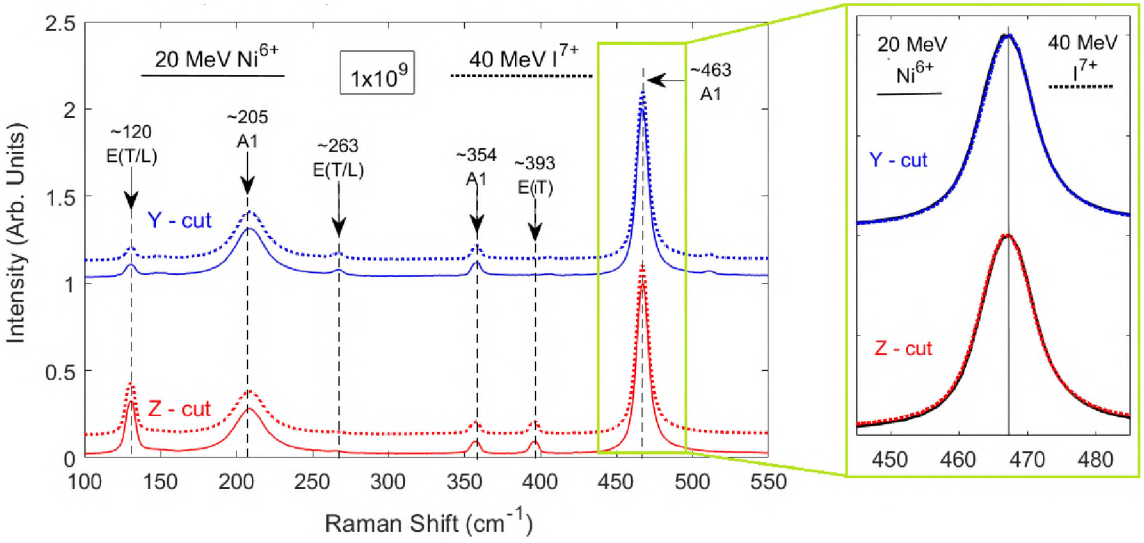

Figure 2. Raman spectra of Y- and Z-cut quartz samples, irradiated with 20 MeV Ni^{6+} and 40 MeV I^{7+} to a fluence of 1×10^{9} ions cm^{-2}

In contrast to ion species and energy, a systematic variation in line-shape was found with increasing ion fluence. Measurements of irradiated samples at different fluences (1×10^{9}, 1×10^{10}, 1×10^{11} ions cm^{-2}) were taken in conjunction with unirradiated samples for comparison purposes. Figure 3 shows the 463 cm^{-1} peak for Y-cut samples that were irradiated with 40 MeV I^{7+} at different fluences along with an unirradiated control. It was found that the Raman bands broadened and shifted to higher frequencies with increasing fluence. Comparable results were obtained for Z-cut samples and for

samples irradiated with 20 MeV Ni^{6+}. The broadening behavior is related to the atomic disorder added to the samples [5], [6], [14]–[16]. This disorder is caused by radiation damage produced during the passage of the incident ion through the crystal structure [55].

The broadening and peak shifting can also be related to the relaxation of the wave vector selection rules, or, equivalently, to the reduction of the correlation length of the phonon modes. The higher the ion fluence, the smaller the areal fraction of defect-free crystalline material [19], [20], [56]–[58]. It should be noted, however, that even up to fluences of 1×10^{11} ions cm^{-2} no amorphous background was observed. This suggests that the actual areal fraction of amorphous or glassy material is below detection limits and that the observed changes in line shape are more likely due to the phonon confinement effect.

In Raman spectra, a shift of the peak center can also indicate the presence of strain. The sign of the shift depends on the sign of the stress and a shift without corresponding broadening is indicative of uniform strain [59]. Accordingly, the blue shift in the peak at 463 cm^{-1} may also be caused, wholly, or in part, by compressive strain in the crystalline regions between ion tracks. This is consistent with the expectation that disordered/amorphous track cores have a lower density than the surrounding matrix and therefore exert an outward compressive strain on the crystalline matrix.

Figure 4 shows the Raman peak at 463 cm^{-1} for Y-cut samples before and after being irradiated with 40 MeV I^{7+} at 1×10^{9} cm^{-2}, and after etching with an aqueous solution of 30%w of HF for one hour. As shown in a companion paper, etching with 30%w HF for one hour produces well-defined nanowells with diameters up to 300 nm and depths up to 700 nm. As with the non-etched ion irradiated samples, the peaks for the

etched sample experience both a blue shift and broadening relative to the unirradiated specimens. However, the Raman peak obtained from the etched samples was slightly redshifted relative to the irradiated samples ($\Delta\omega$ ~2.04 cm^{-1}). The shift back towards the original centroid can be explained as a partial release of the compressive strain by the ion track core when the core is removed in the etching process.

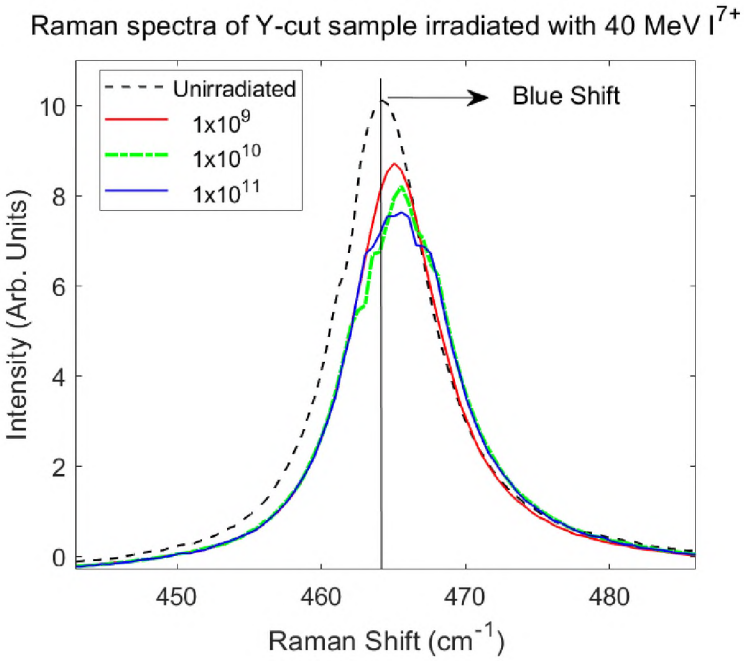

Figure 3. Raman peak centered at 463 cm^{-1} for Y-cut samples irradiated with 40 MeV I^{7+} ions at different ion fluences

The residual shift and broadening may be due to a combination of the remaining section of the un-etched ion track and/or by phonon confinement. As mentioned before, the phonon confinement effect can manifest itself as both shifting and asymmetric

broadening of the peaks. To evaluate the symmetry of the peak broadening, open-source software for nonlinear curve fitting and data analysis, Fityk 0.9.8, was used [60]. A split Voigt function was used to fit the measured Raman peaks. The peak center, the left half width at half maximum (HWHM1), and the right half width at half maximum (HWHM2) were determined through least-squares fitting.

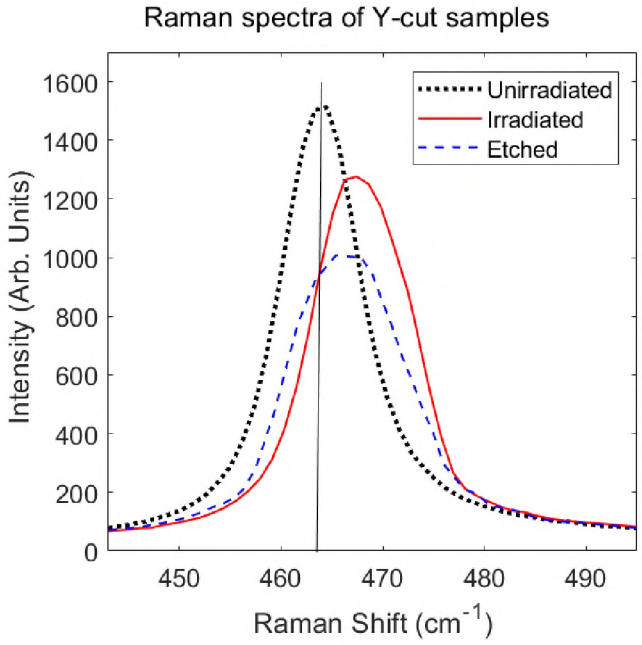

Figure 4. Raman peak centered at 463 cm^{-1} for Y-cut samples before the irradiation process (pristine), after being irradiated with 40 MeV I^{7+} at 1×10^{9} cm^{-2}, and etched with 30%w HF solutions for 1 hour

The asymmetric peak broadening was evaluated by calculating the asymmetry factor, J, defined as the ratio of the right HWHM to left HWHM. An asymmetry factor of 1 indicates symmetric peak broadening. Symmetric broadening might be better explained

using phonon lifetime arguments than by invoking phonon confinement. Values greater than 1 indicate a positive skew while values less than 1 indicate negative skew [61]–[64]. In phonon confinement models, the sign of the skew is related to the curvature of the Raman active phonon dispersion curve at the Brillouin zone center. Figure 5 shows the asymmetry factor values for unirradiated, irradiated, and etched samples, for Y- and Z-cut orientations, irradiated with both ions to a fluence of 1×10^{9} ions cm^{-2}. All samples asymmetrically broadened towards higher frequency values (J >1), making phonon confinement a plausible explanation. Z-cut samples presented a larger gap in the J values when irradiating with 40 MeV I^{7+}, even after the etching process.

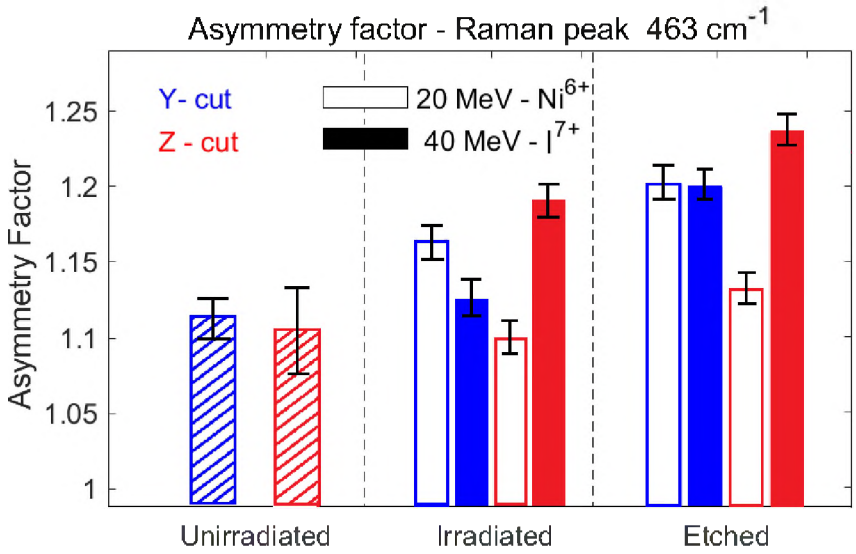

Figure 5. Asymmetry factor values for unirradiated, irradiated, and etched samples, at Y- and Z-cut orientations, that were irradiated with the two different ions at a fluence of 1×10^{9} cm^{-2}

3.2. THEORETICAL FRAMEWORK: APPLICATION OF PHONON-CONFINEMENT MODEL (PCM) TO NANOSTRUCTURED α-QUARTZ

To complement the experimental analysis, calculations of the phonon coherence length were obtained from the theoretical phonon-confinement model (PCM), developed by Richter *et al.* [61] who used it to describe Raman scattering from optical phonons in nanostructures. According to the PCM, the first-order Raman scattering intensity, $I(\omega)$, is given by Equation (1) [61], [62]:

$$I(\omega) = \int \frac{|C(0,q)|^2 d^3q}{[\omega - \omega(q)]^2 + \left(\frac{\Gamma_o}{2}\right)^2} \times [n(\omega_i) - 1] \times \langle R^2 \rangle \tag{1}$$

$\omega(q)$ is the phonon dispersion curve for the branch of interest, Γ_o is the natural linewidth (FWHM) of the zone-center optical phonon in the unirradiated samples, and $C(0,q)$ is the Fourier transform of the confinement function. $n(\omega_i)$ is the Bose occupation number, and $\langle R^2 \rangle$ are the Raman susceptibility tensors that establish the polarization direction depending on the crystal orientation. The Fourier transform of the confinement function is given by Equation (2):

$$C(0,q)^2 = \exp\left(\frac{-q^2L^2}{4}\right) \tag{2}$$

where L is the coherence length. The Bose occupation number is given by Equation (3):

$$n(\omega_i) - 1 = \left[1 - \exp\left(-\hbar\omega_i / k_B T\right)\right]^{-1} \tag{3}$$

The Raman susceptibility tensors are given by Equation (4):

$$\langle R^2 \rangle = \boldsymbol{e}_s \times \boldsymbol{a}_{i,j,n\gamma} \times \boldsymbol{e}_l \quad (4)$$

$\boldsymbol{e}_s$ and $\boldsymbol{e}_l$ are the unit polarization vectors of the scattered and incident photons. $\boldsymbol{a}_{i,j,n\gamma}$ is the Raman tensor that includes the first-order change in the dielectric susceptibility tensors and the eigendisplacement vectors.

To calculate $I(\omega)$, simulations with the Abinit quantum chemistry code [50] were conducted. The calculations were conducted with the linear and nonlinear response within the framework of Density Functional Perturbation Theory (DFPT) and the 2n+1 theorem. The dielectric tensors, interatomic forces, the phonon energies for each phonon wave vector, and the eigenvectors were obtained.

The phonon dispersion curves (Figure 6), were found to be in agreement with previous studies [42]–[44], [48], [49], [65]–[68]. $I(\omega)$ curves were calculated for a range of L values. The peak center and HWHM values were measured with Fityk using a split Voigt function following the same procedure used to analyze the experimental spectra. Figure 7 shows the fitting parameters of the 463 cm^{-1} Raman peak obtained from the irradiated samples (data points) with the model prediction (line) parameterized by coherence length. Good agreement was found between the measured parameters and the model, indicating that the PCM can describe most of the observed spectral changes. As mentioned above, the etching studies seemed to indicate that a portion of the peak shift could be due to compressive strain between the tracks.

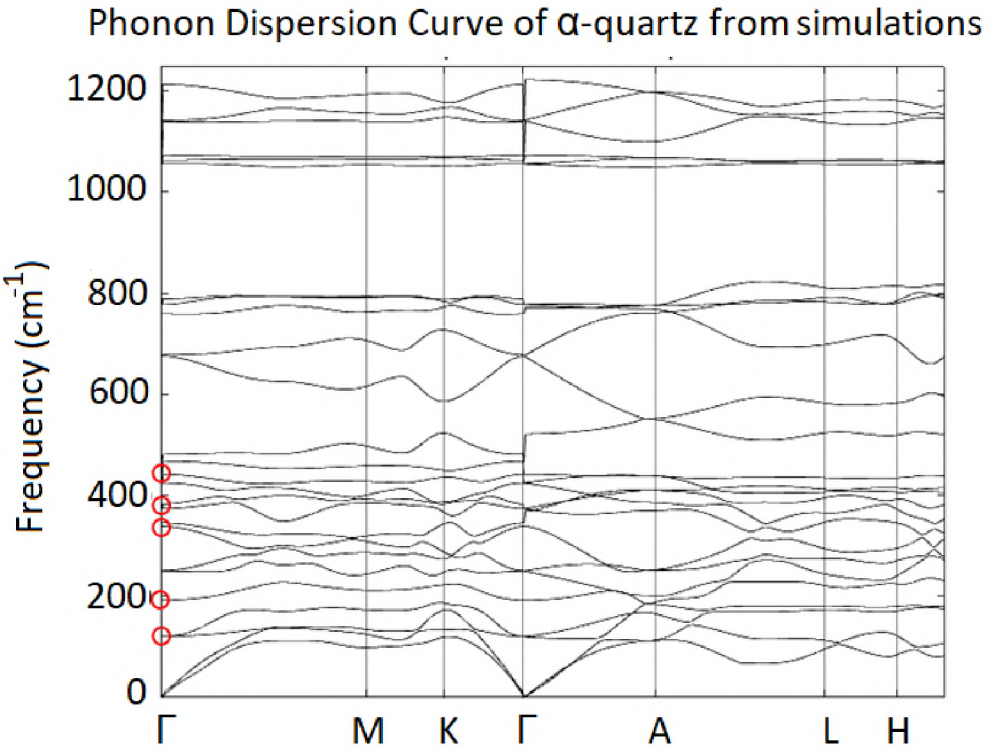

Figure 6. Phonon dispersion curve for α-quartz obtained by simulations with Abinit

This could explain the additional blue shift of the measured data, especially at 1×10^{11} ions cm^{-2}, where the areal fraction of crystal under compressive strain is large. The obtained phonon coherence lengths were ~66 nm for samples irradiated with 1×10^{9} ions cm^{-2}, ~58 nm for samples irradiated with 1×10^{10} ions cm^{-2}, and ~45 nm for samples irradiated with 1×10^{11} cm^{-2}. As expected, with decreasing mean track separation (higher fluences), there is a corresponding decrease in coherence length.

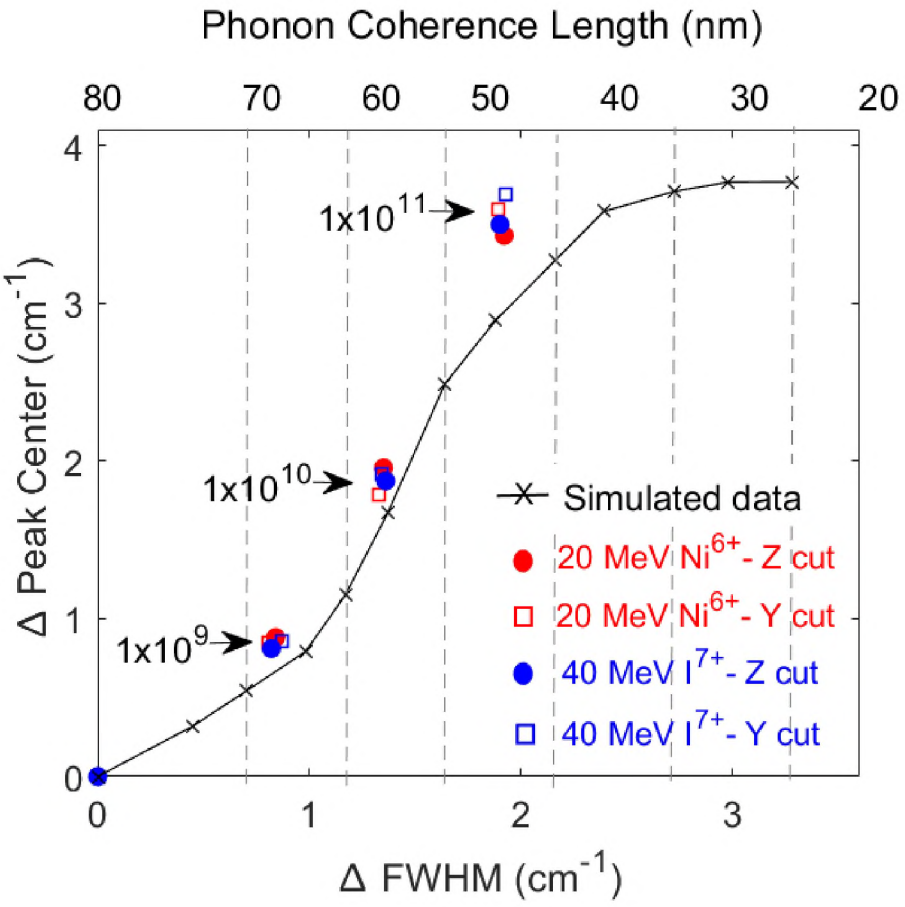

Figure 7. Phonon coherence length of the 463 cm^{-1} Raman peak for the Y- and Z-cut samples irradiated with 20 MeV Ni^{6+} and 40 MeV I^{7+} with different fluences

4. CONCLUSIONS

Phonon confinement effects in ion irradiated and etched samples of α-quartz were investigated. Samples of Y- and Z-cut quartz were irradiated with 20 MeV Ni^{6+} and 40 MeV I^{7+} at ion fluences of 1×10^{9}, 1×10^{10}, and 1×10^{11} cm^{-2}. Samples were etched with aqueous solutions of HF at different concentrations to create nanowells in the crystal structure. Raman measurements indicated changes in peak center, breadth, and symmetry

induced by irradiation and etching. It was observed that the peaks experience a blue shift and broadening asymmetrically with positive skew after irradiation, in agreement with a phonon confinement effect. Similar results were found when analyzing the etched samples, with the main difference being that the Raman peaks experienced a slight red shift relative to the irradiated samples. This is interpreted as relaxation of the stress when the track core was removed in the etching process. Calculations of the phonon coherence length were conducted by curving fitting the experimental spectra and spectra obtained by a phonon confinement model. It was found that the phonon coherence lengths decreased with increasing flux, suggesting that ion tracks may confine optical phonons in quartz.

ACKNOWLEDGMENTS

This work was supported by the Nuclear Regulatory Commission Faculty Development Grant NRC-HQ-84-15-G-0044. M.L.C. acknowledges support from the University of Tennessee Governor's Chair program. The authors are grateful to the staff in The Centro de Microanálisis de Materiales - Universidad Autónoma de Madrid for assistance with experimental irradiations. Also, the authors want to thank the Materials Research Center (MRC) at Missouri S&T for its support and use of equipment.

REFERENCES

[1] D. J. Gardiner, *Introduction to Raman Scattering*. 1989.

[2] P. Hermet, M. Veithen, and P. Ghosez, "First-principles calculations of the nonlinear optical susceptibilities and Raman scattering spectra of lithium niobate," *J. Phys. Condens. Matter*, vol. 19, no. 45, 2007, doi: 10.1088/0953-8984/19/45/456202.

[3] D. Georgescu, L. Baia, O. Ersen, M. Baia, and S. Simon, "Experimental assessment of the phonon confinement in TiO2 anatase nanocrystallites by Raman spectroscopy," *J. Raman Spectrosc.*, vol. 43, no. 7, pp. 876–883, 2012, doi: 10.1002/jrs.3103.

[4] I. E. Tyschenko *et al.*, "Raman shifts and photoluminescence of the InSb nanocrystals ion beam-synthesized in buried SiO2 layers," *J. Lumin.*, vol. 204, no. March, pp. 656–662, 2018, doi: 10.1016/j.jlumin.2018.08.057.

[5] A. Antony *et al.*, "A study of 8 MeV e-beam on localized defect states in ZnO nanostructures and its role on photoluminescence and third harmonic generation," *J. Lumin.*, vol. 207, no. May 2018, pp. 321–332, 2019, doi: 10.1016/j.jlumin.2018.11.043.

[6] H. S. Mavi, B. G. Rasheed, A. K. Shukla, S. C. Abbi, and K. P. Jain, "Spectroscopic investigation of porous silicon prepared by laser-induced etching," *J. Phys. D. Appl. Phys.*, vol. 34, no. 3, p. 292, 2001.

[7] H. S. Mavi, P. Sudakshina, A. K. Shukla, and S. C. Abbi, "Nonlinear phenomenon in nanocrystallites produced by laser-induced etching of silicon," *Opt. Commun.*, vol. 226, no. 1–6, pp. 405–413, 2003, doi: 10.1016/j.optcom.2003.08.035.

[8] P. Sudakshina, H. S. Mavi, and A. K. Shukla, "Optical nonlinearity in silicon nanoparticles: Effect of size and probing intensity," *Phys. Rev. B - Condens. Matter Mater. Phys.*, vol. 71, no. 11, p. 113313, 2005, doi: 10.1103/PhysRevB.71.113313.

[9] D. Nesheva, "Raman scattering from semiconductor nanoparticles and superlattices," *J. Optoelectron. Adv. Mater.*, vol. 7, no. 1, pp. 185–192, 2005.

[10] P. C. Ricci, M. Salis, and A. Anedda, "Phonon characterization of nano-crystals by Raman spectroscopy," *Chem. Phys. Lett.*, vol. 457, no. 1–3, pp. 191–193, 2008, doi: 10.1016/j.cplett.2008.04.002.

[11] S. K. Gupta, R. Desai, P. K. Jha, S. Sahoo, and D. Kirin, "Titanium dioxide synthesized using titanium chloride: Size effect study using Raman spectroscopy and photoluminescence," *J. Raman Spectrosc.*, vol. 41, no. 3, pp. 350–355, 2010, doi: 10.1002/jrs.2427.

[12] J. E. Spanier, R. D. Robinson, F. Zhang, S. W. Chan, and I. P. Herman, "Size-dependent properties of (formula presented) nanoparticles as studied by Raman scattering," *Phys. Rev. B - Condens. Matter Mater. Phys.*, vol. 64, no. 24, pp. 1–8, 2001, doi: 10.1103/PhysRevB.64.245407.

[13] D. Wang, J. Zhao, B. Chen, and C. Zhu, "Lattice vibration fundamentals in nanocrystalline anatase investigated with Raman scattering," *J. Phys. Condens. Matter*, vol. 20, no. 8, 2008, doi: 10.1088/0953-8984/20/8/085212.

[14] R. L. Dubey, S. K. Dubey, A. D. Yadav, and D. Kanjilal, "Surface modification of indium phosphide by 100 MeV iron ions," *Radiat. Eff. Defects Solids*, vol. 168, no. 7–8, pp. 557–563, 2013, doi: 10.1080/10420150.2013.789027.

[15] M. Duval *et al.*, "Quantifying hydrofluoric acid etching of quartz and feldspar coarse grains based on weight loss estimates: implication for ESR and luminescence dating studies," *Anc. TL*, vol. 36, no. 1, 2018.

[16] I. González *et al.*, "Effects of surface and confinement on the optical vibrational modes and dielectric function of 3C porous silicon carbide: An ab-initio study," *Phys. B Condens. Matter*, vol. 550, no. May, pp. 420–427, 2018, doi: 10.1016/j.physb.2018.05.024.

[17] K. linga Murty and I. Charit, *An introduction to nuclear materials: fundamentals and applications*, Illustrate. John Wiley & Sons, 2013, 2013.

[18] L. K. Mansur, A. F. Rowcliffe, R. K. Nanstad, S. J. Zinkle, W. R. Corwin, and R. E. Stoller, "Materials needs for fusion, Generation IV fission reactors and spallation neutron sources - Similarities and differences," in *Journal of Nuclear Materials*, 2004, doi: 10.1016/j.jnucmat.2004.04.016.

[19] K. K. Tioug, P. M. Amirtharaj, and F. H. Pollak, "*effects of As+ ion implantation of the raman spectra of gas: 'spatial correlation' interpretation.*," *Electrochem. Soc. Ext. Abstr.*, vol. 84–1, no. August 1983, pp. 207–208, 1984.

[20] S. Dey, C. Roy, A. Pradhan, and S. Varma, "Raman scattering characterization of Si(100) implanted with mega-electron-volt Sb," *J. Appl. Phys.*, vol. 87, no. 3, pp. 1110–1117, 2000, doi: 10.1063/1.371987.

[21] N. Itoh, D. M. Duffy, S. Khakshouri, and A. M. Stoneham, "Making tracks: Electronic excitation roles in forming swift heavy ion tracks," *J. Phys. Condens. Matter*, vol. 21, no. 47, 2009, doi: 10.1088/0953-8984/21/47/474205.

[22] E. C. H. Silk and R. S. Barnes, "Examination of fission fragment tracks with an electron microscope," *Philos. Mag.*, vol. 4, no. 44, pp. 970–972, 1959, doi: 10.1080/14786435908238273.

[23] M. Lang, R. Devanathan, M. Toulemonde, and C. Trautmann, "Advances in understanding of swift heavy-ion tracks in complex ceramics," *Curr. Opin. Solid State Mater. Sci.*, vol. 19, no. 1, pp. 39–48, 2015, doi: 10.1016/j.cossms.2014.10.002.

[24] A. Meftah *et al.*, "Track formation in SiO2 quartz and the thermal-spike mechanism," *Phys. Rev. B*, vol. 49, no. 18, pp. 12457–12463, 1994, doi: 10.1103/PhysRevB.49.12457.

[25] J. Provost *et al.*, "Swift, Heavy Ions in Insulating and Conducting Oxides: Tracks and Physical Properties," *MRS Bull.*, vol. 20, no. 12, pp. 22–28, 1995, doi: 10.1557/S0883769400045863.

[26] R. G. Musket, J. M. Yoshiyama, R. J. Contolini, and J. D. Porter, "Vapor etching of ion tracks in fused silica," *J. Appl. Phys.*, vol. 91, no. 5760, 2002, doi: 10.1063/1.1467402.

[27] J. Jensen, G. Possnert, A. Razpet, and M. Skupinski, "Ion track formation below 1 MeV/u in thin films of amorphous SiO 2," *Nucl. Instrum. Methods Phys. Res. B.*, vol. 243, no. 1, pp. 119–126, 2006, doi: 10.1016/j.nimb.2005.07.226.

[28] C. Milanez Silva, P. Varisco, A. Moehlecke, P. P. Fichtner, R. M. Papaléo, and J. Eriksson, "Processing of nano-holes and pores on SiO2 thin films by MeV heavy ions," *Nucl. Instruments Methods Phys. Res. Sect. B Beam Interact. with Mater. Atoms*, vol. 206, pp. 486–489, 2003, doi: 10.1016/S0168-583X(03)00803-6.

[29] B. Canut, M. G. Blanchin, S. Ramos-Canut, V. Teodorescu, and M. Toulemonde, "Incorporation of sol-gel SnO2: Sb into nanoporous SiO 2," *Nucl. Instruments Methods Phys. Res. Sect. B Beam Interact. with Mater. Atoms*, vol. 245, no. 1, pp. 327–331, 2006, doi: 10.1016/j.nimb.2005.11.123.

[30] A. Hadley *et al.*, "Etched ion tracks in amorphous SiO2 characterized by small angle x-ray scattering: Influence of ion energy and etching conditions," *Nanotechnology*, vol. 30, no. 27, 2019, doi: 10.1088/1361-6528/ab10c8.

[31] J. O. Orwa, K. W. Nugent, D. N. Jamieson, and S. Prawer, "Raman investigation of damage caused by deep ion implantation in diamond," *Phys. Rev. B - Condens. Matter Mater. Phys.*, vol. 62, no. 9, pp. 5461–5472, 2000, doi: 10.1103/PhysRevB.62.5461.

[32] J. M. Costantini, S. Miro, F. Beuneu, and M. Toulemonde, "Swift heavy ion-beam induced amorphization and recrystallization of yttrium iron garnet," *J. Phys. Condens. Matter*, vol. 27, no. 49, 2015, doi: 10.1088/0953-8984/27/49/496001.

[33] J. T. Graham, Y. Zhang, and W. J. Weber, "Irradiation-induced defect formation and damage accumulation in single crystal CeO2," *J. Nucl. Mater.*, vol. 498, pp. 400–408, 2018, doi: 10.1016/j.jnucmat.2017.09.046.

[34] J. Callaway, "Model for lattice thermal conductivity at low temperatures," *Phys. Rev.*, vol. 113, no. 4, pp. 1046–1051, 1959, doi: 10.1103/PhysRev.113.1046.

[35] A. Behavionr, H. Fischer, G. Gotz, and H. Karge, "Radiation Damage in Ion-Implanted Quartz Crystals," *Phys. status solidi*, vol. 76, no. 1, pp. 249–256, 1983, doi: https://doi.org/10.1002/pssa.2210760129.

[36] C. L. Phillips, R. J. Magyar, and P. S. Crozier, "A two-temperature model of radiation damage in α -quartz," *J. Chem. Phys.*, vol. 133, no. 14, 2010, doi: 10.1063/1.3481356.

[37] U. Utzinger and R. R. Richards-Kortum, "Fiber optic probes for biomedical optical spectroscopy," *J. Biomed. Opt.*, vol. 8, no. 1, p. 121, 2003, doi: 10.1117/1.1528207.

[38] F. P. Bolin, L. E. Preuss, R. C. Taylor, and R. J. Ference, "Refractive index of some mammalian tissues using a fiber optic cladding method," *Appl. Opt.*, vol. 28, no. 12, pp. 2297–2303, 1989.

[39] M. Blomqvist, O. Blomster, M. Palsson, S. Campbell, F. Becker, and W. Rath, "All-in-quartz optics for low focal shifts," in *Proceedings Volume 7912, Solid State Lasers XX: Technology and Devices*, 2011, doi: 10.1117/12.874597.

[40] C. Stambaugh, H. Shakeel, D. Kalteyer, P. Abbott, and J. Pomeroy, "Traceability of frequency based mass measurements using a quartz crystal microbalance," *J. Phys. Conf. Ser.*, vol. 1065, no. 4, 2018, doi: 10.1088/1742-6596/1065/4/042002.

[41] R. G. Macaulay-Newcombe and D. A. Thompson, "Ion bombardment damage in α-quartz at 50–295 K," *Nucl. Instruments Methods Phys. Res. Sect. B Beam Interact. with Mater. Atoms*, vol. 1, no. 2–3, pp. 176–182, 1984, doi: https://doi.org/10.1016/0168-583X(84)90065-X.

[42] B. D. Saksena, "Analysis of the Raman and infra-red spectra of α-quartz," *Proc. Indian Acad. Sci. A*, vol. 12, no. 1, p. 93, 1940.

[43] R. J. Hemley, "Pressure dependence of Raman spectra of SiO2 polymorphs: a-quartz, coesite, and stishovite," *High Press. Res. Miner. Phys.*, pp. 347–359, 1987.

[44] J. F. Scott and S. P. S. Porto, "Longitudinal and transverse optical lattice vibrations in quartz," *Phys. Rev.*, vol. 161, no. 3, pp. 903–910, 1967, doi: 10.1103/PhysRev.161.903.

[45] A. S. Pine and P. E. Tannenwald, "Temperature dependence of Raman linewidth and shift in α-quartz," *Phys. Rev.*, vol. 178, no. 3, pp. 1424–1430, 1969, doi: 10.1103/PhysRev.178.1424.

[46] R. K. Sato and P. F. McMillan, "An infrared and Raman study of the isotopic species of α-quartz," *J. Phys. Chem.*, vol. 91, no. 13, pp. 3494–3498, 1987, doi: 10.1021/j100297a008.

[47] J. . Scott, L. E. Cheesman, and S. P. . Porto, "Polariton Spectrum of -Quartz," *Phys. Rev.*, vol. 162, no. 3, p. 834, 1967.

[48] J. Onstott and G. Lucovsky, "Directional dispersion of extraordinary optical phonons in α-quartz in the frequency domain from 380 to 640cm-1," *J. Phys. Chem. Solids*, vol. 31, no. 10, pp. 2171–2184, 1970, doi: 10.1016/0022-3697(70)90231-3.

[49] P. Umari, A. Pasquarello, and A. Dal Corso, "Raman scattering intensities in α-quartz: A first-principles investigation," *Phys. Rev. B - Condens. Matter Mater. Phys.*, vol. 63, no. 9, pp. 1–9, 2001, doi: 10.1103/PhysRevB.63.094305.

[50] X. Gonze *et al.*, "ABINIT: First-principles approach to material and nanosystem properties," *Comput. Phys. Commun.*, vol. 180, no. 12, pp. 2582–2615, 2009, doi: 10.1016/j.cpc.2009.07.007.

[51] S. Klaumünzer, "Ion tracks in quartz and vitreous silica," *Nucl. Instruments Methods Phys. Res. Sect. B Beam Interact. with Mater. Atoms*, vol. 225, no. 1-2 SPEC. ISS., pp. 136–153, 2004, doi: 10.1016/j.nimb.2004.05.014.

[52] O. Peña-Rodríguez, J. Manzano-Santamaría, A. Rivera, G. García, J. Olivares, and F. Agulló-López, "Kinetics of amorphization induced by swift heavy ions in α-quartz," *J. Nucl. Mater.*, vol. 430, no. 1–3, pp. 125–131, 2012, doi: 10.1016/j.jnucmat.2012.07.001.

[53] T. Wilson, "Resolution and optical sectioning in the confocal microscope," *J. Microsc.*, vol. 244, no. 2, pp. 113–121, 2011, doi: 10.1111/j.1365-2818.2011.03549.x.

[54] A. Jayaraman, D. L. Wood, and R. G. Maines, "High-pressure Raman study of the vibrational modes in AlPO4 and SiO2 (-quartz)," *Phys. Rev. B*, vol. 35, no. 16, pp. 8316–8321, 1987, doi: 10.1103/PhysRevB.35.8316.

[55] S. Sahoo, A. K. Arora, and V. Sridharan, "Raman line shapes of optical phonons of different symmetries in anatase TiO2 nanocrystals," *J. Phys. Chem. C*, vol. 113, no. 39, pp. 16927–16933, 2009, doi: 10.1021/jp9046193.

[56] M. A. Parshin, C. Laermans, and V. G. Melehin, "Boson peak measurements in neutron-irradiated quartz crystals," *Eur. Phys. J. B*, vol. 49, no. 1, pp. 47–57, 2006, doi: 10.1140/epjb/e2006-00018-0.

[57] C. M. Silva, T. M. Rosseel, and M. C. Kirkegaard, "Radiation-Induced Changes in Quartz, A Mineral Analog of Nuclear Power Plant Concrete Aggregates," *Inorg. Chem.*, vol. 57, no. 6, pp. 3329–3338, 2018, doi: 10.1021/acs.inorgchem.8b00096.

[58] M. L. Crespillo, J. T. Graham, Y. Zhang, and W. J. Weber, "In-situ luminescence monitoring of ion-induced damage evolution in SiO2 and Al2O3," *J. Lumin.*, vol. 172, pp. 208–218, 2016, doi: 10.1016/j.jlumin.2015.12.016.

[59] F. Cerdeira, C. J. Buchenauer, F. H. Pollak, and M. Cardona, "Stress-induced shifts of first-order Raman frequencies of diamond- and zinc-blende-type semiconductors," *Phys. Rev. B*, vol. 5, no. 2, pp. 580–593, 1972, doi: 10.1103/PhysRevB.5.580.

[60] M. Wojdyr, "Fityk: A general-purpose peak fitting program," *J. Appl. Crystallogr.*, vol. 43, no. 5 PART 1, pp. 1126–1128, 2010, doi: 10.1107/S0021889810030499.

[61] H. Richter, Z. P. Wang, and L. Ley, "The one phonon Raman spectrum in microcrystalline silicon," *Solid State Commun.*, vol. 39, no. 5, pp. 625–629, 1981, doi: 10.1016/0038-1098(81)90337-9.

[62] I. H. Campbell and P. M. Fauchet, "The Effects of Microcrystal Size and Shape on the One Phonon Raman Spectra of crystalline semiconductors," *Solid State Commun.*, vol. 58, no. 10, pp. 739–741, 1986.

[63] D. R. Dos Santos and I. L. Torriani, "Crystallite size determination in μc-Ge films by x-ray diffraction and Raman line profile analysis," *Solid State Commun.*, vol. 85, no. 4, pp. 307–310, 1993, doi: 10.1017/CBO9781107415324.004.

[64] C. E. Bottani *et al.*, "Raman, optical-absorption, and transmission electron microscopy study of size effects in germanium quantum dots," *Appl. Phys. Lett.*, vol. 69, no. 16, pp. 2409–2411, 1996.

[65] B. Dorner, H. Grimm, and H. Rzany, "Phonon dispersion branches in α quartz," *J. Phys. C Solid State Phys.*, vol. 13, no. 36, pp. 6607–6613, 1980, doi: 10.1088/0022-3719/13/36/014.

[66] M. E. Striefler and G. R. Barsch, "Lattice dynamics of -quartz," *Phys. Rev. B*, vol. 12, no. 10, pp. 4553–4566, 1975, doi: 10.1103/PhysRevB.12.4553.

[67] J. Etchepare and M. Merian, "Vibrational normal modes of SiO2. III. α-Berlinite (AlPO4) and its relations to Γ-A phonon dispersion curves in α-quartz," *J. Chem. Phys.*, vol. 68, no. 12, pp. 5336–5341, 1977, doi: 10.1063/1.435710.

[68] K. de Boer, A. Jansen, R. van Santen, G. Watson, and S. Parker, "Free-energy calculations of thermodynamic, vibrational, elastic, and structural properties of α-quartz at variable pressures and temperatures," *Phys. Rev. B - Condens. Matter Mater. Phys.*, vol. 54, no. 2, pp. 826–835, 1996, doi: 10.1103/PhysRevB.54.826.

III. ENHANCEMENT OF PLASMON-PHONON COUPLING IN ETCHED ION TRACKS IN α-QUARTZ

Maria C. Garcia Toro a, Miguel L. Crespillo b, Joseph T. Graham a, c.

[a] Nuclear Engineering Program, Missouri University of Science and Technology, 65409, Rolla, MO, United States

[b] Department of Material Science and Engineering, University of Tennessee, 37996, Knoxville, TN, United States

[c] Department of Materials Science and Engineering, Missouri University of Science and Technology, 65409, Rolla, MO, United States

ABSTRACT

This study presents the characterization of a novel plasmonic device. The device was prepared through the drop-wise deposition of a colloidal suspension of gold nanoparticles into etched ion tracks in Y-cut alpha quartz. Scanning Electron Microscopy (SEM) measurements were carried out to verify the presence of nanoparticles inside of the nanowells. Raman spectra of substrates with different nanoparticle concentrations were obtained to study the relationship between Raman intensity and nanoparticle concentration. Analysis of the Raman spectra revealed a Surface-Enhanced Raman Scattering (SERS) response from the quartz substrate in ion irradiated and etched specimens. The enhancement of the Raman scattered intensity was observed to increase linearly with concentration for low concentrations of deposited gold nanoparticles (up to 4×10^6 nps/μL). At higher concentrations, the intensity decreased exponentially with concentration following the Beer-Lambert law. It is believed that the reduction in the

enhancement is caused by light attenuation when the deposited nanoparticle layer becomes thick enough to absorb a significant fraction of the incident laser light. Interestingly, no Raman enhancement was observed when the same concentrations of nanoparticles were deposited on unirradiated and unetched quartz. This suggests that plasmon–phonon coupling may be enhanced through this nanostructure.

1. INTRODUCTION

One of the main goals of modern optoelectronic devices is to enhance performance without increasing size. The incorporation of metallic nanostructures has made it possible to enhance the performance of such devices by introducing light-matter interactions at the nanometric scale [1]. Metallic nanostructures can alter the way light scatters from the molecules thanks to the ability of their optical properties to support collective light-induced electronic excitations (plasmons) [2]–[5]. The free electrons at a metallic surface absorb the energy of the incident photons and begin to oscillate. However, due to the nanometric size of the metallic nanoparticles and the boundary conditions that they impose, such oscillations appear as localized surface plasmons. Localized surface plasmons only absorb incoming light with the same frequencies as the plasmons themselves. Localized surface plasmons are responsible for enhancing the optical response of materials by several orders of magnitude [6]–[9].

Plasmonic nanoparticles strongly modify the phase of the optical field in their vicinity due to their capacity to strongly couple local electron density fluctuations with an electromagnetic field of wavelengths larger than the nanoparticle itself [10]. When these

nanoparticles get closer to each other to a distance comparable to their diameter, additional electromagnetic effects appear [11]–[14]. Plasmon coupling occurs when two or more plasmonic nanoparticles form clusters so that their near-field surface plasmons begin to hybridize and further enhance the localized electric field within the clusters (hot spots). Such clusters also enable the exchange of hot electrons between adjacent nanoparticles. Previous studies have reported an enhancement of the interparticle electric field by several orders of magnitude, far-exceeding the field enhancement created by a single plasmonic nanoparticle [6]–[9]. One of the sensing applications that use plasmon coupling to achieve ultralow detection limits is SERS [15].

Nanoplasmonic devices have been of great interest in physics and engineering and they are expected to be the key in nanotechnology that will merge electronics and conventional photonic components on the same nanodevice [3], [16]–[18].

Nanoplasmonics have been successfully used for nanoantennas [19], [20], efficient solar cells [21]–[23], nanoplasmonic biosensors [24]–[28], SERS [29]–[36], localized heat generation [37]–[40], smart coatings [41]–[45], plasmonic nanofilters [46]–[48], and other useful devices.

Quartz is widely used in optoelectronics and photonic devices. Its optical and electrical properties, in conjunction with its thermostability, high resistance to chemical attack, and its insulating and piezoelectric properties, make quartz a good candidate for diverse applications including semiconductors, construction materials, integrated optics, microelectronics, spectroscopy, and others [49]–[53]. Hence, developing new techniques to modify the optical properties of quartz can represent a promising approach to broaden its technological applications.

The main objective of the present work is to incorporate gold nanoparticles (AuNPs) into the crystal structure of quartz in order to modify its optical response by enhancing the plasmon-phonon coupling via localized surface plasmons. To achieve this, samples of Y-cut orientation alpha quartz were irradiated with highly energetic ions and subsequently vapor-etched with hydrofluoric acid solutions to produce nanowell structures. The production and characterization of latent and etched ion tracks were reported in a companion paper. Gold nanoparticles with a mean diameter of 7 nm were deposited into the etched nanowells by dropping a colloidal suspension on the sample surfaces and allowing them to dry. The characterization of the plasmonic devices included scanning electron microscopy (SEM) and Raman spectroscopy.

2. METHODOLOGY

The samples used in this study consisted of single side polished, Y-cut alpha quartz (MTI inc.). The samples were irradiated with 40 MeV I^{7+} (0.31 MeV/amu) ions to a fluence of 1×10^{9} ions cm^{-2}. The passage of the ions forms ion tracks, disordered/amorphous columnar structures that extend several microns into the quartz surface. After irradiation, the samples were vapor-etched with an aqueous solution of 20%w HF for 1 hour at room temperature. The resulting nanowells had nanochannel shapes with superficial dimensions of ~600 nm in length and~200 nm in width, and depths up to~1 μm. Figure 1 shows SEM images of the nanowells. The micrograph on the left side shows the nanowell openings at the sample surface. The micrograph on the right shows a cross-section where the nanowell depth can be determined. SEM micrographs

were obtained at a high voltage of 15 kV, with a current of 86 pA, a working distance of 4.1 mm, and magnifications ranging between 20,000× and 50,000×. The samples were coated with a 3 nm layer of Au/Pd to inhibit charging, reduce thermal damage, and improve the secondary electron signal required for the topographic examination.

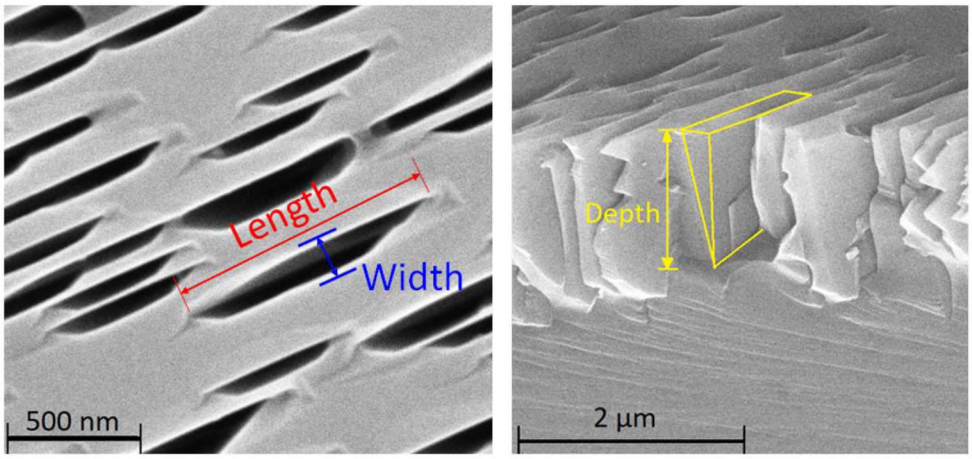

Figure 1. SEM images of irradiated and etched Y-cut α-quartz samples. The nanowell surface dimensions (left) and depth (right) are indicated

Citrate-coated AuNPs with spherical shape and 7 nm diameter were used in the deposition. The AuNPs were purchased from Luna Nanotech as a liquid suspension in water (1.55×10^{-6} M). The citrate coat acts as a stabilizing surfactant to avoid agglomeration (size dispersity:~1.2 nm). The AuNP deposition on the sample surfaces was conducted by dripping 20 µL drops of a diluted suspension (2.3×10^{-8} M in deionized water) onto the samples and letting them dry. Samples with different concentrations of deposited AuNPs were prepared by varying the number of drops. Before depositing a

new drop, the sample's surfaces were cleaned by wiping them with deionized water to remove the nanoparticles that did not get trapped in the nanowells. This procedure was intended to produce devices where the majority of AuNPs reside in the nanowells. Figure 2 shows a photograph of quartz samples with differing AuNPs concentrations: (A) no nanoparticles, (B) 1×10^{6} nanoparticles per microliter (nps/μL), (C) 4×10^{6} nps/μL, (D) 1×10^{7} nps/μL, and (E) 9×10^{7} nps/μL that correspond to a 20 μL-drop of the concentrated suspension (1.55×10^{-6} M).

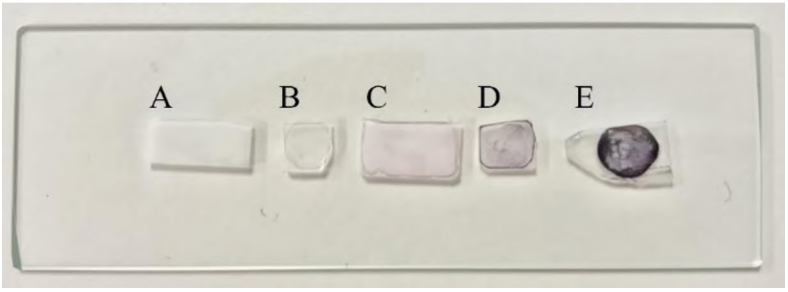

Figure 2. Quartz sample with different AuNP concentrations: (A) no nanoparticles, (B) 1×10^{6} nanoparticles per microliter (nps/μL), (C) 4×10^{6} nps/μL, (D) 1×10^{7} nps/μL, and (E) 9×10^{7} nps/μL corresponding to a 20 μL-drop of the concentrated suspension (1.55×10^{-6} M)

Raman spectra were obtained with a Horiba Xplora Plus Confocal Raman Microscope at room temperature with a 785 nm semiconductor laser. Spectra were collected using a 10× objective lens with an air numerical aperture of 0.25, 1800 lines mm^{-1} grating, and a 100 μm diameter pinhole. Based on these parameters, the index of refraction of quartz and the formulae in [54], an optical sectioning resolution (FWHM) of

about 98.4 μm is assumed. All measurements were acquired in the backscattering geometry without polarization optics.

3. RESULTS

Figure 3 shows an SEM micrograph of a sample with deposited AuNPs at a low concentration (4×10^6 nps/μL). SEM images were taken to characterize the AuNPs distribution after deposition. The micrographs were acquired at high voltage (10 kV), with a current of 43 pA, a working distance of 5.3 mm, and magnitudes ranging between 20,000× and 50,000×. To inhibit charging and improve the secondary electron signal, the samples were coated, but in this case, a 15 nm layer of carbon was used to avoid interference between the Au/Pd coating and the AuNPs.

Agglomeration of AuNPs was observed in the SEM image. This is expected as capillary forces draw NPs together as they dry. Most of the agglomerated AuNPs were found inside the nanowells,. The AuNPs deposition was observed to be nonuniform in the nanowells and several nanowells did not show the presence of AuNPs at all. Also, some of the nanowells that showed the presence of AuNPs were not completely filled at the surface. It is believed that, due to the nanowell geometry, most of the AuNPs fell to the bottom with the possible presence of empty spaces between agglomerated clusters. It was not possible to obtain an SEM cross-section image of the filled nanowells because ion milling can sputter the AuNPs out during the process and contaminate the microscope.

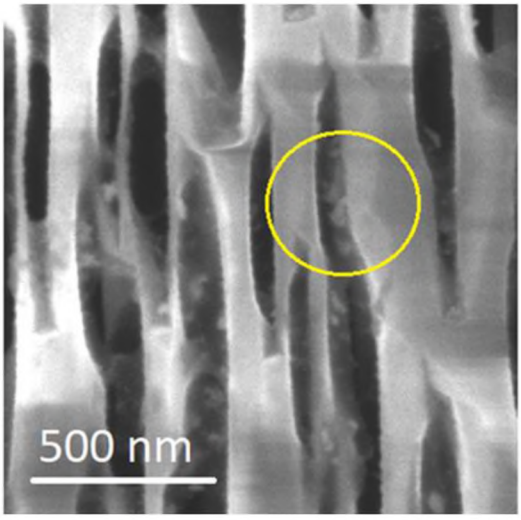

Figure 3. SEM micrograph of a sample with deposited AuNPs

Despite the non-homogeneous AuNP deposition, a modification in the optical response of quartz by the presence of hotspots in agglomerated AuNPs was observed. The enhancement of the electromagnetic field due to plasmon oscillations can occur between as few as two coupled nanoparticles [3], [4], [6]–[10], [55]. Figure 4 shows the Raman spectra of samples with different nanoparticle concentrations. The spectrum of a sample with no AuNPs was included for comparison purposes.

A significant change in the Raman scattering intensities was observed in samples with deposited AuNPs. Samples with a low concentration (up to 4×10^6 nps/μL) of AuNPs presented a roughly linear increase in the Raman signal intensity with concentration. However, at higher concentrations, Raman intensity decreased with increasing concentration. It is believed that, with the increase in deposited-AuNPs, an increase in the number of filled nanowells occurs as does the number of locations where hotspots are in

close proximity to the quartz structure. However, with continued deposition, AuNPs begin to cover the sample surface and block hotspots from new AuNPs from penetrating into the quartz resulting in a saturation of the SERS response. In addition to the saturation of SERS response, continued deposition of AuNPs can produce a decrease in Raman intensity due to light attenuation.

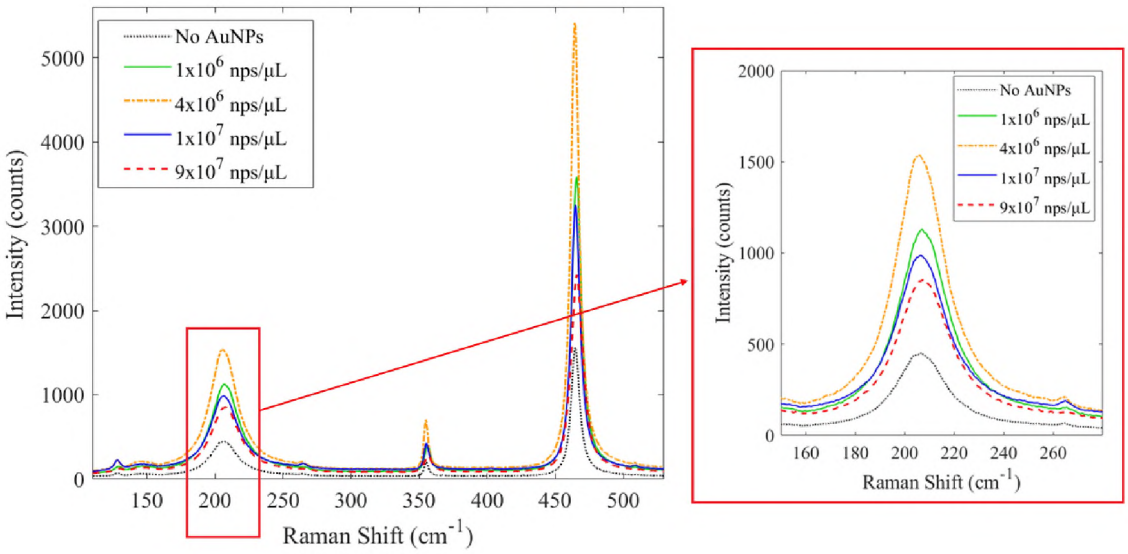

Figure 4. Raman spectra of samples with different AuNP concentrations

The larger number of nanoparticles at the surface increases the mass thickness of gold between the incident laser and the quartz substrate to the point where significant light absorption occurs.

Figure 5 shows the relationship between the enhancement in the localized electromagnetic field with AuNP concentration. The enhancement in the Raman intensity

was evaluated by comparing the measured intensity of the plasmonic devices with the intensity obtained from the samples with no deposited AuNPs. In other words, the enhancement factor was calculated as shown in Equation (1):

$$EF = \frac{I}{I_0} \tag{1}$$

where I is the Raman intensity obtained from the plasmonic devices with different deposited-AuNPs concentrations and I_0 is the Raman intensity obtained from samples without deposited AuNPs. It is important to note that the same Raman microscope conditions were used for all measurements. It is interesting to compare the regime of light attenuation with the Beer-Lambert law shown in Equation (2):

$$\frac{I}{I_0} = e^{-\mu x} \tag{2}$$

μ is the extinction coefficient calculated as 2.854×10^{-7} by fiting the Raman enhancement curve, and x was calculated as the concentration of deposited-AuNPs (nps/μL). As mentioned before, at lower concentrations, the incident light is weakly attenuated and a linear relationship between the EF with the AuNPs concentration was observed (see Figure 6 inset). A maximum EF = 3.41 ± 0.01 was observed at 4×10^{6} nps/μL. The attenuation of light follows an exponential relationship to the AuNPs concentration following the Beer-Lambert law. The Beer-Lambert law from equation 2 is overlayed in

Figure 5. Apart from an intensity, the Beer-Lambert law shows good agreement with the data.

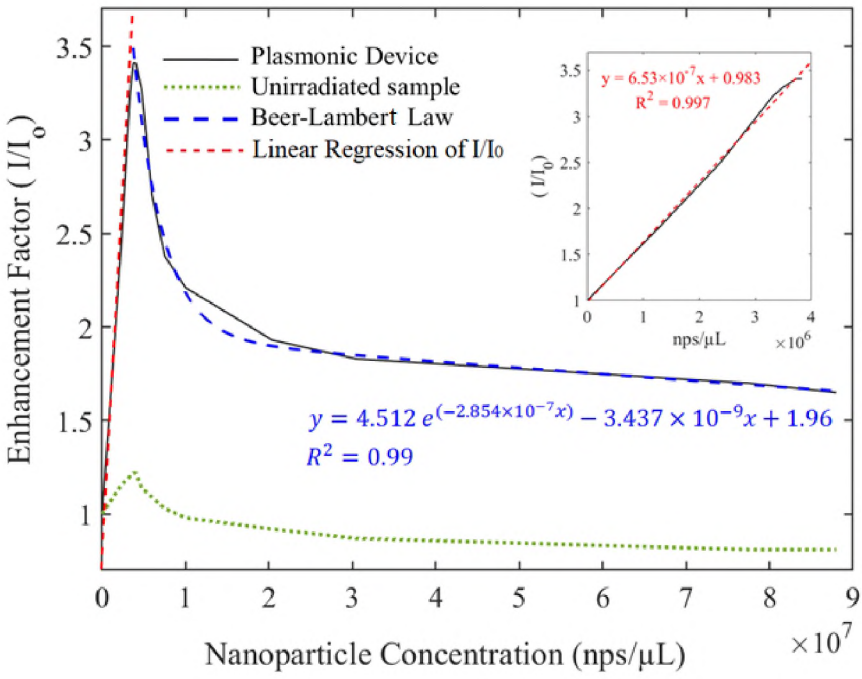

Figure 5. Enhancement in the localized electromagnetic field with AuNP concentration on the plasmonic device

4. CONCLUSIONS

A novel plasmonic device was fabricated and characterized using SEM and Raman spectroscopy. The device comprised a single crystal Y-cut alpha quartz substate with gold nanoparticles deposited into nanowells embedded in its crystal structure. The nanowells were produced by chemical vapor-etching of ion tracks that were obtained

after high energy ion irradiation. The gold nanoparticles produced hotspots that reinforce the electromagnetic field via localized surface plasmons at the nanoparticle surface. The modification in the optical response of the plasmonic device was evaluated by Raman spectroscopy. An increase in the Raman scattering intensity was observed with an increase in AuNP concentration up to 4×10^6 nps/μL. A maximum enhancement factor of 3.4 was observed. For higher nanoparticle concentrations, an exponential reduction in the Raman intensity from light absorption in the AuNPs followed the Beer-Lambert Law. Similar enhancement behavior was not revealed in spectra from unirradiated and unetched quartz when nanoparticles were deposited. This particular nanostructure may be used to couple electromagnetic radiation to optical phonons near the surface of quartz via localized surface plasmons. Moreover, as quartz has piezoelectric properties, the coupling between external electromagnetic radiation and the displacement field of quartz should be studied. Further studies may also investigate the effects of crystal orientation and the geometry of nanowells on the enhancement factor; the effects of interparticle separation, agglomeration, and uniformity; and characterization of other optical properties such as polarization, reflectance, and absorbance and the spectral dependence of these properties.

ACKNOWLEDGMENTS

This work was supported by the Nuclear Regulatory Commission Faculty Development Grant NRC-HQ-84-15-G-0044. M.L.C. acknowledges support from the University of Tennessee Governor's Chair program. The authors are grateful to the staff in The Centro de Microanálisis de Materiales - Universidad Autónoma de Madrid for

assistance with experimental irradiations. Also, the authors want to thank the Materials Research Center (MRC) at Missouri S&T for its support and use of equipment.

REFERENCES

[1] M. L. Brongersma and V. M. Shalaev, "The Case for Plasmonics," *Science (80-.).*, vol. 328, no. 5977, pp. 440–441, 2010.

[2] W. L. Barnes, A. Dereux, and T. W. Ebbesen, "Surface plasmon subwavelength optics," *Nature*, vol. 424, no. 6950, pp. 824–830, 2003.

[3] N. J. Halas, "Plasmonics : An Emerging Field Fostered by Nano Letters," *Nano Lett.*, vol. 10, no. 10, pp. 3816–3822, 2010, doi: 10.1021/nl1032342.

[4] W. A. Murray and W. L. Barnes, "Plasmonic Materials **," *Adv. Mater.*, vol. 19, no. 22, pp. 3771–3782, 2007, doi: 10.1002/adma.200700678.

[5] M. Moskovits, "Surface roughness and the enhanced intensity of Raman scattering by molecules adsorbed on metals," *J. Chem. Phys.*, vol. 69, no. 9, pp. 4159–4161, 1978.

[6] T. Chen, M. Pourmand, A. Feizpour, B. Cushman, and B. M. Reinhard, "Tailoring Plasmon Coupling in Self-Assembled One-Dimensional Au Nanoparticle Chains through Simultaneous Control of Size and Gap Separation," *J. Phys. Chem. Lett.*, vol. 4, no. 13, pp. 2147–2152, 2013, doi: 10.1021/jz401066g.

[7] T. Chung *et al.*, "Nanoislands as plasmonic materials," *Nanoscale*, vol. 11, no. 18, pp. 8651–8664, 2019, doi: 10.1039/c8nr10539a.

[8] H. Yu *et al.*, "Near-field spectral properties of coupled plasmonic nanoparticle arrays," *Opt. Express*, vol. 25, no. 6, pp. 6883–6894, 2017.

[9] Y. Sonnefraud, A. L. Koh, D. W. Mccomb, and S. A. Maier, "Nanoplasmonics : Engineering and observation of localized plasmon modes," *Laser Photonics Rev.*, vol. 6, no. 3, pp. 277–295, 2012, doi: 10.1002/lpor.201100027.

[10] P. K. Jain and M. A. El-sayed, "Plasmonic coupling in noble metal nanostructures," *Chem. Phys. Lett.*, vol. 487, no. 4–6, pp. 153–164, 2010.

[11] Z. Fang *et al.*, "Evolution of Light-Induced Vapor Generation at a Liquid-Immersed Metallic Nanoparticle," *Nano Lett.*, vol. 13, no. 4, pp. 1736–1742, 2013, doi: 10.1021/nl4003238.

[12] E. M. Larsson, C. Langhammer, I. Zorić, and B. Kasemo, "Nanoplasmonic Probes of Catalytic Reactions," *Science (80-.).*, vol. 326, no. 5956, pp. 1091–1094, 2009.

[13] E. Lukianova-Hleb *et al.*, "Plasmonic Nanobubbles as Transient Vapor Nanobubbles Generated around Plasmonic Nanoparticles," *ACS Nano*, vol. 4, no. 4, pp. 2109–2123, 2010, doi: 10.1021/nn1000222.

[14] A. L. Lereu, R. H. Farahi, L. Tetard, S. Enoch, T. Thundat, and A. Passian, "Plasmon assisted thermal modulation in nanoparticles," *Opt. Express*, vol. 21, no. 10, pp. 12145–12158, 2013, doi: 10.1364/OE.21.012145.

[15] R. Pilot, R. Signorini, C. Durante, L. Orian, M. Bhamidipati, and L. Fabris, "A Review on Surface-Enhanced Raman Scattering," *Biosensors*, vol. 9, no. 2, p. 57, 2019.

[16] Z. Liang, J. Sun, Y. Jiang, and L. Jiang, "Plasmonic Enhanced Optoelectronic Devices," *Plasmonics*, vol. 9, no. 4, pp. 859–866, 2014, doi: 10.1007/s11468-014-9682-7.

[17] E. Ozbay, "Plasmonics : Merging Photonics and Electronics at Nanoscale Dimensions," *Science (80-.).*, vol. 311, no. 5758, pp. 189–193, 2006.

[18] L. Jiang *et al.*, "Free-standing one-dimensional plasmonic nanostructures," *Nanoscale*, vol. 4, no. 1, pp. 66–75, 2012, doi: 10.1039/c1nr11445j.

[19] X. Ni, N. K. Emani, A. V Kildishev, A. Boltasseva, and V. M. Shalaev, "Broadband Light Bending with Plasmonic Nanoantennas," *Science (80-.).*, vol. 335, no. 6067, p. 427, 2012, doi: 10.1126/science.1214686.

[20] V. Giannini, A. I. Fernández-Domínguez, S. C. Heck, and S. A. Maier, "Plasmonic Nanoantennas : Fundamentals and Their Use in Controlling the Radiative Properties of Nanoemitters," *Chem. Rev.*, vol. 111, no. 6, pp. 3888–3912, 2011, doi: 10.1021/cr1002672.

[21] S. Pillai and M. A. Green, "Plasmonics for photovoltaic applications," *Sol. Energy Mater. Sol. Cells*, vol. 94, no. 9, pp. 1481–1486, 2010, doi: 10.1016/j.solmat.2010.02.046.

[22] V. E. Ferry *et al.*, "Light trapping in ultrathin plasmonic solar cells," *Opt. Express*, vol. 18, no. 102, pp. A237–A245, 2010.

[23] P. Reineck, G. P. Lee, D. Brick, M. Karg, P. Mulvaney, and U. Bach, "A Solid-State Plasmonic Solar Cell via Metal Nanoparticle," *Adv. Mater.*, vol. 24, no. 35, pp. 4750–4755, 2012, doi: 10.1002/adma.201200994.

[24] M. C. Estevez, M. A. Otte, B. Sepulveda, and L. M. Lechuga, "Trends and challenges of refractometric nanoplasmonic biosensors : A review," *Anal. Chim. Acta*, vol. 806, pp. 55–73, 2014, doi: 10.1016/j.aca.2013.10.048.

[25] G. A. Lopez, M. C. Estevez, M. Soler, and L. M. Lechuga, "Recent advances in nanoplasmonic biosensors : applications and lab-on-a-chip integration," *Nanophonics*, vol. 6, no. 1, pp. 123–136, 2017, doi: 10.1515/nanoph-2016-0101.

[26] A. H. Nguyen and S. J. Sim, "Nanoplasmonic biosensor : Detection and amplification of dual bio-signatures of circulating tumor DNA," *Biosens. Bioelectron.*, vol. 67, pp. 443–449, 2015, doi: 10.1016/j.bios.2014.09.003.

[27] J. Li *et al.*, "Revisiting the Surface Sensitivity of Nanoplasmonic Biosensors," *Acs Photonics*, vol. 2, no. 3, pp. 425–431, 2015, doi: 10.1021/ph5004779.

[28] A. A. Yanik *et al.*, "An Optofluidic Nanoplasmonic Biosensor for Direct Detection of Live Viruses from Biological Media," *Nano Lett.*, vol. 10, no. 12, pp. 4962–4969, 2010, doi: 10.1021/nl103025u.

[29] R. Goul *et al.*, "Quantitative analysis of surface enhanced Raman spectroscopy of Rhodamine 6G using a composite graphene and plasmonic Au nanoparticle substrate," *Carbon N. Y.*, vol. 111, pp. 386–392, 2017, doi: 10.1016/j.carbon.2016.10.019.

[30] K. Kneipp *et al.*, "Single Molecule Detection Using Surface-Enhanced Raman Scattering (SERS)," *Phys. Rev. Lett.*, vol. 78, no. 9, pp. 1667–1670, 1997.

[31] J. B. Jackson and N. J. Halas, "Surface-enhanced Raman scattering on tunable plasmonic nanoparticle substrates," *Proc. Natl. Acad. Sci.*, vol. 101, no. 52, pp. 17930–17935, 2004.

[32] P. P. Patra, R. Chikkaraddy, R. P. N. Tripathi, A. Dasgupta, and G. V. P. Kumar, "Plasmofluidic single-molecule surface-enhanced Raman scattering from dynamic assembly of plasmonic nanoparticles," *Nat. Commun.*, vol. 5, no. 1, pp. 1–8, 2014, doi: 10.1038/ncomms5357.

[33] M. Moskovits, "Surface-enhanced spectroscopy," *Rev. Mod. Phys.*, vol. 57, no. 3, p. 783, 1985.

[34] S. Nie and S. R. Emory, "Probing Single Molecules and Single Nanoparticles by Surface-Enhanced Raman Scattering," *Science (80-.).*, vol. 275, 1997.

[35] A. M. Michaels, M. Nirmal, and L. E. Brus, "Surface Enhanced Raman Spectroscopy of Individual Rhodamine 6G Molecules on Large Ag Nanocrystals," *J. Am. Chem. Soc.*, vol. 121, no. 43, pp. 9932–9939, 1999, doi: 10.1021/ja992128q.

[36] Z. Wang, S. Pan, T. D. Krauss, H. Du, and L. J. Rothberg, "The structural basis for giant enhancement enabling single-molecule Raman scattering," in *Proceedings of the National Academy of Science*, 2003, vol. 100, no. 15, pp. 8638–8643.

[37] U. Guler *et al.*, "Local Heating with Lithographically Fabricated Plasmonic Titanium Nitride Nanoparticles," *Nano Lett.*, vol. 13, no. 12, pp. 6078–6083, 2013, doi: 10.1021/nl4033457.

[38] G. Baffou, J. Polleux, H. Rigneault, and S. Monneret, "Super-Heating and Micro-Bubble Generation around Plasmonic Nanoparticles under cw Illumination," *J. Phys. Chem. C*, vol. 118, no. 9, pp. 4890–4898, 2014, doi: 10.1021/jp411519k.

[39] I. Alessandri and L. E. Depero, "Using plasmonic heating of gold nanoparticles to generate local SER(R)S-active TiO2 spots," *Chem. Commun.*, vol. 17, pp. 2359–2361, 2009, doi: 10.1039/b900647h.

[40] X. Huang, P. K. Jain, I. H. El-sayed, and M. A. El-Sayed, "Plasmonic photothermal therapy (PPTT) using gold nanoparticles," *Lasers Med. Sci.*, vol. 23, no. 3, pp. 217–228, 2008, doi: 10.1007/s10103-007-0470-x.

[41] Q. Hao *et al.*, "VO2/TiN Plasmonic Thermochromic Smart Coatings for Room-Temperature Applications," *Adv. Mater.*, vol. 30, no. 10, pp. 1705421(1–5), 2018, doi: 10.1002/adma.201705421.

[42] A. Tittl *et al.*, "Plasmonic Smart Dust for Probing Local Chemical Reactions," *Nano Lett.*, vol. 13, no. 4, pp. 1816–1821, 2013, doi: 10.1021/nl4005089.

[43] G. Garcia, R. Buonsanti, A. Llordes, E. L. Runnerstrom, A. Bergerud, and D. J. Milliron, "Near-Infrared Spectrally Selective Plasmonic Electrochromic Thin Films," *Adv. Opt. Mater.*, vol. 1, no. 3, pp. 215–220, 2013, doi: 10.1002/adom.201200051.

[44] Q. Liu, Y. Yuan, and I. I. Smalyukh, "Electrically and Optically Tunable Plasmonic Guest–Host Liquid Crystals with Long-Range Ordered Nanoparticles," *Nano Lett.*, vol. 14, no. 7, pp. 4071–4077, 2014, doi: 10.1021/nl501581y.

[45] X. Zhang *et al.*, "Optical polarizers based on gold nanowires fabricated using colloidal gold nanoparticles," *Nanotechnology*, vol. 19, no. 28, pp. 285202(1–6), 2008, doi: 10.1088/0957-4484/19/28/285202.

[46] M. G. Campbell, Q. Liu, A. Sanders, J. S. Evans, and I. I. Smalyukh, "Preparation of Nanocomposite Plasmonic Films Made from Cellulose Nanocrystals or Mesoporous Silica Decorated with Unidirectionally Aligned Gold Nanorods," *Materials (Basel).*, vol. 7, no. 4, pp. 3021–3033, 2014, doi: 10.3390/ma7043021.

[47] Y. Leroux *et al.*, "Active Plasmonic Devices with Anisotropic Optical Response : A Step Toward Active Polarizer," *Nano Lett.*, vol. 9, no. 5, pp. 2144–2148, 2009, doi: 10.1021/nl900695j.

[48] M. Ye *et al.*, "Angle-insensitive plasmonic color filters with randomly distributed silver nanodisks," *Opt. Lett.*, vol. 40, no. 21, pp. 4979–4982, 2015.

[49] C. L. Phillips, R. J. Magyar, and P. S. Crozier, "A two-temperature model of radiation damage in α -quartz," *J. Chem. Phys.*, vol. 133, no. 14, 2010, doi: 10.1063/1.3481356.

[50] U. Utzinger and R. R. Richards-Kortum, "Fiber optic probes for biomedical optical spectroscopy," *J. Biomed. Opt.*, vol. 8, no. 1, p. 121, 2003, doi: 10.1117/1.1528207.

[51] F. P. Bolin, L. E. Preuss, R. C. Taylor, and R. J. Ference, "Refractive index of some mammalian tissues using a fiber optic cladding method," *Appl. Opt.*, vol. 28, no. 12, pp. 2297–2303, 1989.

[52] C. Stambaugh, H. Shakeel, D. Kalteyer, P. Abbott, and J. Pomeroy, "Traceability of frequency based mass measurements using a quartz crystal microbalance," *J. Phys. Conf. Ser.*, vol. 1065, no. 4, 2018, doi: 10.1088/1742-6596/1065/4/042002.

[53] M. Blomqvist, O. Blomster, M. Palsson, S. Campbell, F. Becker, and W. Rath, "All-in-quartz optics for low focal shifts," in *Proceedings Volume 7912, Solid State Lasers XX: Technology and Devices*, 2011, doi: 10.1117/12.874597.

[54] T. Wilson, "Resolution and optical sectioning in the confocal microscope," *J. Microsc.*, vol. 244, no. 2, pp. 113–121, 2011, doi: 10.1111/j.1365-2818.2011.03549.x.

[55] J. A. Schuller, E. S. Barnard, W. Cai, Y. C. Jun, J. S. White, and M. L. Brongersma, "Plasmonics for extreme light concentration and manipulation," *Nat. Mater.*, vol. 9, no. 3, pp. 193–204, 2010, doi: 10.1038/nmat2630.

SECTION

3. PARALLEL STUDY CONDUCTED IN AMORPHOUS SiO_2

As mentioned in the introduction, most of the previous studies about latent and etched ion tracks in SiO_2 have been conducted on the amorphous form, fused silica. These studies include detailed analysis of ion track formation [130], [133], the evolution of the damage induced by ion-irradiation [134], the effect of deposited energy density on the ion track radius [112], the mechanical response [63] and plastic deformation [58] of SiO_2 after ion irradiation, and etching mechanism under different etching conditions [62], [64], [67], [120]. Therefore, the same experimental procedure used in this study was conducted on fused silica samples to create a reference point for the results obtained with α-SiO_2 and to validate the used experimental methodology.

Fused silica samples, from MTI corporation, were irradiated at the CMAM-UAM with 40 MeV I^{7+} ions at fluences of 1×10^{9}, 1×10^{10}, and 1×10^{11} ions cm^{-2}, and etched at room temperature with solutions of 10, 20, and 30%w HF and different etching times. The irradiated and subsequently etched samples showed similar results, with a few significant differences, when compared with α-SiO_2.

The first difference observed was related to the formation of hillocks at the irradiated sample surface. The AFM measurements taken from irradiated α-SiO_2 showed hillocks at the sample surface as a consequence of swelling and decrease in density produced by the passage of energetic ions (See Section 2.1). On the other hand, it was difficult to identify the formation of hillocks at the sample surface of irradiated fused

silica by atomic force microscopy (AFM) measurements. According to previous studies [56], [62], [88], [112], [115], ion irradiation of amorphous substrates produces densification and plastic deformation of the material, not expansion. This means the silica samples had higher density (more compact) ion tracks that did not produce hillocks at the sample surface. The previous studies have reported that amorphous and crystalline SiO_2 have a similar electronic stopping power threshold (2 – 5 keV/nm). Hence, ion tracks with similar diameters and depths can be expected in both silica and α-SiO_2 though it may be difficult to observe tracks in fused silica with AFM.

The second difference was found in the nanowells formed after etching the fused silica samples. Vapor-etching was conducted following the same experimental procedure as the one used for α-SiO_2 (see Paper I). Aqueous solutions of HF at 10, 20, and 30%w HF were used with etching times up to 1 hour. As observed after etching α-SiO_2, the fused silica samples irradiated with 1×10^{11} ions cm^{-2} exhibited high surface damage even when etching with the lower acid concentration and short etching times (< 10 minutes). This is expected in the overlapping track regime. Therefore, to produce isolated nanowells, the etching process was conducted on samples irradiated with fluences of 1×10^{9} cm^{-2} and 1×10^{10} cm^{-2}. Also, samples etched with 30%w HF were highly sensitive to acid attack, making it difficult to control the etching rate because the bulk material (zones without ion tracks) was being etched at the same time. The best results were observed on samples etched with 20%w HF up to 10 minutes. Longer etching times produced greater surface modification and the nanowells began to exhibit agglomeration.

The formation of nanowells was successfully observed. However, instead of showing facetted openings, the nanowells had circular openings and conical shapes in the

solid even when using the higher acid concentration with longer etching time. It is believed that the circular shape of the opening is caused by the absence of a crystal structure; the random position of the oxygen atoms gives rise to isotropic etching behavior (as explained in Section 2.3).

Figure 3.1 shows, at the left, an SEM micrograph of a silica sample that was irradiated with 40 MeV I^{7+} at 1×10^{9} ion cm^{-2} and subsequently etched with 10%w HF for 10 minutes. The nanowells superficial diameters and depths were measured with AFM are shown on the right. The SEM micrograph was obtained at high voltage of 15 kV, with a current of 86 pA, a working distance of 4.1 mm, and a magnification of 35,000×. The sample was coated with a 3 nm layer of Au/Pd to inhibit charging, reduce thermal damage, and improve the secondary electron signal required for the topographic examination.

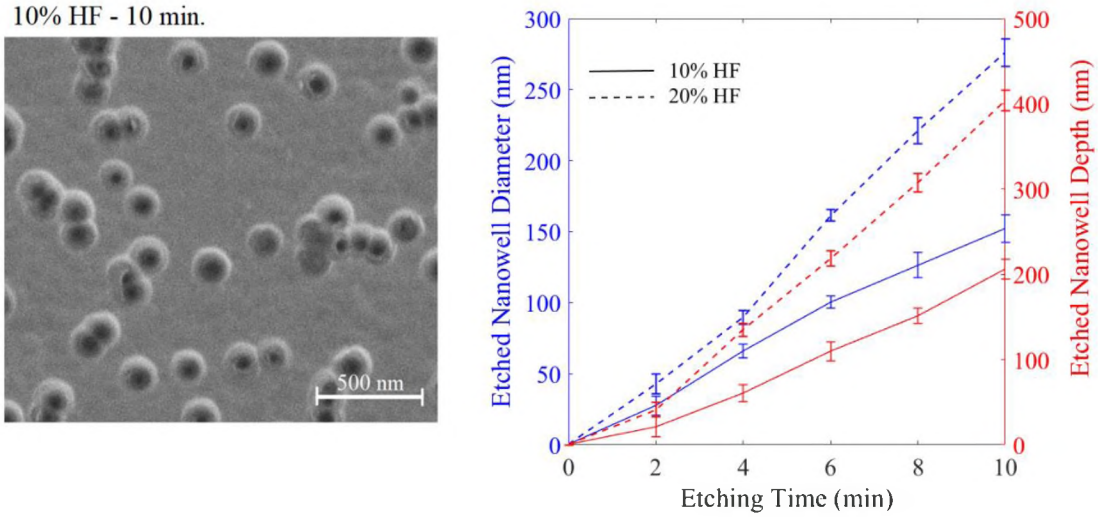

Figure 3.1. (Left) SEM micrograph of a silica sample irradiated with 40 MeV I^{7+} ion at 1×10^{9} ions cm^{-2} and etched with 10% HF for 10 minutes. (right) Analysis of the nanowell superficial diameter and depths obtained after etching with 10% and 20% HF for different etching times

It was found that the depths and diameters increase with acid concentration, as observed when etching α-SiO_2. The etching rates were ~15 nm/min (superficial diameter) and ~20 nm/min (depth) for samples etched with 10% HF, and ~27 nm/min (superficial diameter) and ~40 nm/ min (depth) for samples etched with 20% HF. The calculated aspect ratios (depth/diameter) were 1.3 and 1.5 respectively and were slightly higher than the nanowell aspect ratios obtained from etching α-SiO_2 with similar acid concentrations.

The deposition of gold nanoparticles (AuNPs) was conducted by drying drops of a diluted colloidal solution (23 nM) as explained in Paper III. Samples that were etched with 20% HF for 10 minutes were used (superficial diameter: ~250 nm, depths up to 400 nm). The main objective of this part of the experiments was to deposit the nanoparticles inside of the etched nanowells while avoiding nanoparticle deposition on the sample surface. The characterization techniques included AFM, SEM, and energy dispersive spectroscopy (EDS). It is important to mention that, for both crystalline and amorphous SiO_2, the main challenge obtained during sample characterization was resolving the nanoparticle. The size of the nanoparticles, being just 7 nm, was smaller than the resolution of the types of equipment used. AFM can detect features at that nanometric scale, but, due to the dimensions of the obtained nanowells in both kinds of samples, it was not possible to identify single nanoparticles given the topographic variations in the surface of the etched silica. Moreover, AFM does not provide mass or elemental contrast. Therefore, the analysis was conducted considering the observation of agglomerated nanoparticles at the sample surfaces.

The AFM measurements were conducted to check how the nanowell depths change after depositing AuNPs. It was observed that the deposition process was not

homogeneous on the sample substrates, as observed in the α-SiO_2 samples. Several nanowells were completely filled to sample surface while others were partially filled (mostly at the walls of the nanowells) or empty. Figure 3.2 shows the AFM images for a silica sample after depositing 4×10^6 nps/μL, (A) sample surface, (B) 3D-surface analysis, and (C) the section analysis of the ion tracks found in the selected area. The chosen nanoparticle concentration was the same as the one found to produce the highest Raman enhancement in the α-SiO_2 (EF = 3.4).

Thanks to the consistent conical shape of the nanowells, it was easier to analyze the changes in depth after the AuNPs deposition. The AFM profile (image C) from Figure 3.1 clearly shows how the depth of some nanowells changes after the deposition process. It is still possible, however, that empty spaces are produced in the nanowell due to non-uniform nanoparticle agglomeration. A better characterization technique is needed to analyze the nanoparticle distribution inside of the nanowell, as suggested in Paper III.

The same AFM analysis conducted on α-SiO_2 samples after depositing AuNPs was more difficult to interpret. It was not possible to clearly observe isolated filled nanowells due to the agglomeration of etched nanowells and formation of linked nanochannels. Figure 3.3 showed different AFM profiles taken from the same nanowell that was partially filled with AuNPs. Variations in nanowell depth could indicate non-homogeneous AuNPs deposition and agglomeration (as with fused silica). However, it needs to be reiterated that the etched nanowells/nanochannels in quartz were less uniform in size and it is difficult to differentiate between filled nanowells and unfilled nanowells that are merely more shallow and narrow. Moreover, a clearly defined opening “lip” was difficult to observe in the quartz nanowells. The same lip can be seen in Figure 3.2(A).

Hence, the need for a better characterization technique to analyze the nanoparticle distribution inside of the nanowell is reinforced.

Figure 3.4 shows an SEM micrograph of a fused silica sample with deposited AuNPs (4×10^6 nps/µL). The micrographs were acquired at a high voltage of 10 kV, with a current of 43 pA, a working distance of 5.3 mm, and magnifications ranging between 20,000× and 50,000×.

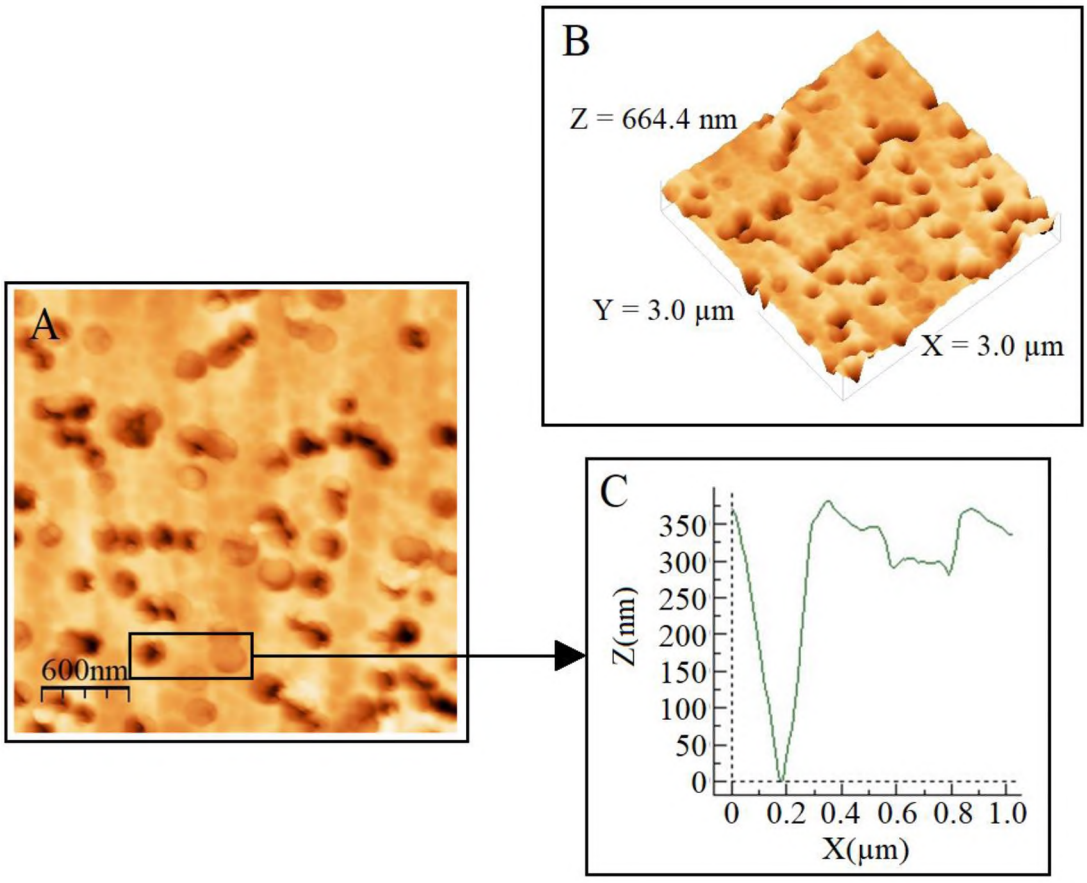

Figure 3.2. AFM images for a silica sample after depositing $4x10^6$ nps/µL, (A) sample surface, (B) 3D-surface analysis, and (C) the section analysis of the ion tracks found in the selected area

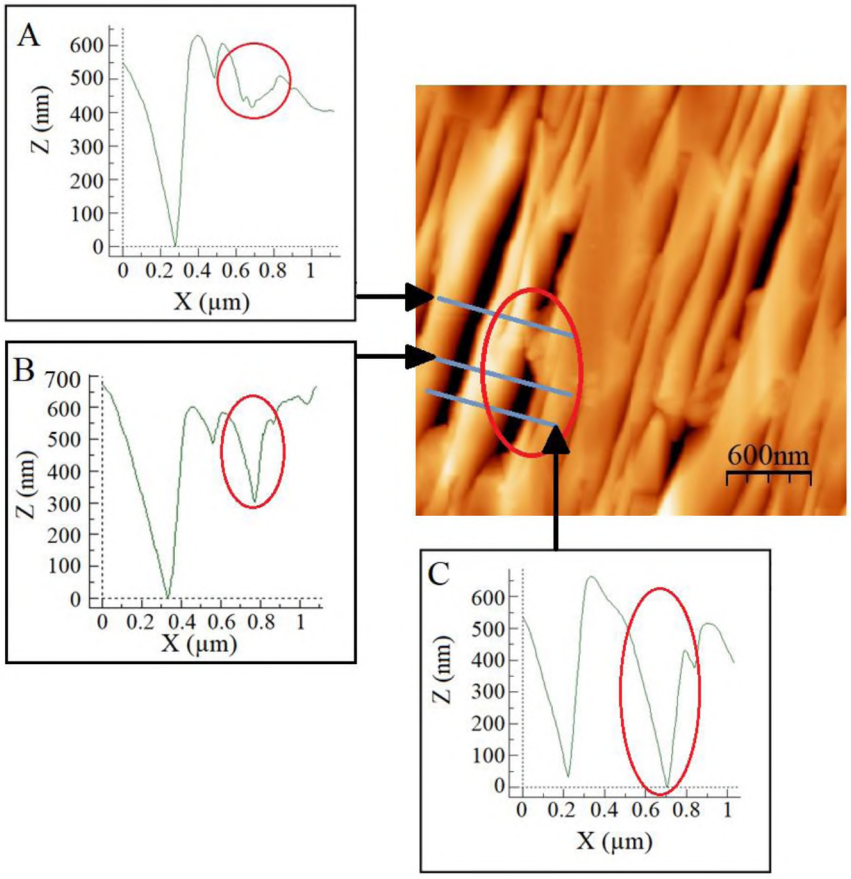

Figure 3.3. AFM depth profiles of a nanowell with deposited AuNPs. (A) depth profile of AuNPs seeing close to the sample surface. (B) and (C) depth profiles of AuNPs probably at the nanowell bottom

To inhibit charging and improve the secondary electron signal, the samples were coated with 15 nm layer of carbon. Carbon was chosen instead of Au/Pd to prevent the coating from interfering with the AuNPs in EDS analysis. Through comparison with the SEM image of Figure 3.1 (left), it is possible to identify the filled nanowells and empty nanowells. Also, it was possible to confirm that the nanowell shape and dimensions favored the filling process when compared with the SEM micrographs obtained from α-

SiO_2 (Figure 3 from Paper II), though possibly this is, in part, a consequence of the surface area and volume difference between the two nanowell shapes.

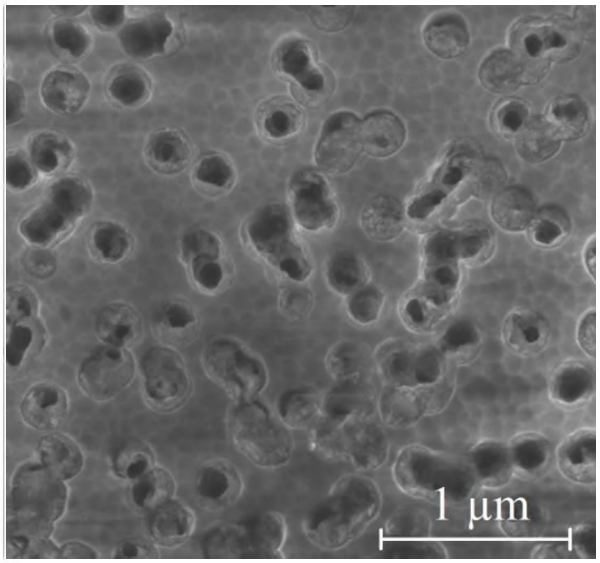

Figure 3.4. SEM micrograph of a silica sample with deposited AuNPs (4×10^6 nps/μL)

From the SEM micrograph, one can conclude that no significant amount of agglomerated nanoparticles was observed at the sample surface while it was possible to detect AuNPs agglomeration in the nanowells. However, due to the large scales used during the AFM and SEM measurements, and the lack of single AuNPs detection, An EDS analysis was conducted to verify if AuNPs are present on the sample surface.

EDS spectra were taken from the inside of the filled nanowells as well as from the sample surfaces between nanowells. Figure 3.5 shows the EDS spectra taken from a silica sample surface (spectrum 6) where no nanowell was observed, and the EDS analysis

taken from a filled nanowell (spectrum 7). Table 3.1 shows the EDS report for each spectrum where the characteristics X-ray lines (line type), the apparent concentration, ratio of the intensity (number of X-ray counts – k ratio (ratio of characteristic intensities measured on the specimen and standard)), the element concentration in terms of the mass fraction (Wt%), its error (Wt% Sigma), and the atomic weight percent (Atomic %) are included. It was observed that the EDS analysis did not detect the presence of AuNPs at the sample surface. Thus the methodology used to deposit gold nanoparticles successfully produced clean silica surfaces with AuNPs residing wholly within the nanowells.

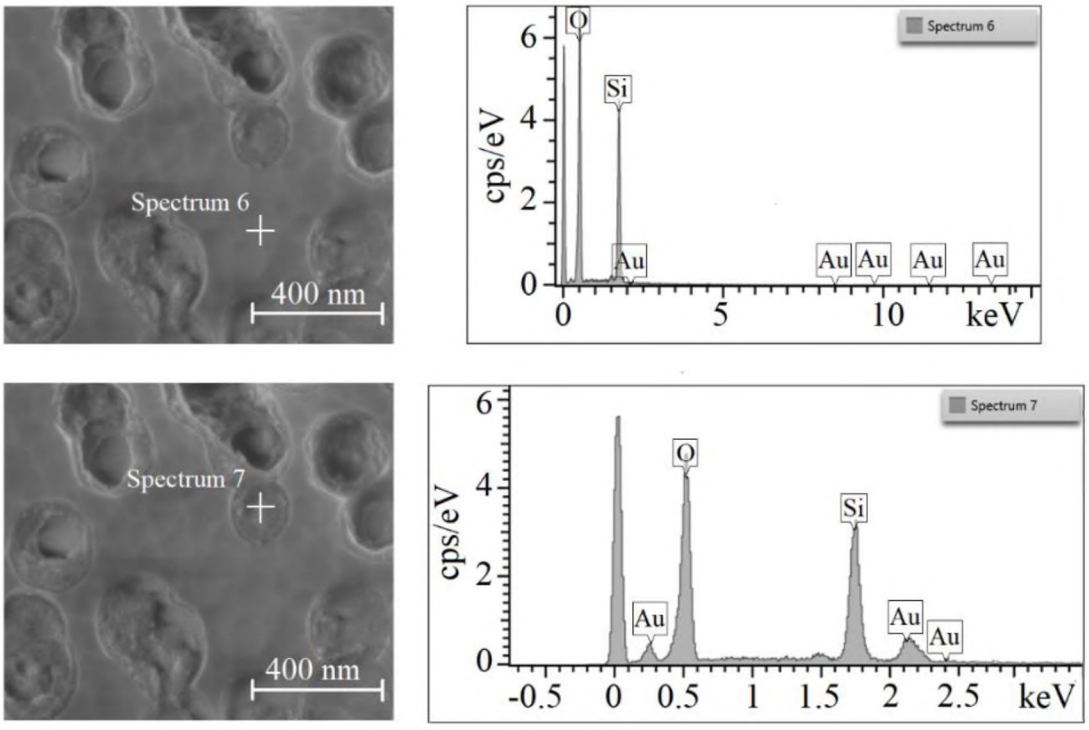

Figure 3.5. EDS spectra taken from a silica sample after depositing AuNPs. (Top – spectrum 6) EDS analysis was taken from the sample surface. (Bottom – spectrum 7) EDS analysis was taken from a filled nanowell

Table 3.1. EDS reports from silica samples with deposited AuNPs

	Element	Line Type	Apparent Concentration	k Ratio	Wt%	Wt% Sigma	Atomic %	Standard Label
Spectro 6	O	K	5.86	0.02	67.4	0.5	78.4	SiO2
	Si	K	1.87	0.01	32.6	0.5	21.6	SiO2
	Au	M	0.00	0.00	0.0	0.5	0.0	Au
	Total:				100.0		100.0	
Spectro 7	O	K	3.98	0.01	57.6	0.9	78.7	SiO2
	Si	K	1.35	0.01	24.4	0.6	19.2	SiO2
	Au	M	0.64	0.01	18.0	1.0	2.1	Au
	Total:				100.0		100.0	

Considering the previous studies of latent and etched ion tracks in amorphous SiO_2 and the results shown in this section, it was possible to create a reference point for comparing the results obtained with α-SiO_2. This section verifies that the methodology used in this thesis was suitable to build the plasmonic device using α-SiO_2 as the main substrate. Additionally, it shows that plasmonic devices may also be easy to fabricate in fused silica. Certainly, much additional work could be dedicated to this one topic.

4. SUMMARY AND CONCLUSIONS

The fabrication of a plasmonic device using single crystals of alpha quartz was successfully accomplished. The device consisted of Y-cut α-SiO_2 samples with deposited gold nanoparticles into nanowells embedded in its crystal structure. The nanowells were produced by chemical vapor-etching of ion tracks that were obtained after irradiating with highly energetic ions. The deposited gold nanoparticles modified the optical response of α-SiO_2 thanks to the creation of hotspots in the interparticle spaces. Such hotspots enhance the electromagnetic field via localized surface plasmons at the nanoparticle surface. Raman measurements showed that such hotspots were effective in enhancing the coupling between external electromagnetic radiation and optical phonons. As quartz is one of the most used materials in optoelectronics and photonics applications and considering plasmonic devices as a promising technology for nanophotonics, this work represents a promising approach to broaden these technological applications and to make quartz a promising material for nanophotonics.

The experiments can be divided into three main sections: the production of latent ion tracks by high energy ion irradiation in electronic energy loss regime, chemical vapor-etching of ion tracks to create nanowells, and the deposition of gold nanoparticles into the nanowells. It is important to note that experiments were conducted using two different sample orientations (Y-cut and Z-cut) to determine which one produces a more suitable substrate for deposition and creation of the plasmonic device. Additionally, a detailed analysis of the phonon confinement effect produced by the presence of latent and etched ion tracks in the crystal structure was conducted.

Latent ion tracks were produced by irradiating α-SiO_2 samples with both 20 MeV Ni^{6+} ions and 40 MeV I^{7+} ions at different fluences. The species and energies of the ions were chosen considering that permanent changes in the crystal structure occur when the electronic stopping power exceeds a critical threshold required to form highly defective or amorphous zones in the crystal matrix. It was found that the irradiation conditions produced continuous and homogeneous ion tracks. After irradiating, it was possible to observe hillocks at the sample surface, a consequence of the amorphization process. Hillocks of similar height and width were observed in both Y- and Z-cut samples. The hillock morphology depends on the stopping power, track depth, and perhaps ion velocity to a lesser extent. Samples irradiated with 20 MeV Ni^{6+} had broader hillocks and presumably wider tracks. Samples irradiated with 40 MeV I^{7+} ions produced deeper ion tracks with smaller hillock diameters.

Chemical vapor-etching was conducted with aqueous solutions of HF at different concentrations. It was found that Z-cut samples etched at significantly faster rates. Low acid concentrations (<10% HF) were needed to conduct an etching process in a controlled manner and without damaging the surface of the samples. Under those etching conditions, it was possible to obtain conical-shaped nanowells with superficial dimensions up to ~ 140 nm width and depths of around ~ 15 nm. The Y-cut samples showed higher resistance to acid attack, allowing etching with higher acid concentrations (up to 30%w HF) and longer etching times (up to 1 hour). During etching, strong anisotropic etching behavior was observed. Nanowells produced during the first 15 minutes were roughly lenticular in shape. After longer etching times, the nanowells began to elongate in the Z direction, eventually agglomerating into nanochannels.

Different kinetic regimes were identified in all etched samples. Initially, the etching process is rapid and occurs primarily along the track core. This is followed by a slower regime where the growth of the superficial dimension(s) increases. For Y-cut quartz, a third, fast etching regime was also observed at longer etching times as a consequence of agglomeration of channels, which creates a relatively open structure that may improve HF transport. The ion energy and stopping power are believed to explain differences in the nanowell aspect ratio. Samples that were irradiated with 20 MeV Ni^{6+} ions presented shallower nanowells with broader diameters than those irradiated with 40 MeV I^{7+}. Though the ion velocities were similar, the stopping power of the iodine ions was higher, possibly resulting in more defective/amorphous track cores. Higher aspect ratios could also be achieved at higher etchant concentrations. At this point, it was possible to identify the Y-cut samples, irradiated with 40 MeV I^{7+} at 1×10^{9} ion cm^{-2}, as the most suitable substrate for the plasmonic devices. The higher stopping power, combined with high acid concentration (20%w HF) and longer etching times (up to 1 hour), produced deeper nanowells with nanochannel-shapes at the sample surface. The nanowell had superficial dimensions of ~ 600 nm length, ~ 200 nm width, and depths up to ~ 1 μm.

7 nm diameter Au nanoparticles were deposited into the nanowells by drying drops of a diluted colloidal suspension (23 nM). Different nanoparticle concentrations were used to evaluate how the optical response of the plasmonic device is modified with different amounts of deposited nanoparticles. Raman spectroscopy was used as the main technique to evaluate the modification in the optical response. SEM micrographs confirmed that the procedure used produced gold nanoparticles confined within the

nanowells. Agglomerated nanoparticles were observed inside the nanowells with no significant presence at the sample surface. The enhancement in the electromagnetic field due to localized surface plasmons at the nanoparticle surfaces was observed as an increase in the Raman scattering intensities. A linear increase of the enhancement factor (I/I_o) was observed when depositing gold nanoparticles at low concentrations, reaching the maximum enhancement of 3.4 at a nanoparticle concentration of 4×10^6 nps/μL. Higher nanoparticle concentrations exponentially reduced the Raman intensity following the Beer-Lambert Law. It is believed that the Raman signal is attenuated due to an increase in the mass thickness of Au at the surface and accompanying increase in absorption of the incident laser light. Thus, the optimal nanoparticle concentration represents a balance between plasmonic enhancement and light absorption.

Additionally, phonon confinement effects in ion irradiated and subsequent etched samples were investigated. The analysis was conducted on both Y- and Z-cut α-SiO_2. Raman measurements indicated a blue shift and asymmetric broadening with positive skew after irradiation, in agreement with a phonon confinement effect. Similar results were found when analyzing the etched samples, with the main difference being that the Raman peaks red-shifted slightly from the irradiated sample values back to lower frequencies. This is interpreted as relaxation of the stress when the track core was removed in the etching process. Calculations of the phonon coherence length were conducted by curving fitting the experimental spectra and spectra obtained by a phonon confinement model. It was found that the phonon coherence lengths decreased with increasing flux suggesting that ion tracks may confine optical phonons in quartz

5. RECOMMENDATIONS AND FUTURE WORKS

This dissertation demonstrated several experimental techniques that can be used to produced ion tracks in crystalline quartz, etch them to produce anisotropic nanowells, and fill the nanowells with gold nanoparticles. A change in the Raman scattering intensity was successfully induced by the plasmonic nanoparticles inside of the nanowells. However, it is believed that the modification of the optical response of alpha quartz deserves further investigation in order to: (1) optimize the experimental procedures and thereby tailor a wider variety of novel plasmonic nanostructures and (2) characterize more of the optical properties of such structures and devices. Future works may include using different irradiation conditions (i.e. ion mass and energy) and etching processes with different acids that allow the production of nanowells with higher aspect ratios or different shapes. The Raman measurements can be improved by using nanostructures with different geometrical shapes, more controlled nanoparticle deposition with varying interparticle separation, and understanding in a more systematic way the parameters that govern the surface-enhanced Raman response. Also, more detailed SEM or TEM characterization is needed to quantitatively analyze the nanoparticle distribution along the depth of the nanowells. Different optical characterization techniques (i.e. absorbance, UV-Vis spectroscopy, ellipsometry, etc.) and interpretation of experimental data with models will help broaden the knowledge of how these 3D arrangements of deposited nanoparticles in dielectric media affect optical properties. In a more general sense, one seeks to understand the multitude of ways that such structures can couple incident electromagnetic radiation with various responses of the material.

BIBLIOGRAPHY

[1] M. L. Brongersma and V. M. Shalaev, "The Case for Plasmonics," *Science (80-.).*, vol. 328, no. 5977, pp. 440–441, 2010.

[2] M. Moskovits, "Surface roughness and the enhanced intensity of Raman scattering by molecules adsorbed on metals," *J. Chem. Phys.*, vol. 69, no. 9, pp. 4159–4161, 1978.

[3] Z. Liang, J. Sun, Y. Jiang, and L. Jiang, "Plasmonic Enhanced Optoelectronic Devices," *Plasmonics*, vol. 9, no. 4, pp. 859–866, 2014, doi: 10.1007/s11468-014-9682-7.

[4] E. Ozbay, "Plasmonics : Merging Photonics and Electronics at Nanoscale Dimensions," *Science (80-.).*, vol. 311, no. 5758, pp. 189–193, 2006.

[5] N. J. Halas, "Plasmonics : An Emerging Field Fostered by Nano Letters," *Nano Lett.*, vol. 10, no. 10, pp. 3816–3822, 2010, doi: 10.1021/nl1032342.

[6] L. Jiang *et al.*, "Free-standing one-dimensional plasmonic nanostructures," *Nanoscale*, vol. 4, no. 1, pp. 66–75, 2012, doi: 10.1039/c1nr11445j.

[7] S. V Boriskina, H. Ghasemi, and G. Chen, "Plasmonic materials for energy : From physics to applications," *Mater. Today*, vol. 16, no. 10, pp. 375–386, 2013, doi: 10.1016/j.mattod.2013.09.003.

[8] J. A. Schuller, E. S. Barnard, W. Cai, Y. C. Jun, J. S. White, and M. L. Brongersma, "Plasmonics for extreme light concentration and manipulation," *Nat. Mater.*, vol. 9, no. 3, pp. 193–204, 2010, doi: 10.1038/nmat2630.

[9] N. J. Halas, "Connecting the dots : Reinventing optics for nanoscale dimensions," in *Proceedings of the National Academy of Science*, 2009, vol. 106, no. 10, pp. 3643–3644.

[10] M. I. Stockman, "Nanoplasmonics : past , present , and glimpse into future," *Opt. Express*, vol. 19, no. 22, pp. 22029–22106, 2011, doi: 10.1021/nl2023299.

[11] W. L. Barnes, A. Dereux, and T. W. Ebbesen, "Surface plasmon subwavelength optics," *Nature*, vol. 424, no. 6950, pp. 824–830, 2003.

[12] R. H. Ritchie, "Surface plasmons in solids," *Surf. Sci.*, vol. 34, no. 1, pp. 1–19, 1973.

[13] C. F. Bohren, "How can a particle absorb more than the light incident on it ?," *Am. J. Phys.*, vol. 51, no. 4, pp. 323–327, 1983, doi: 10.1119/1.13262.

[14] U. Kreibig and M. Vollmer, *Optical Properties of Metal Clusters*, 1st ed. Base,l Switzerland: Springer-Verlag Berlin Heidelberg, 1995.

[15] X. Ni, N. K. Emani, A. V Kildishev, A. Boltasseva, and V. M. Shalaev, "Broadband Light Bending with Plasmonic Nanoantennas," *Science (80-.).*, vol. 335, no. 6067, p. 427, 2012, doi: 10.1126/science.1214686.

[16] V. Giannini, A. I. Fernández-Domínguez, S. C. Heck, and S. A. Maier, "Plasmonic Nanoantennas : Fundamentals and Their Use in Controlling the Radiative Properties of Nanoemitters," *Chem. Rev.*, vol. 111, no. 6, pp. 3888–3912, 2011, doi: 10.1021/cr1002672.

[17] S. Pillai and M. A. Green, "Plasmonics for photovoltaic applications," *Sol. Energy Mater. Sol. Cells*, vol. 94, no. 9, pp. 1481–1486, 2010, doi: 10.1016/j.solmat.2010.02.046.

[18] V. E. Ferry *et al.*, "Light trapping in ultrathin plasmonic solar cells," *Opt. Express*, vol. 18, no. 102, pp. A237–A245, 2010.

[19] P. Reineck, G. P. Lee, D. Brick, M. Karg, P. Mulvaney, and U. Bach, "A Solid-State Plasmonic Solar Cell via Metal Nanoparticle," *Adv. Mater.*, vol. 24, no. 35, pp. 4750–4755, 2012, doi: 10.1002/adma.201200994.

[20] M. C. Estevez, M. A. Otte, B. Sepulveda, and L. M. Lechuga, "Trends and challenges of refractometric nanoplasmonic biosensors : A review," *Anal. Chim. Acta*, vol. 806, pp. 55–73, 2014, doi: 10.1016/j.aca.2013.10.048.

[21] G. A. Lopez, M. C. Estevez, M. Soler, and L. M. Lechuga, "Recent advances in nanoplasmonic biosensors : applications and lab-on-a-chip integration," *Nanophonics*, vol. 6, no. 1, pp. 123–136, 2017, doi: 10.1515/nanoph-2016-0101.

[22] A. H. Nguyen and S. J. Sim, "Nanoplasmonic biosensor : Detection and amplification of dual bio-signatures of circulating tumor DNA," *Biosens. Bioelectron.*, vol. 67, pp. 443–449, 2015, doi: 10.1016/j.bios.2014.09.003.

[23] J. Li *et al.*, "Revisiting the Surface Sensitivity of Nanoplasmonic Biosensors," *Acs Photonics*, vol. 2, no. 3, pp. 425–431, 2015, doi: 10.1021/ph5004779.

[24] A. A. Yanik *et al.*, "An Optofluidic Nanoplasmonic Biosensor for Direct Detection of Live Viruses from Biological Media," *Nano Lett.*, vol. 10, no. 12, pp. 4962–4969, 2010, doi: 10.1021/nl103025u.

[25] R. Goul *et al.*, "Quantitative analysis of surface enhanced Raman spectroscopy of Rhodamine 6G using a composite graphene and plasmonic Au nanoparticle substrate," *Carbon N. Y.*, vol. 111, pp. 386–392, 2017, doi: 10.1016/j.carbon.2016.10.019.

[26] K. Kneipp *et al.*, "Single Molecule Detection Using Surface-Enhanced Raman Scattering (SERS)," *Phys. Rev. Lett.*, vol. 78, no. 9, pp. 1667–1670, 1997.

[27] J. B. Jackson and N. J. Halas, "Surface-enhanced Raman scattering on tunable plasmonic nanoparticle substrates," *Proc. Natl. Acad. Sci.*, vol. 101, no. 52, pp. 17930–17935, 2004.

[28] P. P. Patra, R. Chikkaraddy, R. P. N. Tripathi, A. Dasgupta, and G. V. P. Kumar, "Plasmofluidic single-molecule surface-enhanced Raman scattering from dynamic assembly of plasmonic nanoparticles," *Nat. Commun.*, vol. 5, no. 1, pp. 1–8, 2014, doi: 10.1038/ncomms5357.

[29] U. Guler *et al.*, "Local Heating with Lithographically Fabricated Plasmonic Titanium Nitride Nanoparticles," *Nano Lett.*, vol. 13, no. 12, pp. 6078–6083, 2013, doi: 10.1021/nl4033457.

[30] G. Baffou, J. Polleux, H. Rigneault, and S. Monneret, "Super-Heating and Micro-Bubble Generation around Plasmonic Nanoparticles under cw Illumination," *J. Phys. Chem. C*, vol. 118, no. 9, pp. 4890–4898, 2014, doi: 10.1021/jp411519k.

[31] I. Alessandri and L. E. Depero, "Using plasmonic heating of gold nanoparticles to generate local SER(R)S-active TiO2 spots," *Chem. Commun.*, vol. 17, pp. 2359–2361, 2009, doi: 10.1039/b900647h.

[32] X. Huang, P. K. Jain, I. H. El-sayed, and M. A. El-Sayed, "Plasmonic photothermal therapy (PPTT) using gold nanoparticles," *Lasers Med. Sci.*, vol. 23, no. 3, pp. 217–228, 2008, doi: 10.1007/s10103-007-0470-x.

[33] Q. Hao *et al.*, "VO2/TiN Plasmonic Thermochromic Smart Coatings for Room-Temperature Applications," *Adv. Mater.*, vol. 30, no. 10, pp. 1705421(1–5), 2018, doi: 10.1002/adma.201705421.

[34] A. Tittl *et al.*, "Plasmonic Smart Dust for Probing Local Chemical Reactions," *Nano Lett.*, vol. 13, no. 4, pp. 1816–1821, 2013, doi: 10.1021/nl4005089.

[35] G. Garcia, R. Buonsanti, A. Llordes, E. L. Runnerstrom, A. Bergerud, and D. J. Milliron, "Near-Infrared Spectrally Selective Plasmonic Electrochromic Thin Films," *Adv. Opt. Mater.*, vol. 1, no. 3, pp. 215–220, 2013, doi: 10.1002/adom.201200051.

[36] Q. Liu, Y. Yuan, and I. I. Smalyukh, "Electrically and Optically Tunable Plasmonic Guest–Host Liquid Crystals with Long-Range Ordered Nanoparticles," *Nano Lett.*, vol. 14, no. 7, pp. 4071–4077, 2014, doi: 10.1021/nl501581y.

[37] X. Zhang *et al.*, "Optical polarizers based on gold nanowires fabricated using colloidal gold nanoparticles," *Nanotechnology*, vol. 19, no. 28, pp. 285202(1–6), 2008, doi: 10.1088/0957-4484/19/28/285202.

[38] M. G. Campbell, Q. Liu, A. Sanders, J. S. Evans, and I. I. Smalyukh, "Preparation of Nanocomposite Plasmonic Films Made from Cellulose Nanocrystals or Mesoporous Silica Decorated with Unidirectionally Aligned Gold Nanorods," *Materials (Basel).*, vol. 7, no. 4, pp. 3021–3033, 2014, doi: 10.3390/ma7043021.

[39] Y. Leroux *et al.*, "Active Plasmonic Devices with Anisotropic Optical Response : A Step Toward Active Polarizer," *Nano Lett.*, vol. 9, no. 5, pp. 2144–2148, 2009, doi: 10.1021/nl900695j.

[40] M. Ye *et al.*, "Angle-insensitive plasmonic color filters with randomly distributed silver nanodisks," *Opt. Lett.*, vol. 40, no. 21, pp. 4979–4982, 2015.

[41] P. K. Jain and M. A. El-sayed, "Plasmonic coupling in noble metal nanostructures," *Chem. Phys. Lett.*, vol. 487, no. 4–6, pp. 153–164, 2010, doi: 10.1016/j.cplett.2010.01.062.

[42] Z. Fang *et al.*, "Evolution of Light-Induced Vapor Generation at a Liquid-Immersed Metallic Nanoparticle," *Nano Lett.*, vol. 13, no. 4, pp. 1736–1742, 2013, doi: 10.1021/nl4003238.

[43] E. M. Larsson, C. Langhammer, I. Zorić, and B. Kasemo, "Nanoplasmonic Probes of Catalytic Reactions," *Science (80-.).*, vol. 326, no. 5956, pp. 1091–1094, 2009.

[44] E. Lukianova-Hleb *et al.*, "Plasmonic Nanobubbles as Transient Vapor Nanobubbles Generated around Plasmonic Nanoparticles," *ACS Nano*, vol. 4, no. 4, pp. 2109–2123, 2010, doi: 10.1021/nn1000222.

[45] A. L. Lereu, R. H. Farahi, L. Tetard, S. Enoch, T. Thundat, and A. Passian, "Plasmon assisted thermal modulation in nanoparticles," *Opt. Express*, vol. 21, no. 10, pp. 12145–12158, 2013, doi: 10.1364/OE.21.012145.

[46] T. Chen, M. Pourmand, A. Feizpour, B. Cushman, and B. M. Reinhard, "Tailoring Plasmon Coupling in Self-Assembled One-Dimensional Au Nanoparticle Chains through Simultaneous Control of Size and Gap Separation," *J. Phys. Chem. Lett.*, vol. 4, no. 13, pp. 2147–2152, 2013, doi: 10.1021/jz401066g.

[47] T. Chung *et al.*, "Nanoislands as plasmonic materials," *Nanoscale*, vol. 11, no. 18, pp. 8651–8664, 2019, doi: 10.1039/c8nr10539a.

[48] H. Yu *et al.*, "Near-field spectral properties of coupled plasmonic nanoparticle arrays," *Opt. Express*, vol. 25, no. 6, pp. 6883–6894, 2017.

[49] Y. Sonnefraud, A. L. Koh, D. W. Mccomb, and S. A. Maier, "Nanoplasmonics : Engineering and observation of localized plasmon modes," *Laser Photonics Rev.*, vol. 6, no. 3, pp. 277–295, 2012, doi: 10.1002/lpor.201100027.

[50] R. Pilot, R. Signorini, C. Durante, L. Orian, M. Bhamidipati, and L. Fabris, "A Review on Surface-Enhanced Raman Scattering," *Biosensors*, vol. 9, no. 2, p. 57, 2019.

[51] F. A. Cucinotta, R. Katz, and J. W. Wilson, "Heavy ion track-structure calculations for radial dose in arbitrary materials," *Robert Katz ...*, no. February, 1995, [Online]. Available: http://digitalcommons.unl.edu/cgi/viewcontent.cgi?article=1003&context=physics katz%5Cnpapers3://publication/uuid/1F421F7E-C169-488C-B570-0E75E73F51CF.

[52] D. Schauries, B. Afra, M. D. Rodriguez, C. Trautmann, A. Hawley, and P. Kluth, "Ion track annealing in quartz investigated by small angle X-ray scattering," *Nucl. Instruments Methods Phys. Res. Sect. B Beam Interact. with Mater. Atoms*, vol. 365, pp. 380–383, 2015, doi: 10.1016/j.nimb.2015.07.081.

[53] D. M. Follstaedt, A. K. Norman, B. L. Doyle, and F. D. McDaniel, "Strain fields around high-energy ion tracks in α-quartz," *J. Appl. Phys.*, vol. 100, no. 6, 2006, doi: 10.1063/1.2345029.

[54] D. Schauries *et al.*, "Temperature dependence of ion track formation in quartz and apatite," *J. Appl. Crystallogr.*, vol. 46, no. 6, pp. 1558–1563, 2013, doi: 10.1107/S0021889813022802.

[55] A. Meftah *et al.*, "Track formation in SiO2 quartz and the thermal-spike mechanism," *Phys. Rev. B*, vol. 49, no. 18, pp. 12457–12463, 1994, doi: 10.1103/PhysRevB.49.12457.

[56] J. Manzano-Santamaría, J. Olivares, A. Rivera, and F. Agulló-López, "Electronic damage in quartz (c-SiO 2) by MeV ion irradiations: Potentiality for optical waveguiding applications," *Nucl. Instruments Methods Phys. Res. Sect. B Beam Interact. with Mater. Atoms*, vol. 272, pp. 271–274, 2012, doi: 10.1016/j.nimb.2011.01.081.

[57] W. Primak, L. H. Fuchs, and P. Day, "Effects of Nuclear Reactor Exposure on Some Properties of Vitreous Silica and Quartz," *Am. Ceram. Soc.*, vol. 38, no. 4, pp. 135–139, 1955, doi: https://doi.org/10.1111/j.1151-2916.1955.tb14916.x.

[58] A. Benyagoub, S. Löffler, M. Rammensee, S. Klaumünzer, and G. Saemann-Ischenko, "Plastic deformation in SiO2 induced by heavy-ion irradiation," *Nucl. Inst. Methods Phys. Res. B*, vol. 65, no. 1–4, pp. 228–231, 1992, doi: 10.1016/0168-583X(92)95039-T.

[59] H. Fischer, G. Götz, and H. Karge, "Radiation damage in ion-implanted quartz crystals. Part I: Nuclear and electronic energy deposition. Title," *Phys. status solidi*, vol. 76, no. 1, 1983, doi: https://doi.org/10.1002/pssa.2210760129.

[60] R. L. Fleisher, P. B. Price, and R. M. Walker, *Nuclear tracks in solids: Principles and applications*. Berkeley California: Univ of California Press, 1975.

[61] R. G. Macaulay-Newcombe and D. A. Thompson, "Ion bombardment damage in α-quartz at 50–295 K," *Nucl. Instruments Methods Phys. Res. Sect. B Beam Interact. with Mater. Atoms*, vol. 1, no. 2–3, pp. 176–182, 1984, doi: https://doi.org/10.1016/0168-583X(84)90065-X.

[62] S. Klaumünzer, "Ion tracks in quartz and vitreous silica," *Nucl. Instruments Methods Phys. Res. Sect. B Beam Interact. with Mater. Atoms*, vol. 225, no. 1-2 SPEC. ISS., pp. 136–153, 2004, doi: 10.1016/j.nimb.2004.05.014.

[63] Á. R. Páramo *et al.*, "Mechanical response to swift ion irradiation-induced nano-tracks in silica," *Nucl. Instruments Methods Phys. Res. Sect. B Beam Interact. with Mater. Atoms*, vol. 352, pp. 145–147, 2015, doi: 10.1016/j.nimb.2014.12.073.

[64] R. G. Musket, J. M. Yoshiyama, R. J. Contolini, and J. D. Porter, "Vapor etching of ion tracks in fused silica," *J. Appl. Phys.*, vol. 91, no. 5760, 2002, doi: 10.1063/1.1467402.

[65] M. Wong and R. A. Bowling, "Silicon Etch Using Vapor Phase HF/H2O and O3," *J. Electrochem. Soc.*, vol. 140, no. 2, pp. 567–570, 1993.

[66] M. A. Kozlova and P. A. Shkonda, "Structure of the Surfaces of Vitreous Silica and Quartz After Prolonged Etching in Hf.," *The Soviet journal of glass physics and chemistry*, vol. 13, no. 2. pp. 127–130, 1987.

[67] E. Y. Kaniukov *et al.*, "Tunable nanoporous silicon oxide templates by swift heavy ion tracks technology," *Nanotechnology*, vol. 27, no. 11, 2016, doi: 10.1088/0957-4484/27/11/115305.

[68] C. Hedlund, U. Lindberg, U. Bucht, and J. Soderkvist, "Anisotropic etching of Z-cut quartz," *J. Micromechanics Microengineering*, vol. 3, no. 2, 1993.

[69] P. Rangsten, C. Hedlund, I. V. Katardjiev, and Y. Bäcklund, "Etch rates of crystallographic planes in Z-cut quartz - Experiments and simulation," *J. Micromechanics Microengineering*, vol. 8, no. 1, pp. 1–6, 1998, doi: 10.1088/0960-1317/8/1/001.

[70] C. R. Tellier, "Some results on chemical etching of AT-cut quartz wafers in ammonium bifluoride solutions," *J. Mater. Sci.*, vol. 17, no. 5, pp. 1348–1354, 1982, doi: 10.1007/BF00752244.

[71] H. Iwata, "Multistage chemical etching for high-precision adjustment of resonance frequencies in ultrahigh-frequency-fundamental quartz resonators," *Proc. IEEE Int. Freq. Control Symp. Expo.*, pp. 121–124, 2005, doi: 10.1109/freq.2004.1418439.

[72] C. L. Phillips, R. J. Magyar, and P. S. Crozier, "A two-temperature model of radiation damage in α -quartz," *J. Chem. Phys.*, vol. 133, no. 14, 2010, doi: 10.1063/1.3481356.

[73] U. Utzinger and R. R. Richards-Kortum, "Fiber optic probes for biomedical optical spectroscopy," *J. Biomed. Opt.*, vol. 8, no. 1, p. 121, 2003, doi: 10.1117/1.1528207.

[74] F. P. Bolin, L. E. Preuss, R. C. Taylor, and R. J. Ference, "Refractive index of some mammalian tissues using a fiber optic cladding method," *Appl. Opt.*, vol. 28, no. 12, pp. 2297–2303, 1989.

[75] C. Stambaugh, H. Shakeel, D. Kalteyer, P. Abbott, and J. Pomeroy, "Traceability of frequency based mass measurements using a quartz crystal microbalance," *J. Phys. Conf. Ser.*, vol. 1065, no. 4, 2018, doi: 10.1088/1742-6596/1065/4/042002.

[76] M. Blomqvist, O. Blomster, M. Palsson, S. Campbell, F. Becker, and W. Rath, "All-in-quartz optics for low focal shifts," in *Proceedings Volume 7912, Solid State Lasers XX: Technology and Devices*, 2011, doi: 10.1117/12.874597.

[77] K. Momma and F. Izumi, "VESTA 3 for three-dimensional visualization of crystal , volumetric and morphology data," *J. Appl. Crystallogr.*, vol. 44, no. 6, pp. 1272–1276, 2011, doi: 10.1107/S0021889811038970.

[78] C. Hernandez-Rodriguez and P. Gomez-Garrido, "Optical anisotropy of quartz in the presence of temperature-dependent multiple reflections using a high-accuracy universal polarimeter," *J. Phys. D. Appl. Phys.*, vol. 33, pp. 2985–2994, 2000.

[79] W. Duojun, H. Li, L. Yi, T. Matsuzaki, and T. Yoshino, "Anisotropy of synthetic quartz electrical conductivity at high pressure and temperature," *J. Geophys. Res. Solid Earth*, vol. 115, no. B9, pp. 2–11, 2010, doi: 10.1029/2009JB006695.

[80] K. Midttomme and E. Roaldset, "The e ffect of grain size on thermal conductivity of quartz sands and silts," *Pet. Geosci.*, vol. 4, no. 2, pp. 165–172, 1998.

[81] C. Gao and W. Li, "Theoretical Research on the Bending Effect of Piezoelectric Quartz and Experimental Verification," in *2009 International Conference on Mechatronics and Automation*, 2009, pp. 1957–1961.

[82] K. linga Murty and I. Charit, *An introduction to nuclear materials: fundamentals and applications*, Illustrate. John Wiley & Sons, 2013, 2013.

[83] L. K. Mansur, A. F. Rowcliffe, R. K. Nanstad, S. J. Zinkle, W. R. Corwin, and R. E. Stoller, "Materials needs for fusion, Generation IV fission reactors and spallation neutron sources - Similarities and differences," in *Journal of Nuclear Materials*, 2004, doi: 10.1016/j.jnucmat.2004.04.016.

[84] G. García, A. Rivera, M. L. Crespillo, N. Gordillo, J. Olivares, and F. Agulló-López, "Amorphization kinetics under swift heavy ion irradiation: A cumulative overlapping-track approach," *Nucl. Instruments Methods Phys. Res. Sect. B Beam Interact. with Mater. Atoms*, vol. 269, no. 4, pp. 492–497, 2011, doi: 10.1016/j.nimb.2010.12.073.

[85] N. L. Singh, S. Shah, A. Qureshi, F. Singh, D. K. Avasthi, and V. Ganesan, "Swift heavy ion induced modification in dielectric and microhardness properties of polymer composites," *Polym. Degrad. Stab.*, vol. 93, no. 6, pp. 1088–1093, 2008, doi: 10.1016/j.polymdegradstab.2008.03.015.

[86] R. A. B. Devine, "Ion implantation- and radiation-induced structural modifications in amorphous SiO 2," vol. 152, pp. 50–58, 1993.

[87] J. Manzano, J. Olivares, F. Agulló-López, M. L. Crespillo, A. Moroño, and E. Hodgson, "Optical waveguides obtained by swift-ion irradiation on silica (a-SiO 2)," *Nucl. Instruments Methods Phys. Res. Sect. B Beam Interact. with Mater. Atoms*, vol. 268, no. 19, pp. 3147–3150, 2010, doi: 10.1016/j.nimb.2010.05.075.

[88] N. Itoh, D. M. Duffy, S. Khakshouri, and A. M. Stoneham, "Making tracks: Electronic excitation roles in forming swift heavy ion tracks," *J. Phys. Condens. Matter*, vol. 21, no. 47, 2009, doi: 10.1088/0953-8984/21/47/474205.

[89] E. C. H. Silk and R. S. Barnes, "Examination of fission fragment tracks with an electron microscope," *Philos. Mag.*, vol. 4, no. 44, pp. 970–972, 1959, doi: 10.1080/14786435908238273.

[90] M. Lang, R. Devanathan, M. Toulemonde, and C. Trautmann, "Advances in understanding of swift heavy-ion tracks in complex ceramics," *Curr. Opin. Solid State Mater. Sci.*, vol. 19, no. 1, pp. 39–48, 2015, doi: 10.1016/j.cossms.2014.10.002.

[91] M. Toulemonde, C. Trautmann, E. Balanzat, K. Hjort, and A. Weidinger, "Track formation and fabrication of nanostructures with MeV-ion beams," *Nucl. Instruments Methods Phys. Res. Sect. B Beam Interact. with Mater. Atoms*, vol. 216, no. 1–4, pp. 1–8, 2004, doi: 10.1016/j.nimb.2003.11.013.

[92] R. Hellborg, H. J. Whitlow, and Y. Zhang, *Ion Beams in Nanoscale and Technology*, Illustrate. Springer Science & Business Media, 2009, 2009.

[93] R. Spohr, "Status of ion track technology — Prospects of single tracks," *Radiat. Meas.*, vol. 40, pp. 191–202, 2005, doi: 10.1016/j.radmeas.2005.03.008.

[94] W. J. Weber, D. M. Duffy, L. Thomé, and Y. Zhang, "The role of electronic energy loss in ion beam modification of materials," *Curr. Opin. Solid State Mater. Sci.*, vol. 19, no. 1, pp. 1–11, 2015, doi: 10.1016/j.cossms.2014.09.003.

[95] J. Provost *et al.*, "Swift, Heavy Ions in Insulating and Conducting Oxides: Tracks and Physical Properties," *MRS Bull.*, vol. 20, no. 12, pp. 22–28, 1995, doi: 10.1557/S0883769400045863.

[96] J. Sajita, U. Gupta, and N. K. Jain, "Pharmaceutical and Biomedical Potential of Surface Engineered Dendrimers," *Crit. Rev. Ther. Drug Carrier Syst.*, vol. 24, no. 3, pp. 257–306, 2007.

[97] R. . Fleischer, P. B. Price, and R. . Walker, "Ion Explosion Spike Mechanism for Formation of Charged-Particle Tracks in Solids," *J. Appl. Phys.*, vol. 36, no. 11, pp. 3645–3652, 1965.

[98] D. Lesueur and A. Dunlop, "Damage creation via electronic excitations in metallic targets part II : A theoretical model," *Radiat. Eff. Defects Solids*, vol. 126, no. 1–4, pp. 163–172, Mar. 1993, doi: 10.1080/10420159308219701.

[99] A. Iwase *et al.*, "High energy heavy ion irradiation damage in oxide superconductor," *Nucl. Inst. Methods Phys. Res. B Beam Interact. with Mater. Atoms*, vol. 146, no. 1–4, pp. 557–564, 1998.

[100] S. Bouffard, C. Leroy, S. Della-Negra, A. Brunelle, and J. M. Costantini, "Damage production yield by electron excitation in mica for ion and cluster irradiations," *Philos. Mag. A*, vol. 81, no. 12, pp. 2841–2854, Dec. 2001, doi: 10.1080/01418610108217168.

[101] M. Toulemonde, C. Dufour, A. Meftah, and E. Paumier, "Transient thermal processes in heavy ion irradiation of crystalline inorganic insulators," *Nucl. Instruments Methods Phys. Res. Sect. B Beam Interact. with Mater. Atoms*, vol. 166, pp. 903–912, 2000, doi: 10.1016/S0168-583X(99)00799-5.

[102] C. Dufour and M. Toulemonde, "Thermal spike model in the electronic stopping power regime," in *Ion Beam Modification of Solids. Ion-Solid Interaction and Radiation Damage*, no. 61, W. Wendler and E. Wesch, Eds. Switzerland 2016: Springer Series in Surface Sciences, 1993, pp. 63–104.

[103] J. M. Costantini, S. Miro, F. Beuneu, and M. Toulemonde, "Swift heavy ion-beam induced amorphization and recrystallization of yttrium iron garnet," *J. Phys. Condens. Matter*, vol. 27, no. 49, 2015, doi: 10.1088/0953-8984/27/49/496001.

[104] F. Dessauer, "Über einige Wirkungen von Strahlen. I," *Zeitschrift für Phys.*, vol. 12, no. 1, pp. 38–47, 1923, doi: 10.1007/BF01328080.

[105] J. A. Van Vechten, R. Tsu, F. W. Saris, and D. Hoonhout, "Reasons to believe pulsed laser annealing of Si does not involve simple thermal melting," *Phys. Lett. A*, vol. 74, no. 6, pp. 417–421, 1979, doi: https://doi.org/10.1016/0375-9601(79)90241-X.

[106] P. Stampfli and K. H. Benneman, "Time dependence of the laser-induced femtosecond lattice instability of Si and GaAs: Role of longitudinal optical distortions," *Phys. Rev. B*, vol. 49, no. 11, p. 7299, 1994.

[107] A. Gottdang, D. J. W. Mous, and R. G. Haitsma, "The novel HVEE 5 MV Tandetron," *Nucl. Instruments Methods Phys. Res. B*, vol. 190, pp. 177–182, 2002.

[108] N. Itoh and A. M. Stoneham, "Materials modification by electronic excitation," *Radiat. Eff. Defects Solids*, vol. 155, no. 1–4, pp. 277–290, 2001, doi: 10.1016/S0169-4332(00)00587-0.

[109] A. Meftah *et al.*, "Swift heavy ions in magnetic insulators: A damage-cross-section velocity effect," *Phys. Rev. B*, vol. 48, no. 2, p. 920, 1993, doi: 10.1103/PhysRevB.48.920.

[110] J. Jensen, A. Dunlop, S. Della-Negra, and M. Toulemonde, "A comparison between tracks created by high energy mono-atomic and cluster ions in Y3Fe5O12," *Nucl. Instruments Methods Phys. Res. Sect. B Beam Interact. with Mater. Atoms*, vol. 146, no. 1, pp. 412–419, 1998, doi: https://doi.org/10.1016/S0168-583X(98)00442-X.

[111] C. Houpert, F. Studer, D. Groult, and M. Toulemonde, "Transition from localized defects to continuous latent tracks in magnetic insulators irradiated by high energy heavy ions: A HREM investigation," *Nucl. Instruments Methods Phys. Res. Sect. B Beam Interact. with Mater. Atoms*, vol. 39, no. 1, pp. 720–723, 1989, doi: https://doi.org/10.1016/0168-583X(89)90882-3.

[112] A. Rivera *et al.*, "Permanent modifications in silica produced by ion-induced high electronic excitation: Experiments and atomistic simulations," *Sci. Rep.*, vol. 7, no. 1, pp. 1–14, 2017, doi: 10.1038/s41598-017-11182-4.

[113] N. Khalfaoui, C. C. Rotaru, S. Bouffard, E. Jacquet, H. Lebius, and M. Toulemonde, "Study of swift heavy ion tracks on crystalline quartz surfaces," *Nucl. Instruments Methods Phys. Res. Sect. B Beam Interact. with Mater. Atoms*, vol. 209, pp. 165–169, 2003, doi: https://doi.org/10.1016/S0168-583X(02)02014-1.

[114] F. Aumayr, S. Facsko, A. S. El-said, C. Trautmann, and M. Schleberger, "Single ion induced surface nanostructures : a comparison between slow highly charged and swift heavy ions," *J. Phys. Condens. Matter*, vol. 23, p. 393301, 2011, doi: 10.1088/0953-8984/23/39/393001.

[115] P. Kluth *et al.*, "Fine Structure in Swift Heavy Ion Tracks in Amorphous SiO 2," *Phys. Rev. Lett.*, vol. 101, no. 17, p. 175503, 2008, doi: 10.1103/PhysRevLett.101.175503.

[116] B. Wang, Y. Yu, I. Pignatelli, G. Sant, and M. Bauchy, "Nature of radiation-induced defects in quartz," *J. Chem. Phys.*, vol. 143, no. 2, 2015, doi: 10.1063/1.4926527.

[117] C. G. Gunderson, S. T. Barlow, and B. Zhang, "FIB-milled quartz nanopores in a sealed nanopipette," *J. Electroanal. Chem.*, vol. 833, no. December 2018, pp. 181–188, 2019, doi: 10.1016/j.jelechem.2018.11.052.

[118] P. B. Price and R. M. Walker, "Chemical etching of charged-particle tracks in solids," *J. Appl. Phys.*, vol. 33, no. 12, pp. 3407–3412, 1962, doi: 10.1063/1.1702421.

[119] P. Apel, "Track etching technique in membrane technology," *Radiat. Meas.*, vol. 34, no. 1–6, pp. 559–566, 2001, doi: 10.1016/S1350-4487(01)00228-1.

[120] C. Milanez Silva, P. Varisco, A. Moehlecke, P. P. Fichtner, R. M. Papaléo, and J. Eriksson, "Processing of nano-holes and pores on SiO2 thin films by MeV heavy ions," *Nucl. Instruments Methods Phys. Res. Sect. B Beam Interact. with Mater. Atoms*, vol. 206, pp. 486–489, 2003, doi: 10.1016/S0168-583X(03)00803-6.

[121] G. M. Rignanese, J. C. Charlier, and X. Gonze, "First-principles molecular-dynamics investigation of the hydration mechanisms of the (0001) α-quartz surface," *Phys. Chem. Chem. Phys.*, vol. 6, no. 8, pp. 1920–1925, 2004, doi: 10.1039/b311842h.

[122] F. M. Ernsberger, "Structural effects in the chemical reactivity of silica and silicates," *J. Phys. Chem. Solids*, vol. 13, no. 3–4, pp. 347–351, 1960.

[123] J. S. Judge, "A Study of the Dissolution of SiO2 in Acidic Fluoride Solutions," *J. Electrochem. Soc.*, vol. 118, no. 11, p. 1772, 1971.

[124] D. J. Monk, D. S. Soane, and R. T. Howe, "A review of the chemical reaction mechanism and kinetics for hydrofluoric acid etching of silicon dioxide for surface micromachining applications," *Thin Solid Films*, vol. 232, no. 1, pp. 1–12, 1993, doi: 10.1016/0040-6090(93)90752-B.

[125] J. K. Vondeling, "Fluoride-based etchants for quartz," *J. Mater. Sci.*, vol. 18, no. 1, pp. 304–314, 1983, doi: 10.1007/BF00543840.

[126] C. R. Helms and B. E. Deal, " Mechanisms of the HF/H 2 O vapor phase etching of SiO 2 ," *J. Vac. Sci. Technol. A Vacuum, Surfaces, Film.*, vol. 10, no. 4, pp. 806–811, 1992, doi: 10.1116/1.577676.

[127] D. M. Knotter, "Etching mechanism of vitreous silicon dioxide in HF-based solutions," *J. Am. Chem. Soc.*, vol. 122, no. 18, pp. 4345–4351, 2000, doi: 10.1021/ja993803z.

[128] N. Miki, H. Kikuyama, I. Kawanabe, M. Miyashita, and T. Ohmi, "Gas-Phase Selective Etching of Native Oxide," *IEEE Trans. Electron Devices*, vol. 37, no. 1, pp. 107–115, 1990, doi: 10.1109/16.43806.

[129] P. Suda, A. . Zumsteg, and W. Zinng, "Anisotropy of Etching Rate for Quartz in Ammonium Bifluoride," in *33rd Annual Symposium on Frequency Control*, 1979, pp. 359–363, doi: 10.1109/FREQ.1979.200339.

[130] J. Jensen, G. Possnert, A. Razpet, and M. Skupinski, "Ion track formation below 1 MeV/u in thin films of amorphous SiO 2," *Nucl. Instrum. Methods Phys. Res. B.*, vol. 243, no. 1, pp. 119–126, 2006, doi: 10.1016/j.nimb.2005.07.226.

[131] B. Canut, M. G. Blanchin, S. Ramos-Canut, V. Teodorescu, and M. Toulemonde, "Incorporation of sol-gel SnO2: Sb into nanoporous SiO 2," *Nucl. Instruments Methods Phys. Res. Sect. B Beam Interact. with Mater. Atoms*, vol. 245, no. 1, pp. 327–331, 2006, doi: 10.1016/j.nimb.2005.11.123.

[132] M. L. Crespillo, "Ion beam damage by electronic excitation with swift heavy ions in lithium niobate : mechanisms and nanostructuring for photonic applications," Universidad Autonoma de Madrid, 2011.

[133] J. Jensen, A. Razpet, M. Skupin, and G. Possnert, "Ion tracks in amorphous SiO2 irradiated with low and high energy heavy ions," *Nucl. Instruments Methods Phys. Res. B*, vol. 245, pp. 269–273, 2006, doi: 10.1016/j.nimb.2005.11.072.

[134] M. L. Crespillo, J. T. Graham, Y. Zhang, and W. J. Weber, "In-situ luminescence monitoring of ion-induced damage evolution in SiO2 and Al2O3," *J. Lumin.*, vol. 172, pp. 208–218, 2016, doi: 10.1016/j.jlumin.2015.12.016.

VITA

Maria Camila Garcia Toro was born in Medellin, Colombia. She completed her undergraduate program at Universidad Nacional de Colombia (UNAL) in Medellin in April 2014 with a Bachelor of Science in Chemical Engineering. During her undergraduate program, Maria was an active member of the Electrochemical Engineering research group GRIEQUI, where she developed her thesis entitled "Construction and Characterization of anodes NiO-CGO for Hydrogen Oxidation in Intermediate- Temperature Solid Oxide Fuel Cells." During Summer 2013, she did an internship in electrochemical processes in the Department of Chemical and Biomolecular Engineering of the University of Tennessee, Knoxville, Tennessee, with the support of Dr. Thomas A. Zawodzinski and Dr. Gabriel Goenaga. On Fall 2014, Maria started as a graduate student for the Nuclear Engineering Department at the Missouri University of Science and Technology. Her master's research was focused on the synthesis of radioactive nanostructures (metallic and bimetallic) by irradiating with both neutrons and ionizing radiation in the Missouri University of Science and Technology research nuclear reactor (MSTR). This research was conducted to create radioactive nanostructures to be used in cancer treatment. Maria received her master's degree in summer16. After completing her master's, Maria continued with her doctoral studies in Nuclear Engineering. Her Ph.D. research was focused on the modification of optical and plasmonic properties of quartz by depositing gold nanoparticles in highly energetic ion tracks. Maria received her Doctorate of Philosophy in Nuclear Engineering in December 2020 from Missouri University of Science and Technology, Rolla, Missouri, USA.